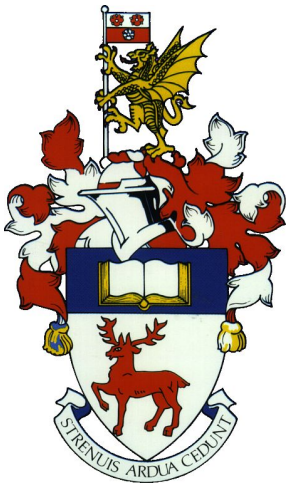

University of Southampton

Faculty of Engineering and Physical Sciences

Optoelectronics Research Centre

Advanced O-band Communications Enabled by a Novel Bismuth-Doped Fibre Amplifier

Natsupa Taengnoi

Doctor of Philosophy

January 2022

UNIVERSITY OF SOUTHAMPTON

ABSTRACT

FACULTY OF ENGINEERING AND PHYSICAL SCIENCES

Optoelectronics Research Centre

Doctor of Philosophy

ADVANCED O-BAND COMMUNICATIONS ENABLED BY A NOVEL BISMUTH-DOPED FIBRE AMPLIFIER

By Natsupa Taengnoi

Current optical transmission systems, based on erbium-doped fibre amplifier (EDFA) equipped wavelength division multiplexing (WDM) transmission in the C-band, are gradually being driven towards their capacity limits due to the rapid growth of data traffic. Several routes for increasing transmission capacity have been heavily investigated in recent years and it is unclear as of yet which solutions will be adopted. One solution is to increase the bandwidth utilisation of standard single-mode fibre (SMF) by pursuing transmission in regions beyond the C-band and doing so requires the availability of high-gain, low-noise amplifiers in the region of interest.

The objective of this thesis is to demonstrate the enablement of WDM transmission in the O-band by a newly developed bismuth-doped fibre amplifier (BDFA), offering high gain between 1320nm and 1370nm. This BDFA delivers effective, low-noise amplification and may finally provide an amplification solution for the O-band that is analogous to the ubiquitous C-band EDFA. If the BDFA is to be extensively used in the future, it will be necessary to undertake its characterisation by similar means to that performed on the EDFA in the early days of its development. This thesis reports the first parameterisation of the O-band BDFA in terms of its gain parameters and frequency-resolved noise figure to provide confidence in its performance and advise in its future development. To prove its practicality, the BDFA is successfully deployed in an amplified WDM O-band transmission testbed. The work further investigates the nonlinear performance of the BDFA as well as its transient characteristics. Finally, this thesis proposes an application of alternate-mark inversion to mitigate the nonlinearity in O-band transmission by applying it to on-off-keying and 4-level pulse amplitude modulation formats, the latter being the first time such a format has been demonstrated. Altogether, the results of this thesis suggest that the BDFA is a promising solution for O-band WDM systems.

Contents

List of Figures

List of Tables

Acronyms

AC ..... Alternating current
AMI ..... Alternate-mark inversion
ASE ..... Amplified spontaneous emission
ATT ..... Attenuator, optical attenuator
AWG ..... Arbitrary waveform generator
AWGN ..... Additive white Gaussian noise
B2B ..... Back-to-back
BAC ..... Bismuth active centre
BDF ..... Bismuth-doped fibre
BDFA ..... Bismuth-doped fibre amplifier
BER ..... Bit-error ratio
BERT ..... Bit-error ratio tester
BOA ..... Booster optical amplifier
C-band ..... Conventional-band
CD ..... Chromatic dispersion
CIRC ..... Circulator
CW ..... Continuous wave
CW-AMI ..... Continuous-wave alternate-mark inversion
CWDM ..... Coarse-wavelength-division multiplexing
CW-PAM ..... Continuous-wave pulse amplitude modulation
DAC ..... Digital-to-analogue converter
DB ..... Duobinary, 2-level duobinary
DC ..... Direct current
DCF ..... Dispersion compensating fibre
DD-MZM ..... Dual-drive Mach-Zehnder modulator
DFB ..... Distributed feedback
DFE ..... Decision-feedback equaliser
DML ..... Directly modulated laser

DMT ..... Discrete multi-tone transmission
DRS..... Double Rayleigh scattering
DSO ..... Digital storage oscilloscope
DSP..... Digital signal processing
DUT..... Device under test
DWDM..... Dense-wavelength-division multiplexing
E-band..... Extended-band
EDF ..... Erbium-doped fibre
EDFA..... Erbium-doped fibre amplifiers
FBG ..... Fibre Bragg grating
FEC..... Forward error correction
FL ..... Fibre laser
FOPA..... Fibre optical parametric amplifier
FWM..... Four-wave mixing
GVD..... Group velocity dispersion
HCF ..... Hollow-core fibre
HNLF ..... Highly nonlinear fibre
IMDD ..... Intensity modulation and direct detection
IoT ..... Internet of things
ISI ..... Inter-symbol interference
ISO..... Optical isolator
ITU ..... International telecommunication union
KK ..... Kramers–Kronig, Kramers–Kronig detection
LAS..... Laser
L-band..... Long-band
LD..... Laser diode
MFD..... Mode-field diameter
MUX ..... Multiplexer
MZM ..... Mach-Zehnder modulator
NANF..... Anti-resonant nodeless hollow-core fibre
NDFA..... Neodymium-doped fibre amplifier
NF..... Noise figure
NLSE..... Nonlinear Schrödinger equation
NRZ ..... Non-return-to-zero
NZDSF ..... Non-zero dispersion shifted fibre

O-band.....Original-band
OBPF .....Optical bandpass filter
ODC .....Oxygen deficient centre
OOK .....On-off keying
OPC .....Optical phase conjugation
OSA.....Optical spectrum analyser
OSC.....Oscilloscope
OSNR .....Optical signal-to-noise ratio
PAM.....Pulse amplitude modulation
PD .....Photodetector
PDFA .....Praeseodymium doped-fibre amplifier
PDG .....Polarisation dependent gain
PDL.....Polarisation dependent loss
PMD.....Polarisation mode dispersion
PolScr .....Polarisation scrambler
POW .....Power meter
PRBS.....Pseudorandom bit sequences
PS.....Pulsed source
PS-AMI .....Pulsed source alternate-mark inversion
PS-PAM .....Pulsed source pulse amplitude modulation
QAM.....Quadrature amplitude modulation
Q-factor .....Quality factor
QPSK .....Quadrature phase-shift keying
RF .....Radio frequency
RFSA.....Radio-frequency spectrum analyser
RIN.....Relative intensity noise
RLS .....Recursive least squares
RZ .....Return-to-zero
S-band .....Short-band
SBS.....Stimulated Brillouin scattering
SE.....Spectral efficiency
SMF.....Single-mode fibre
SNR.....Signal-to-noise ratio
SOA.....Semiconductor optical amplifier
SPM.....Self-phase modulation

SRS ..... Stimulated Raman scattering

SSE ..... Source spontaneous emission

SSMF ..... Standard single-mode fibre

TEC ..... Thermoelectric cooler

TOD ..... Third order dispersion

WDM ..... Wavelength-division multiplexing

XGM ..... Cross-gain modulation

XPM ..... Cross-phase modulation

Declaration of Authorship

I, Natsupa Taengnoi, declare that this thesis entitled *Advanced O-band Communications Enabled by a Novel Bismuth-Doped Fibre Amplifier* and the work presented in it are my own and has been generated by me as the result of my own original research.

I confirm that:

- This work was done wholly or mainly while in candidature for a research degree at this University;
- Where any part of this thesis has previously been submitted for a degree or any other qualification at this University or any other institution, this has been clearly stated;
- Where I have consulted the published work of others, this is always clearly attributed;
- Where I have quoted from the work of others, the source is always given. With the exception of such quotations, this thesis is entirely my own work;
- I have acknowledged all main sources of help;
- Where the thesis is based on work done by myself jointly with others, I have made clear exactly what was done by others and what I have contributed myself;
- Parts of this work have been published as listed in the Publications as First Author section;

Signature:

Date: 21st January 2022

Acknowledgements

Firstly, I am very grateful to my supervisors, Dr. Yang Hong and Prof. Periklis Petropoulos who have guided and supported me throughout my time at the University of Southampton. I am truly glad to have completed a PhD in this group at the Optoelectronics Research Centre (ORC). I would also like to thank Prof. David Richardson for helping me to improve the quality of my publications through his comments and suggestions.

My special thanks of gratitude go to Dr. Kyle Bottrill for his support and help. I cannot express enough thanks for his patience and dedication of help and teaching me about many new things in research since my master's degree and we have become a very good team over this time.

I would like to acknowledge the team at the ORC that developed and built the bismuth-doped fibre amplifier that enabled many of the studies I carried out during my PhD, including: Dr. Naresh Thipparapu, Yu Wang, Dr. Andrey Umnikov and Prof. Jayanta Sahu.

I would like to deeply thank my family for their support and as the best energy source for me, forever (not only throughout my time studying for my PhD). Even though they are living in Thailand and I am working in the UK, we have often been able to video call (in part thanks to optical telecoms!). I would like to thank: my dad, Supakorn, for his positive support and his rich experience in life; my mom, Panita, for her relaxing, heart-warming and funny attitude; and my sister, Tanakarn, for listening to me and supporting me throughout the challenges I have experienced. Furthermore, I would like to express my thanks to my two toy poodles, Prode and Pan, for their pure-love energy that I can sense even through video calls.

Finally, I am very sincerely grateful to Kasetsart University, Bangkok, Thailand, for fully funding my postgraduate studies at the University of Southampton, which has really been a golden opportunity for me. I would also like to thank Assoc. Prof. Wachira Chongburee and my colleagues at Kasetsart University for their kind support throughout my studies in Southampton.

Chapter 1

Introduction

The history of optical telecommunications can be characterised by a series of technological innovations offering dramatic increases in capacity which have managed to outpace ever growing demands for data. Growth in traffic has been driven both by an increase in subscribers as well as an increase in bitrate intensive services. Owing to the upcoming internet of things (IoT) and the increased use of video streaming (for entertainment, remote learning and business), these trends are unlikely to end soon [1] [2].

Since at least 1979, with the development of silica-based single-mode fibre (SMF) offering a loss below 0.5dB/km across a wavelength window of approximately 1150nm to 1700nm [3], the field of optical fibre telecommunications has been unsurpassed in its combination of reach and bandwidth. This fibre possessed a loss very close to the theoretical minimum for silica fibre and would effectively form the basis for the standard single-mode fibre (SSMF) that is still the most commonly used today [4]. The attenuation and dispersion profiles typical of a commercialised version of this type of fibre, Corning SMF-28e (a member of the SMF-28 family) [5], are provided in Figure 1-1. The underlying sources of loss in silica fibres include intrinsic factors, such as Rayleigh scattering and infrared absorption, as well as extrinsic factors, such as

water absorption (OH absorption) and various waveguide imperfections, see the labels in Figure 1-1. Despite the transmission fibre remaining relatively unchanged, link capacities have increased by several orders of magnitude due to other technological innovations which have supported a greater exploitation of the bandwidth available [1].

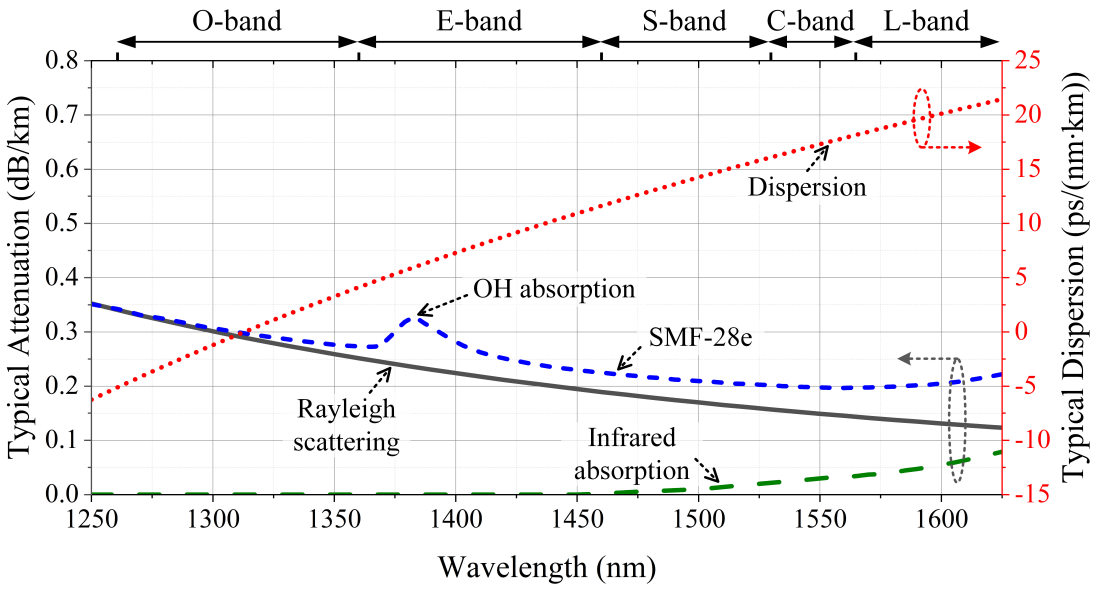

Figure 1-1: Attenuation and dispersion of SMF-28e with optical transmission bands labelled [5]. The wavelength range corresponding to each transmission band is as follows: O-band=1260-1360nm, E-band=1360-1460nm, S-band=1460-1530nm, C-band=1530-1565nm, and L-band=1565-1625nm.

Two main wavelength regions have been used for optical telecommunications, the O-band (original band) and the C-band (conventional band). The O-band was originally selected for its low chromatic dispersion (CD), which meant that broad linewidth light sources could be used with little distortion due to the very low dispersion [1]. On the other hand, the C-band region possesses a considerably higher dispersion, but also contains the lowest loss region of standard silica single-mode fibres (~0.2dB/km compared to the O-band's ~0.3dB/km). At first, dispersion was overcome using specially designed dispersion shifted fibre (which offered a lower dispersion) and narrower linewidth lasers [6], but transmission returned to SSMF with the invention of the erbium-doped fibre amplifier (EDFA) in 1987 [7]. The EDFA offered, for the first time, a broadband and highly linear solution to optical amplification. With a bandwidth of ~4.4THz [8], it was capable of supporting very many channels, which, around the time of the EDFA's introduction in the early 1990s, would have had

bandwidths of ~2.5GHz [1]. The low-noise gain of the EDFA enabled the use of dispersion compensating fibre (DCF) and opened up the era of wavelength division multiplexing (WDM), where capacity could be increased simply through the addition of additional channels. The combination of the EDFA with WDM transmission triggered the greatest leap in link capability so far seen in the evolution of optical telecommunications – an increase in capacity-distance product by 2 orders of magnitude over just a three-year period [1].

Since the WDM revolution in the 1990s, internet traffic has slowly been growing into the latent bandwidth of the EDFA and it is only recently that pressures on link bandwidth have been felt [1] [2]. This has led to the introduction of higher spectral efficiency (SE) formats (such as 4-level pulse amplitude modulation (PAM) and 16-ary quadrature amplitude modulation (16QAM)) and coherent communication (which offers higher receiver sensitivity) to bring link data rates closer to their theoretical capacity [2] [9]. Eventually, however, efforts must be directed towards increasing the capacity itself and this can be achieved in two ways: increasing SNR or increasing bandwidth (excluding efforts towards using multiple spatial modes, assuming the continued use of SSMF) [2].

Economics and technology will certainly determine the solutions which are ultimately adopted, but a quick look at the Shannon theorem shows that there is a fundamental difference between the returns of the two approaches – SNR and bandwidth. Shannon proved that reliable, error-free communication through a memory-less channel in the presence of additive white Gaussian noise (AWGN) is achievable if the transmitted information rate (R) is within the lower bound of the channel capacity, the so called *Shannon limit* [2] [9] [10], given by:

$$C = 2MB\log_2(1 + SNR) \qquad \text{Equation 1-1}$$

where, the factor of 2 accounts for the use of two polarisation modes.

M is the number of spatial paths.

B is the system bandwidth.

SNR is the signal-to-noise ratio.

To visualise the scaling of capacity, C, with SNR and B, an analytical plot of the equations given below is provided in Figure 1-2, which are essentially modified versions

of Equation 1-1 (with single spatial path, $M = 1$, and single polarisation) into which a scaling factor, δ, has been inserted:

$$C = B_0 \log_2[1 + (SNR_0 \times \delta)] \quad \text{: for scaling SNR} \qquad \text{Equation 1-2}$$

$$C = (B_0 \times \delta) \log_2[1 + SNR_0] \quad \text{: for scaling bandwidth} \qquad \text{Equation 1-3}$$

where, the initial value of SNR_0 is set to 25 (14dB), which corresponds to bit-error ratios (BERs) in on-off keying (OOK) 5×10^{-6} [11].
Meanwhile, B_0 is set to be 4.4THz, the bandwidth of a typical C-band EDFA.

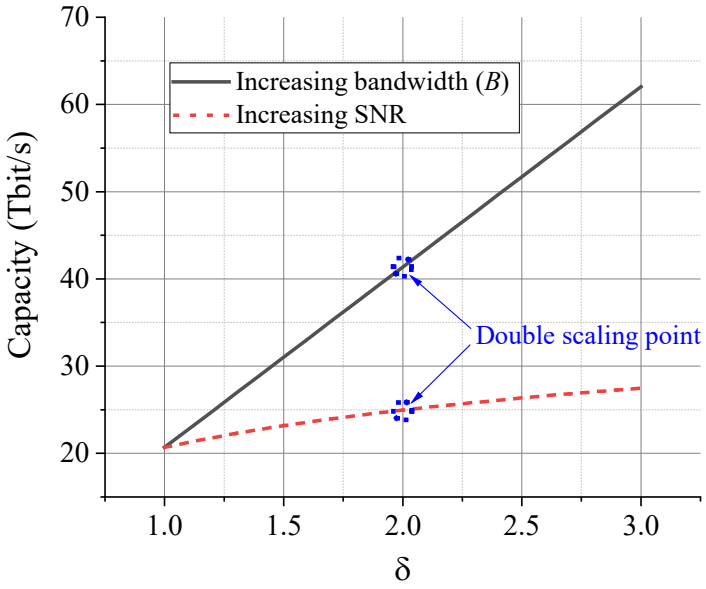

Figure 1-2: Analytical plot of channel capacity as it varies with the scaling factor, δ, when increasing the SNR (dashed line, Equation 1-2) and the bandwidth (solid line, Equation 1-3).

As is clearly shown in Figure 1-2, scaling bandwidth results in a greater gain in capacity than scaling SNR, suggesting that it may be more efficient to focus on improving bandwidth, B, to benefit from the linear scaling of capacity with these pre-log factors, rather than increasing the SNR only to receive logarithmic and hence rapidly fading, returns [2]. Specifically, a doubling of bandwidth offers a doubling of capacity, whilst a doubling of SNR results in only a ~20% increase in capacity.

Both approaches are, however, being studied and it should be noted that the above discussion does not take into account economic and practical factors, whose trends may not be trivial. Examples of techniques currently being studied for SNR improvement include: lower-noise optical amplifiers [7] [12], lower-loss fibre [13], lower

nonlinearity fibre [14], digital nonlinearity compensation, and optical phase conjugation [15]. Meanwhile, efforts to improve transmission bandwidth include novel transmission fibre (such as nested anti-resonant nodeless hollow-core fibre, NANF [16]), broader bandwidth amplifiers [17] [18], and amplifiers in alternative transmission bands [19] [20].

Focussing on alternative transmission bands, in expectation of continued traffic growth catered for through an ever-increasing number of WDM channels, S- and L-band systems have been discussed (and indeed marketed) since the 1990s [21]. Both bands benefit from lying close to the lowest loss region of the silica fibre, possess similar dispersive properties to the C-band and are served by a number of doped fibre amplifiers (such as EDFAs and thulium-doped fibre amplifiers, although these variants typically have worse performance, such as lower gain and higher noise figure (NF) than C-band EDFAs [22] [23] [24]) and Raman amplifiers [25]. Interestingly, the phenomenon that enables Raman amplification is also behind one of the challenges of ultra-wideband communication [6] [25]. In silica fibre, the Raman shift is approximately 100nm, meaning that if two signals are separated by 100nm, the shorter wavelength signal will tend to lose power to the longer wavelength signal (at room temperature) [25]. In the context of S+C and C+L band systems, it can be understood that there could be a power transition from S to C bands and from C to L bands, respectively. Efforts have been made to apply pre-emphasis to combat this [25], but the Raman effect remains a challenge that complicates such ultra-wideband transmission.

A less discussed solution is a return to the O-band. In the context of multiband transmission, the O-band is far enough away from the C-band that no Raman interaction will occur between them, and advantages can be taken of its lower CD (although it should be noted that it is lossier than the C-band). Outside of multiband communication, the low CD may make dense WDM (DWDM), with channel spacings of 50GHz to 200GHz, communication in the O-band a more cost-effective solution for short, inter-datacentre interconnects. One of the main reasons that of DWDM O-band transmission has not been deployed is a lack of suitable optical amplification, with available amplifiers either being too noisy (such as the neodymium-doped fibre amplifier, NDFA [26]) or suffering from too much nonlinearity (such as semiconductor optical amplifiers (SOAs) [27]).

Recently, a new doped fibre amplifier with O-band operation has been developed, a bismuth-doped fibre amplifier (BDFA), offering a peak gain of more than 25dB [28] and a 5-dB bandwidth (chosen because this was the range over which transmission was performed) of ~8.3THz (~1320–1370 nm), which is 1.9 times larger than the typical ~4.4THz offered by C-band EDFAs [8]. With a performance approaching or exceeding that of the EDFA (by certain metrics), the newly developed BDFA, coupled with an increasing demand for bandwidth beyond the C-band, may enable the development of the first commercial DWDM O-band links. This possibility is the motivation for the work in this thesis. If the BDFA is to be adopted in real telecommunications systems, there must be confidence in its performance and an understanding of how best to implement amplified DWDM O-band communications, since the higher loss and lower CD could make it quite different to the C-band. Therefore, if the greatest benefit is to be taken from the BDFA, it will be important to both comprehensively characterise the BDFA as well as to deploy it in practical systems and both of these tasks have been thoroughly performed during the work presented in this thesis.

1.1 Thesis Outline and Contribution

The thesis is organised as follows.

Chapter 2 provides the theoretical background necessary to set the context of the experimental work presented in later chapters. The chapter begins with a discussion of the key impairments experienced by signals during transmission as well as their solutions and the link between these impairments and the terms of the nonlinear Schrödinger equation are identified. Afterwards, the characteristics of the O-band in terms of these parameters is described and some challenges discussed. The chapter then moves on to discuss the properties of optical amplifiers in general, covering the concepts of optical gain and NF. Finally, the operating principles and characteristics of several optical amplification techniques that could be used in O-band transmission are introduced, including SOAs, Raman amplifiers, and doped-fibre amplifiers, closing with an explanation of the novel O-band BDFA that will be studied throughout this thesis.

Chapter 3 details a set of gain characterisations of the BDFA that confirm its suitability for amplified WDM transmission and provide useful information for future system design and modelling. The characterisations include the measurement of static

and dynamic gain tilts, transient response, cross-gain modulation, and polarisation dependent gain, in which the result of transient response is also compared with a commercial O-band SOA.

Chapter 4 presents the theory and experimental measurement of frequency-resolved NF using the electrical method. Although this method requires a more complicated procedure than the more commonly used optical technique, it is understood to be a more complete measurement of NF and allows for the observation of low-frequency noise components that could be undetectable using the optical method, which is particularly important for novel amplifiers like the BDFA. The performance of the BDFA is then benchmarked against a C-band EDFA that is also measured in this chapter. Furthermore, the frequency-resolved NF characterisation is also applied to several other optical amplifiers, including the commercial O-band SOA tested throughout this work, a double-pass O-band BDFA, and a broadband Raman amplifier.

Chapter 5 studies the performance of the BDFA in a practical amplified O-band WDM transmission system. It includes both coarse and dense spacing between the channels, which number from two to six channels. The transmission experiments are performed with ~10Gbit/s OOK signals. This experimental work is understood to be the first O-band WDM transmission with a BDFA-equipped link. Additionally, the nonlinear behaviour of the amplifiers used in the transmission, the SOA and BDFA, are also investigated.

Chapter 6 demonstrates a modulation technique to mitigate nonlinearity for intensity-signalling format in O-band transmission by using a partial response format, alternate-mark inversion. The modulation scheme is applied into 2- and 4-level formats and the results are compared to their traditional non-return-to-zero variants, OOK and PAM4, respectively. Performance in SOA and BDFA equipped links was studied.

Chapter 7 concludes all experiments presented in this thesis and discusses their outcomes. Finally, directions for further development and future work are provided.

Chapter 2

Background

The objective of this chapter is to provide the background information necessary to understand the research presented in the remainder of the thesis and place it in the context of O-band telecommunications in SSMF. The chapter begins by describing the main impairments experienced by signals when they propagate along optical fibres. These phenomena will be connected to the nonlinear Schrödinger equation and commonly used methods to mitigate these impairments will be described. Afterwards, the specific characteristics of the O-band will be discussed, as it is in this band that the work of this thesis takes place. The main theme of this thesis is novel O-band transmission enabled by the BDFA and, as such, the next discussion describes the theory behind some of the most fundamental parameters of an optical amplifier – gain and NF. After this, some current solutions for O-band amplification are discussed, before the BDFA itself is described. Following this presentation, the reader will have sufficient context for the subsequent experimental chapters.

2.1 Impairments and Solutions in Optical Transmission

To develop effective, high capacity, amplified O-band transmission systems, it is first necessary to understand, generally, the impairments in typical transmission systems, how they can be overcome and specifically, how they manifest in the O-band.

Firstly, it should be mentioned that the discussion in this thesis will assume, unless otherwise stated, that the transmission fibres used are compliant with the G.652 ITU standard [4], as fibres meeting this standard are by far the most commonly deployed fibres in the kinds of short to medium haul optical networks in which O-band communication is most relevant [29] [30]. People often refer to such fibres using: "SMF", "SMF-28", "SSMF", or "Standard telecoms fibres", owing to the popularity of Corning SMF-28 fibre. It will be assumed that such fibre has the following nominal parameters: an attenuation of ~0.2dB/km and dispersion of approximately 17ps/(nm·km) at the wavelength of 1550nm; an attenuation of ~0.3dB/km and a dispersion of approximately 0ps/(nm·km) at the wavelength of 1310nm.

2.1.1 Nonlinear Schrödinger Equation

To develop the background for discussing impairments during transmission and solutions that are commonly employed in telecommunications systems, it is helpful to make use of a mathematical model of pulse propagation in an optical fibre. In this thesis, considering a scalar model of such propagation is sufficient to satisfy our purposes, wherein all electric fields are assumed to be, and always remain, co-polarised. We consider the longitudinal evolution of a complex wave, $E(z,t)$, as it propagates along a fibre. We also assume that the complex wave can be explained as a carrier wave with angular frequency, ω, modulated by a complex, time dependent envelope, $A(z,t)$. As such the propagating wave can be written as [6]:

$$E(z,t) = A(z,t)e^{i(\omega t - \beta z)} \qquad \text{Equation 2-1}$$

where, β is the propagation constant (or phase constant), given by $\beta = \frac{2\pi n}{\lambda} = \frac{\omega n}{c}$ (where λ is the carrier wavelength, n is the refractive index, and c is the speed of light in vacuum, ~3×10^8 m/s).

z is the longitudinal propagation distance.

t is time.

The evolution of the envelope function, $A(z,t)$, travelling in single-mode fibre, can be described using a simplified version of the *generalised Nonlinear Schrödinger Equation (NLSE),* provided in Equation 2-2 (re-arranged from [31]). The condition of using the NLSE is that the envelope of the pulse needs to vary slowly compared to the carrier frequency of the electromagnetic field [31].

$$\frac{\partial A}{\partial z} = \underbrace{-\frac{\alpha}{2}A}_{\substack{attenuation \\ term}} \underbrace{-\frac{i\beta_2}{2}\frac{\partial^2 A}{\partial t^2} + \frac{\beta_3}{6}\frac{\partial^3 A}{\partial t^3}}_{\substack{dispersion \\ terms}} \underbrace{+ i\gamma|A|^2 A}_{\substack{nonlinearity \\ term}} \qquad \text{Equation 2-2}$$

where, α is the attenuation coefficient.

β_2 is the group velocity dispersion (GVD).

β_3 is the third order dispersion (TOD).

γ is the Kerr nonlinearity coefficient, and $\gamma = \frac{n_2\omega}{cA_{eff}}$ where n_2 is the nonlinear refractive index and A_{eff} is the effective area of the fibre.

Note that this simplified NLSE does not consider other nonlinear effects. For example, Raman scattering and backward-scattering effects are completely ignored [31]. However, it provides a sufficiently accurate description of the systems studied in this thesis.

In the next section, we will discuss the terms on the right-hand side of Equation 2-2, which can be divided into three parts – attenuation, CD, and fibre Kerr nonlinearity (as labelled in the equation), in terms of their effects in general, implications for telecommunication signals, and possible ways to overcome their impact.

2.1.2 Attenuation Effects on Transmission

In the optical fibre, attenuation (represented by the parameter α) originates from a range of processes such as infrared absorption and Rayleigh scattering of light out of the fibre. Attenuation simply causes a loss of power from the transmitted pulse as the pulse propagates along a fibre, resulting in reduced power arriving at the receiver, which can be expressed as [6]:

$$P(z) = P(0)e^{-\alpha z} \qquad \text{Equation 2-3}$$

where, $P(z)$ is the power after signal propagating over a distance, z, along the fibre.

$P(0)$ is the launch power.

The amount of power required at the receiver for acceptable communication performance is determined by the sensitivity of the receiver. Insufficient power at the receiver may contribute to errors in the detected signal. Therefore, for a given fixed total reach, loss is overcome either by using higher launch powers or making use of periodic optical amplification. However, increasing launch power can potentially lead to nonlinear distortion (see discussion later in nonlinear effects in Section 2.1.4) and

amplifiers are generally the greatest source of additive noise in transmission links [32] and so both of these approaches have their limitations. Other options are to use lower loss fibre [13], which in the future may include low loss hollow core fibres [33], install lower noise amplifiers, such as phase sensitive amplifiers [12], or use higher sensitivity receivers, such as coherent receivers [6].

2.1.3 Chromatic Dispersion Effects on Transmission

The term chromatic dispersion (CD) describes the effects of a frequency dependent refractive index, $n(\omega)$, on propagating light [31]. It is often expressed in terms of a frequency dependent propagation constant, $\beta = \frac{\omega\, n(\omega)}{c}$, which can in general take any shape and hence is often approximated by a truncated Taylor series expansion about a centre frequency, ω_0 [6]:

$$\beta(\omega) = \beta_0 + (\omega - \omega_0)\beta_1 + \frac{1}{2}(\omega - \omega_0)^2 \underbrace{\beta_2}_{GVD} + \frac{1}{6}(\omega - \omega_0)^3 \underbrace{\beta_3}_{TOD} + \cdots \qquad \text{Equation 2-4}$$

where, β_0 is the common phase shift applied to all frequencies by the medium.

β_1 is the reciprocal of the group velocity (v_g), which represents the traveling speed of the waveform's envelope along the fibre, and $v_g = \frac{d\omega}{d\beta} = \frac{1}{\beta_1}$.

Here, we only consider the effects due to GVD (β_2) and TOD (β_3) (as labelled in Equation 2-4). Although higher order dispersive terms may also be included, this is sufficient to discuss any important phenomena observed in this work. Some details of the terms GVD and TOD in optical transmission are provided as follows:

- GVD: This term, which can be described as $\beta_2 = \frac{d^2\beta}{d\omega^2} = \frac{1}{c}\left(\omega\frac{d^2n}{d\omega^2} + 2\frac{dn}{d\omega}\right)$, is generally the dominant term responsible for different frequency components contained in a wave packet propagating at different speeds or velocities. Therefore, it causes a wave travelling along a fibre to become chirped, which may lead to so called *dispersion-induced pulse broadening* (depending upon the initial state of chirp of the pulse).

  When discussing the GVD in fibre, β_2 is more commonly reformulated as time delay per wavelength per unit length rather than phase delay per angular frequency per unit length. The relationship between the two is given by: $D = -\frac{2\pi c}{\lambda^2}\beta_2$, and this term, D, is often referred to simply as *dispersion*. The

average values of dispersion corresponding to the SMF-28e used in this thesis are shown in Figure 2-1.

GVD describes the effect of dispersion on light per unit length propagated through an optical medium. Integrating GVD over the length of a device or medium results in a quantity named *group delay dispersion* (GDD).

- TOD: This term can be defined as $\beta_3 = \frac{d^3\beta}{d\omega^3} = \frac{1}{c}\left(\omega\frac{d^3n}{d\omega^3} + 3\frac{d^2n}{d\omega^2}\right)$ and can be considered to simply account for the frequency dependence of GVD.

  As with GVD, it is more common to use the dispersion slope, $D' = \frac{dD}{d\lambda}$, rather than β_3, in optical telecommunications.

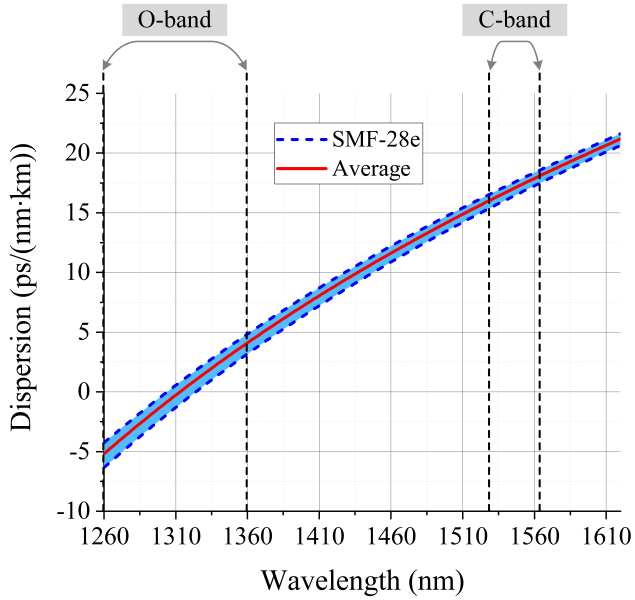

Figure 2-1: Dispersion values of SMF-28e [5]. The shading between the dashed lines represents the variation of the dispersion and the solid line is its average. The formula for the analytical plot can be found in [5].

The effects caused by CD can be observed as a simple phase shift in the frequency domain, since CD arises from the frequency dependence of the propagation constant. This implies that we cannot observe the results of dispersion through the power spectrum of a dispersed wave, for instance, as provided by an optical spectrum analyser (OSA). In any case, the phase shift in the frequency domain can cause a distortion of the waveform in the time domain, which can be observed as pulse broadening. It is through this pulse broadening that CD is able to cause inter-symbol interference (ISI).

Although CD cannot be observed in the power spectrum of an optical signal, it does manifest in the electrical power spectrum of a photo-detected double-sideband signal. A good example that is worth discussing in this context is *periodic deep power fading*, also known as *frequency selective fading*. It occurs when two frequency components symmetric about a carrier have accumulated a π-phase shift between them, due to CD, and hence the beating between the two tones and the carrier destructively interferes, resulting in the attenuation of electrical power at that frequency. If data is contained within the attenuated frequency at which fading has occurred, it will be weakened or diminished. The relative phase shift ($\Delta\phi$) caused by the dispersion can be expressed as:

$$\Delta\phi = \frac{8\pi DLc\Delta\lambda^2}{4\lambda_0^2 - \Delta\lambda^2} \quad : \text{wavelength, or}$$

$$= \frac{8\pi DLc\Delta f^2}{4f_0^2 - \Delta f^2} \quad : \text{frequency} \qquad \text{Equation 2-5}$$

where, L is the transmission reach.

$\Delta\lambda$ and Δf is the wavelength and frequency bandwidth, respectively.

λ_0 and f_0 is the centre (carrier) wavelength and frequency, respectively.

Figure 2-2 provides analytical plots of power fading due to dispersion, according to Equation 2-5, experienced after transmission over 100km of SMF-28e at three different example wavelengths in SMF-28e: -0.28ps/(nm·km) at 1310nm, 4.1ps/(nm·km) at 1360nm, and 17.29ps/(nm·km) at 1550nm (see the solid line in Figure 2-1). The effects of CD can be seen by a roll-off in frequency response, which fades faster for higher values of dispersion in the bandwidth presented. The results show that, if the reach is fixed, the higher the dispersion, the narrower the useable ('unfaded') bandwidth if dispersion compensating techniques are not employed.

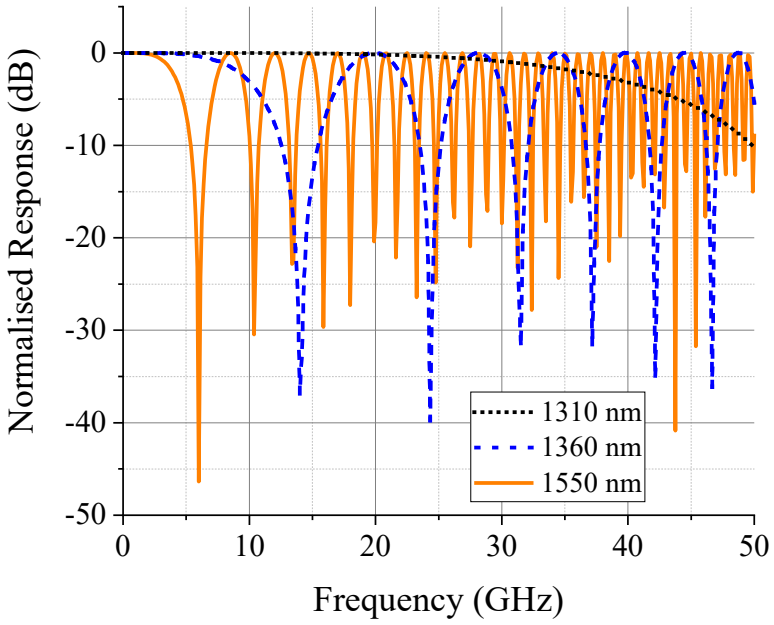

Figure 2-2: Power fading caused by dispersion after 100-km transmission over SMF-28e at the wavelengths of 1310nm, 1360nm, and 1550nm.

In short reach links, dispersion may simply be tolerated, with baud rates kept within the unfaded bandwidth of a signal, or techniques such as discrete multi-tone transmission (DMT) used to simply avoid using bandwidth that lies at deeply faded frequencies [34] [35]. There are, however, several techniques to manage CD in transmission systems. In the absence of other distortions, after a signal experiences dispersion in a fibre span/link, we can simply compensate the dispersion by passing the signal through a second fibre/device with the same magnitude of total dispersion as the first span, but of opposite polarity. The fibre type used for this purpose is referred to as dispersion compensating fibre (DCF) and it is typically much more dispersive than SSMF, so that a shorter length of DCF can be used to compensate for a given length of SSMF to minimise losses. The losses imposed by DCF may necessitate the use of additional optical amplification. Alternatively, the broadening of a pulse due to CD can also be compensated using a chirped fibre Bragg grating (FBG), by reflecting different wavelengths at different points along the length of the grating [36]. FBGs may offer lower loss compared to DCF, however, they are generally thermally sensitive, so controlling the level of compensation may require feedback circuitry or an athermal grating design [37].

The previously discussed solutions to dispersion compensation are optical-based methods, however, dispersion compensation can also be performed in the digital domain through digital signal processing (DSP). Dispersion compensation can be

readily performed in coherent systems, as it constitutes a simple, frequency dependent, phase shift of the received signal in the frequency domain. Given that the technique is applied in the digital domain, the amount of dispersion compensation can be more flexibly adjusted than with optical methods. However, it should be noted that the phase noise in the local oscillator used to decode the coherent signal is converted into amplitude noise upon detection in a coherent receiver, which does result in reduced effectiveness [6]. Other digital techniques include digital predistortion (pre-chirping) of a signal before transmission [38] [39], single sideband transmission [40] and the use of formats more tolerant to CD, such as duobinary signalling [41] and minimum shift keying [42].

Making use of these examples of dispersion compensation techniques is essential for transmission systems in commercial C-band systems, wherein the dispersion of SMF-28e (and its variants) can be as high as 17.29 ps/(nm·km). The shorter-wavelength region of the same fibre, the O-band, attractively contains the zero-dispersion wavelength (λ_0) of SMF-28e around 1304–1324nm (see Figure 2-1) and offers relatively low dispersion throughout the entire band. Signals propagating near λ_0 experience little dispersion-induced distortion, therefore the use of this wavelength range was popular in early telecommunications.

2.1.4 Nonlinear Effects on Transmission

The optical Kerr effect is typically the main source of nonlinearity in optical fibres. The Kerr effect causes the refractive index of the medium to be dependent upon the intensity of light, which can be expressed as:

$$n = n_0 + n_2 I \qquad \text{Equation 2-6}$$

where, n_0 is the common or linear refractive index.

n_2 is the nonlinear refractive index.

I is the intensity of the propagating signal, $I \propto |E|^2$.

The intensity of light, I, depends on both the total power of the light as well as the confinement of the light (effective area) in the core of the optical fibre [41]. Although silica typically has only low to moderate nonlinearity compared to other media (for example it is higher than some fluoride glasses by 0.6 times [43], but lower than some chalcogenide glasses by two orders of magnitude [44]), it is the tight confinement in

fibre and long propagation lengths (enabled by the low loss of fibre) that make Kerr effect induced nonlinearities relevant in SSMF.

In the nonlinear Schrödinger equation, Equation 2-2, the term $i\gamma|A|^2A$ encapsulates the effects of Kerr nonlinearity. This term can be expanded to describe three main nonlinear phenomena affecting optical transmission in SSMF – self-phase modulation (SPM), cross-phase modulation (XPM), and four-wave mixing (FWM).

- SPM is the phenomenon in which a propagating pulse experiences a nonlinear phase-shift which is proportional to the instantaneous intensity of the pulse itself. This phenomenon derives from the intensity dependent change in refractive index of the fibre, as described by Equation 2-6, which then translates into a change in propagating speed (v) of the pulse from $v = \frac{c}{n}$, and finally results in the SPM induced phase shift. The higher the instantaneous power of the propagating pulse, the higher the phase shift within the pulse at that point in time. Typically, this phase shift can be observed as a change in the waveform [6], as shown in the example in Figure 2-3, which shows the characteristic 'cat-ear' profile [45] of a pulse heavily distorted by SPM (and a small amount of dispersion). The combination of pulse broadening due to dispersion with this *cat-ear profile* may can lead to ghost pulse formation [46], as the cat ears get pulled away from the pulse. Ghost pulses are an important cause of ISI in nonlinearity limited links.
- XPM is similar to SPM, but the nonlinear phase shift is induced by the intensity variations of co-propagating signals, rather than from its own. As such, XPM can be harmful in multi-channel transmission, such as WDM transmission systems [6], being essentially a source of crosstalk. The impact of XPM becomes greater with increasing channel count and, in a dispersive fibre, decreases when increasing channel spacing (as pulses effectively 'walk past' each other) [6].
- FWM is an effect that creates new frequency components from the interaction between two or more waves [6]. The efficiency of FWM depends upon phase matching. This requirement essentially represents the condition of momentum conservation and depends upon the propagation constants of the waves involved [6]. Once this phenomenon occurs, the adjacent signals will be interfered (crosstalk) and hence the signal quality is degraded. FWM can

generally be suppressed by increasing dispersion and becomes more severe with decreasing channel spacing (owing to improved phase matching).

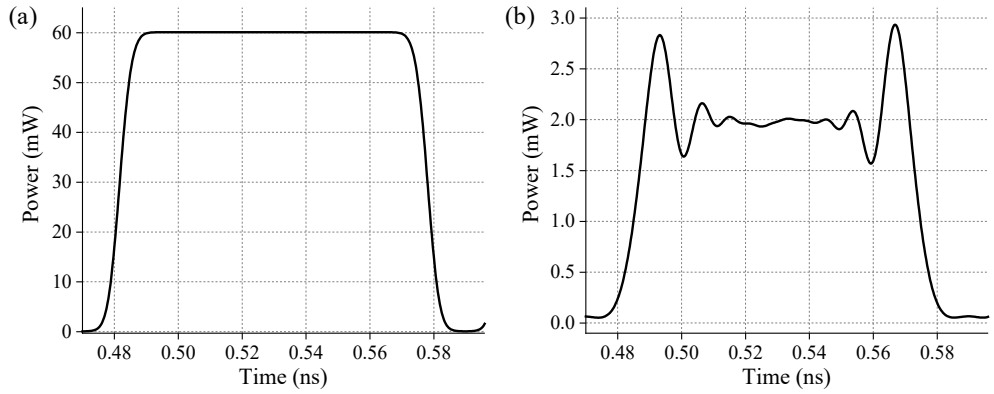

Figure 2-3: Illustration of the distortion of a pulse due to SPM and dispersion. See the details of this simulation in Section 6.4.2.

There are other nonlinear effects present in optical fibres that are not encapsulated in the NLSE presented in Equation 2-2, for example:

- Stimulated Raman Scattering (SRS): An inelastic scattering effect involving the creation (or annihilation) of optical phonons in the medium. Aside from its use in amplifiers, SRS mainly effects ultra-broadband transmission where power can move from one band to another.
- Stimulated Brillouin Scattering (SBS): An inelastic scattering effect involving the creation (or annihilation) of acoustic phonons in the medium. For telecoms, the most commonly encountered challenge induced by SBS is scattering of the carrier of a non-carrier-suppressed signal.

Note that there are other nonlinear effects, the details of which are beyond the scope of this thesis, but can be found, for instance, at [31].

The most basic solution to avoid nonlinear effects in optical transmission is to regulate the launch power such that nonlinearities have little impact on the transmission, essentially striking a balance between linear impairments (particularly the loss) and nonlinear impairments. Adopting some special formats, such as partial-response signalling and probabilistic shaping, has been demonstrated to improve the signal tolerance against the nonlinear effects [41]. Furthermore, there are several active nonlinear mitigation techniques. For instance, optical phase conjugation (OPC) which works by optically conjugating the phase of the entire transmission band in the middle

of a span, so that the further nonlinearity in the second span undoes the nonlinearity of the first [15]. This idea of implementing an 'inverse' nonlinear effect or pre-distortion is also realised in the digital domain, i.e., using DSP, through digital back propagation [47].

2.2 Nature of O-band Transmission

Now that the physical phenomena in optical transmission have been described, this section will discuss the parameters typical of SSMF in the O-band and compare them to the most commonly used band in amplified telecommunication links, the C-band.

We start with one of the most notable characteristics of the O-band, its near-zero dispersion (see Figure 2-1 for the denoted regions of dispersion for the O- and C-bands for comparison). Operating in the O-band offers a greatly reduced or even eliminated requirement for dispersion compensation for a given reach compared to the C-band. This can help reduce the overall system cost by reducing the number of dispersion compensating elements required or, if dispersion compensation is performed digitally, reducing the complexity of the receiver (for example, enabling the use of a lower memory depth compared to C-band equivalent).

Nevertheless, the reduced fibre dispersion in the O-band compared to the C-band could result in more severe nonlinear impairments (particularly from FWM), especially near the zero-dispersion wavelength. According to numerical studies in [41], for a 40Gbit/s OOK signal, systems are FWM limited when their CD is lower than ~1.4ps/(nm·km) (intra-channel XPM becomes dominant for CD greater than this). This value could be taken as an estimate for the lowest tolerable CD, although further study is required. It is interesting to note that, in real fibre, fluctuation of the zero-dispersion wavelength can broaden the wavelength region over which nonlinear distortion is intolerable [48] and so it can be difficult to provide a general analysis of the effects of dispersion on nonlinear distortion in a WDM band.

The SSMF exhibits a 20% higher nonlinearity coefficient in the O-band than in the C-band which will make the effects of SPM, XPM, and FWM worse. The efficiency of FWM can be expected to be increased due to the lower dispersion of the O-band, which could cause more crosstalk in the transmitted signal. On the other hand, Raman amplification is more efficient in the O-band compared to the C-band, as reported in [49].

The higher attenuation of the O-band in SSMF (~0.3dB/km compared to ~0.2dB/km in the C-band) will tend to favour a higher launch power, however, this will be in tension with the increased nonlinear susceptibility of the O-band. Hence, high gain and low noise optical amplification can be expected to be particularly valuable for O-band transmission.

2.3 General Properties of Optical Amplifiers

As discussed in the previous section, increased loss represents perhaps the biggest challenge of the O-band relative to the C-band, implying the need for high performance optical amplification. This section will introduce the concepts behind some important parameters used to describe optical amplifier, notably gain and noise figure, which are typically used to determine the amplifier performance and will feature in later work in this thesis.

2.3.1 Optical Gain

The optical gain is an important parameter of any amplifier. It is the increase in in-band power caused by amplification and is commonly specified in dB, which can be expressed as:

$$G = 10\log\left(\frac{P_{sig,out}}{P_{sig,in}}\right) \qquad \text{Equation 2-7}$$

where, G is the optical gain of the amplifier.

$P_{sig,in}$ is the signal power at the amplifier input.

$P_{sig,out}$ is the signal power at the amplifier output.

A high gain is generally preferred but increasing the gain is often associated with lower bandwidth, more complicated amplification schemes, and/or higher cost. Usually, the requirement of the gain is determined by the loss of the link. If an amplifier offers insufficient gain, then multiple stages of amplification might be used. In general, the higher the saturated output power of the amplifier, the better. This not only enables a longer reach, but also helps avoid operating the amplifier under gain saturation conditions. Gain saturation occurs when a given increase in the signal power at the input of an amplifier is not met with an equal increase in power at the output of the amplifier. Gain compression is the difference between the actual gain of a saturating amplifier and its unsaturated, linear gain. Amplifiers are often parameterised by their

3-dB compression point, the amplifier input power that results in a gain compression of 3dB. If the input power is increased further, the output signal power will eventually tend towards a constant value, known as the amplifier's saturation power.

The gain offered by optical amplifiers generally depends upon the wavelength. A wide gain bandwidth is desirable to amplify a wide range of signal wavelength, as it is often parameterised in terms of its 3-dB or 6-dB bandwidth. The flatness of the gain throughout the operating band is particularly important in WDM applications. If the gain is not flat, different WDM channels will have different gain, which can accumulate along a series of amplifiers causing a substantial mismatch in received powers between the channels. The measurement of the slope of optical gain across a certain wavelength, the so-called *gain tilt*, is another commonly used parameter to indicate of the gain flatness of an amplifier [50].

2.3.2 Noise Figure

In an optical amplifier (assuming amplification with a doped-fibre amplifier or semiconductor optical amplifier), the amplification is achieved by placing the gain medium in a state of *population inversion*. There are two kinds of emission from the inverted carrier population that occur whilst the medium is in this state – *stimulated emission* and *spontaneous emission*. The former occurs when a photon stimulates a carrier to return to a lower energy level by emitting a photon of the same frequency as the stimulating photon and so can be used as a source of amplification. The latter is caused by spontaneous carrier recombination and constitutes a source of additive noise. Photons originating from spontaneous emission can go on to stimulate other excited carriers, creating what is commonly known as *amplified spontaneous emission* (ASE). This ASE is generally the main cause of SNR degradation in the amplified signal, and hence is a major factor in determining the performance of the amplifier [50] [51].

The amplifier noise figure (NF) is a figure of merit representing the SNR degradation after passing through an amplifier, which historically was originally defined in the electrical domain for RF devices, before being extended to optical devices. Therefore, the parameter is measured through the (electrical) SNRs, defined as:

$$NF = 10\log(F) = 10\log\left(\frac{SNR_{in}}{SNR_{out}}\right)$$ Equation 2-8

where, F is the noise factor of the amplifier, $F = \frac{SNR_{in}}{SNR_{out}}$.

SNR_{in} is the input SNR of the amplifier.

SNR_{out} is the output SNR of the amplifier.

For an optical amplifier, a photodetector has to be used to determine its input and output SNR. It is illustrative to consider the diagram shown in Figure 2-4 for a fundamental measuring scheme by which NF can be defined.

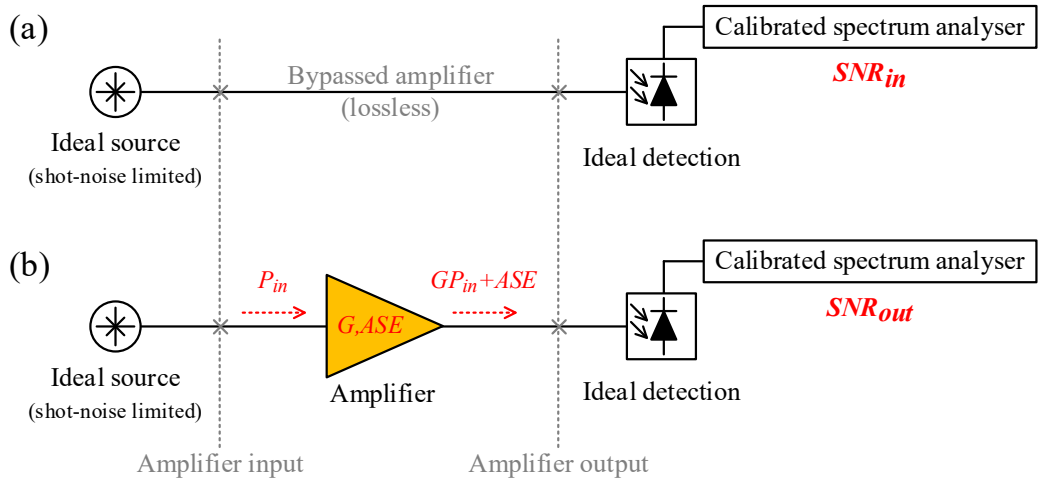

Figure 2-4: Schematic diagram for optical amplifier NF measurement with ideal source and ideal detection of (a) input SNR and (b) output SNR.

Preferably, there would be no excess optical noise appearing at the input of the amplifier if an ideal source was used. This means that the noise at the input is only from the quantum noise of the photodetector used to detect the signal. In other words, the input SNR is determined by the shot noise produced within the photodetector. The electrical power of the detected input signal (S_{in}) and the total shot-noise power ($N_{shot,in}$) are described by Equation 2-9 and Equation 2-10, respectively [50].

$$S_{in} = (\mathcal{R}P_{in})^2 Z \quad \text{Equation 2-9}$$

$$N_{shot,in} = (2q\mathcal{R}P_{in}B_e)Z \quad \text{Equation 2-10}$$

where, $\mathcal{R}$ is the responsivity of the photodetector.

P_{in} is the input power into the amplifier.

Z is the impedance of the photodetector.

q is the electron charge (1.602×10^{-19} coulombs).

B_e is the electrical bandwidth of the photodetector.

Therefore, the input SNR of an optical amplifier can be written as:

$$SNR_{in} = \frac{S_{in}}{N_{shot,in}} = \frac{(\mathcal{R}P_{in})^2}{2q\mathcal{R}P_{in}B_e} = \frac{\mathcal{R}P_{in}}{2qB_e} \quad \text{Equation 2-11}$$

At the output of the amplifier, the signal detected by an ideal, linear photodetector (neglecting thermal noise) contains three noise sources [50] [51]:

- shot noise,
- signal-spontaneous beat noise, and
- spontaneous-spontaneous beat noise.

The spontaneous-spontaneous beat noise term can be neglected if an appropriately narrow optical bandpass filter is placed before the photodetector. In that case, the output SNR can be determined by the shot noise and the signal-spontaneous beat noise. The electrical power of the detected output signal (S_{out}) is given in Equation 2-12. The detected electrical power of the noise terms: the total shot-noise power ($N_{shot,out}$) and the signal-spontaneous beat noise (N_{sg-sp}) are described in Equation 2-13 and Equation 2-14, respectively [50].

$$S_{out} = (\mathcal{R}GP_{in})^2 Z \quad \text{Equation 2-12}$$

$$N_{shot,out} = (2q\mathcal{R}GP_{in}B_e)Z \quad \text{Equation 2-13}$$

$$N_{sg-sp} = 4\mathcal{R}^2 GP_{in}(n_{sp}hv(G-1)B_e)Z \quad \text{Equation 2-14}$$

where, n_{sp} is the spontaneous emission factor, and $n_{sp} = \frac{\sigma_e N_2}{\sigma_e N_2 - \sigma_a N_1}$ where N_1 and N_2 are ground state and excited state population, respectively. σ_e and σ_a are stimulated emission and absorption cross-section, respectively.

h is the Planck constant ($6.626 \times 10^{-34}\ \mathrm{J \cdot Hz^{-1}}$).

v is the optical frequency of the signal.

Therefore, the output SNR of an optical amplifier is given by:

$$SNR_{out} = \frac{S_{out}}{N_{shot,out} + N_{sg-sp}} = \frac{\mathcal{R}GP_{in}}{2qB_e + 4\mathcal{R}n_{sp}hv(G-1)B_e} \quad \text{Equation 2-15}$$

By substituting Equation 2-11 and Equation 2-15 into Equation 2-8, the NF can therefore be written as Equation 2-16. The labels in the equation denote the sort of noises responsible for the terms in the derived NF.

$$NF = 10\log\left(\frac{1}{2q}\frac{4\mathcal{R}n_{sp}hv(G-1)+2q}{G}\right) = 10\log\left(\underbrace{2n_{sp}\eta\frac{(G-1)}{G}}_{sg-sp} + \underbrace{\frac{1}{G}}_{shot}\right) \quad \text{Equation 2-16}$$

The term η is the quantum efficiency of the photodetector, $\eta = \frac{\mathcal{R}hv}{q}$ [50]. Since the NF of an optical amplifier should be independent of the characteristics of the photodetector used, an ideal photodetector should be assumed and the detection efficiency should be set to its maximum, $\eta = 1$ [50], and thus

$$NF = 10\log\left(2n_{sp}\frac{(G-1)}{G} + \frac{1}{G}\right) \quad \text{Equation 2-17}$$

In general, amplifiers operate with large gains ($G \gg 1$) and $n_{sp} \geq 1$ [51]. Therefore, according to Equation 2-17, the minimum NF is 3 dB which is the well-known limit 3-dB NF of phase-insensitive optical amplifiers. Even though the definition and

expression of NF is straightforward, it is difficult to predict the specific value of the factor n_{sp} in an optical amplifier, which relates to the population inversion in the gain medium and is dependent on many factors, such as wavelength, temperature, pumping topology, etc. [50] [51]. Therefore, an actual measurement is needed to determine the NF of an optical amplifier.

Furthermore, it is important to describe the specifications of the ideal source and receiver with which to perform the measurement. The ideal source should have no excess noise and be only shot noise limited, whilst the ideal receiver should have a frequency-flat response and not create any excess noise [51]. If these specifications cannot be achieved, which is more than likely in a practical setup, then various corrective terms must be measured and included when performing the NF estimation. Chapter 4 details these corrective techniques, introduces the case for a frequency-resolved measurement of NF and provides the results of some experimental measurements of the NF of a number of O-band optical amplifiers. Given that the NF of an amplifier largely determines its noise performance, it is a particularly valuable metric to determine the suitability of candidate amplifiers for use in O-band WDM transmission.

2.4 O-band Amplifier Candidates

In this section, a brief overview of technologies suitable for O-band amplification is presented. This will help to illustrate the current state of O-band telecommunications and place the BDFA in context with its competitors. Although the technology to amplify signals in the O-band has been presented since at least the 1980s [52], commercial devices have only had limited success. This is likely due to their mediocre performance and the relatively low demand for O-band amplification, given the dominance of the C-band, which, along with the L-band, occupies the lowest loss region of SSMF whilst being served by the most successful optical amplifier ever made – the EDFA.

Regarding O-band amplifiers, two different optical amplifiers were used throughout the work presented in the thesis. Firstly, a commercial O-band amplifier, an SOA, and secondly, a novel BDFA which enabled all of the experimental investigations undertaken. To place these amplifiers in the context of their alternatives, the following sections describe the main candidates for O-band amplification presented today: SOAs, Raman amplifiers, and doped-fibre amplifiers.

Note that the details such as chemical processes, fabrication, and energy states of these amplifiers are out of the scope of this thesis. The discussions related to their telecommunication applications in terms of the amplification and noise performance are the main topics for this context.

2.4.1 Semiconductor Optical Amplifiers

SOAs comprise a semiconductor material with a direct band gap, such as GaAs and InP [6] [27]. They amplify the light via stimulated emission by applying an electrical pump (the driving current) into the p-n junction of the semiconductor to excite carriers to move from the valence band into the conduction band and achieve population inversion. Figure 2-5 illustrates a simple configuration of an SOA.

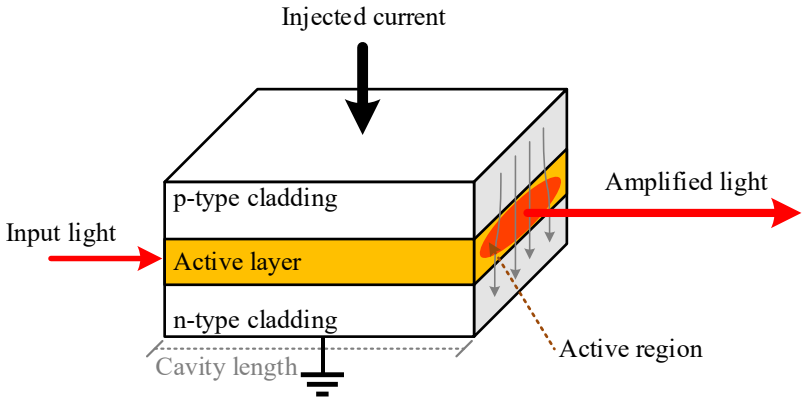

Figure 2-5: Schematic of typical SOA structure [53].

SOAs are generally fabricated using molecular beam epitaxy and etching [54]. Many of the benefits of SOAs compared to other amplifiers stem from the high degree of control that can be had over their design; SOAs can be constructed for a very wide variety of bandwidths, as large as 100nm, at present [55], offer a compact physical size (typical SOAs are only few centimetres long) and can even be built into interferometric structures, such as Mach-Zehnder interferometers for a purpose of wavelength conversion [56] [57]. Typically, the gain offered is around 20-25dB and the saturated output power is around 15-20dBm [55] [58].

Unfortunately, despite their benefits, there are in general a number of features of SOAs that limit their applications in telecommunications, specifically in terms of noise and nonlinearity. Firstly, due to the high refractive index contrast between a typical SOA waveguide and silica, internal reflection from the end facets of an SOA can be considerable, essentially forming a Fabry-Perot cavity and inducing noise through

repeated interference [6]. Given the slab structure of the active region of general SOAs, as can be seen from Figure 2-5, SOAs often exhibit a reasonably strong polarisation sensitivity which can be as much as 5–8dB between orthogonal polarisations [6], unless special design steps are taken [59].

Another important feature of SOAs that contributes to several phenomena observed in this thesis is their short carrier lifetime (<1ns) (which compares poorly to the ~10ms typical of EDFAs) [6]. This is because there are many permitted electronic transitions within an SOA that allow an electron to move from its excited state in the conduction band back into the valence band, (meanwhile rare-earth-doped amplifiers often rely on weakly allowed transitions and hence possess much longer carrier lifetimes [60]). The term '*carrier lifetime*' (τ_c) represents the total recombination time of the carriers or equivalently, the decay time of the upper-state populations due to the unavoidable spontaneous recombination in the absence of stimulated recombination. In other words, the shorter the carrier lifetime, the higher the spontaneous emission. Therefore, this relatively short carrier lifetime of SOAs is, in combination with the loss due to internal reflection, the main factor contributing for their comparatively high NF [6]. Beyond this, the short carrier lifetime is also largely responsible for the nonlinear behaviour of SOAs, which will be discussed in more detail later in Section 2.4.1.1. Currently available, commercial O-band SOAs generally meet the description described above. They are the most popular commercial O-band amplification solution, likely owing to their relatively low cost and compact size (relevant to the high volume/low-cost nature of the short-haul and inter-datacentre links the O-band often deployed in).

In the investigations presented in this thesis, the O-band SOA used is a commercial product from Thorlabs, model number: **BOA1036S** [61]. Referred to as a 'Booster Optical Amplifier' by the manufacturer, it is based on InP/InGaAsP with a quantum well layer structure and is designed to be able provide a high gain (20-23dB) and high saturated output power (~15dBm), with an operating bandwidth from 1330nm to 1370nm. The gain spectrum of the SOA is provided in Figure 2-6. A standard 14-pin butterfly package with an integrated thermoelectric cooler (TEC) and thermistor is used with this SOA. Figure 2-7 shows the SOA when mounted onto the laser-diode platform during an actual experiment. Further characterisation of this SOA will be provided and discussed in Chapter 3 and Chapter 4.

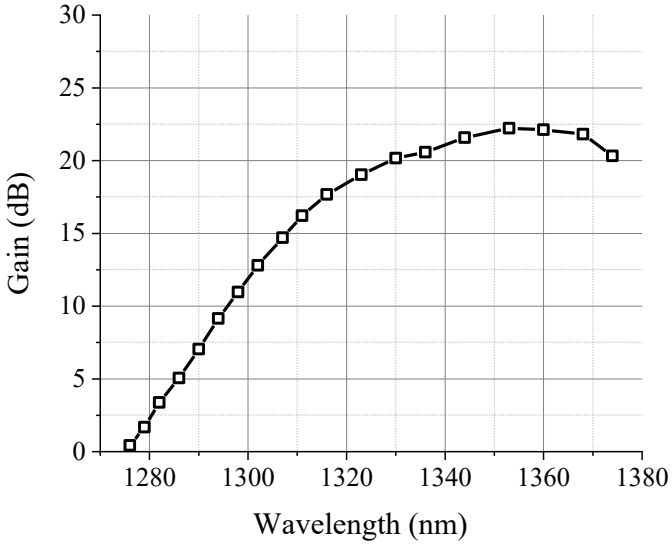

Figure 2-6: Gain spectrum of the O-band SOA used in the work in this thesis. The gain was measured at the input power of -20dBm and the operating current of the SOA was 680mA.

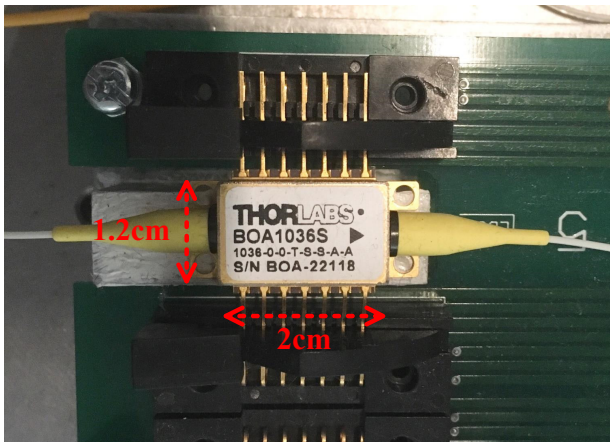

Figure 2-7: The O-band SOA used to perform the work presented in this thesis.

2.4.1.1 Carrier Dynamics in SOAs

Before moving on, it is illustrative to discuss the carrier dynamics in SOAs in more detail here, as it provides insight into the origin of the nonlinear behaviour of SOAs. Furthermore, despite doped fibre amplifiers being optically pumped (as opposed to the electrical pumping of SOAs), the effects of carrier dynamics on gain recovery are nonetheless very similar (albeit mathematically more complicated) and provide an answer as to why doped fibre amplifiers generally outperform SOAs in terms of nonlinearity.

Considering the event of an optical pulse passing through the SOA, the fast response of the SOA can cause the different parts of the pulse to experience a different gain, as illustrated in Figure 2-8 (a) and (b). In the scenario shown, the leading edge receives the most gain, whilst the increasing power of the pulse rapidly depletes excited carriers or carrier population (see Figure 2-8 (c)), leading to gain saturation. The peak of the pulse leaves the gain medium heavily saturated, which results in the trailing edge of the pulse receiving much less gain than the leading edge. The gain can be seen to slowly recover after the peak of the pulse has passed, and this is due to the interaction between the constant pump current and the amount of spontaneous emission occurring (which is affected by the carrier lifetime). Consequently, the spectrum of the amplified pulse will become broader than the input, taking on an asymmetric shape with the peak shifted toward the red side of the band [6].

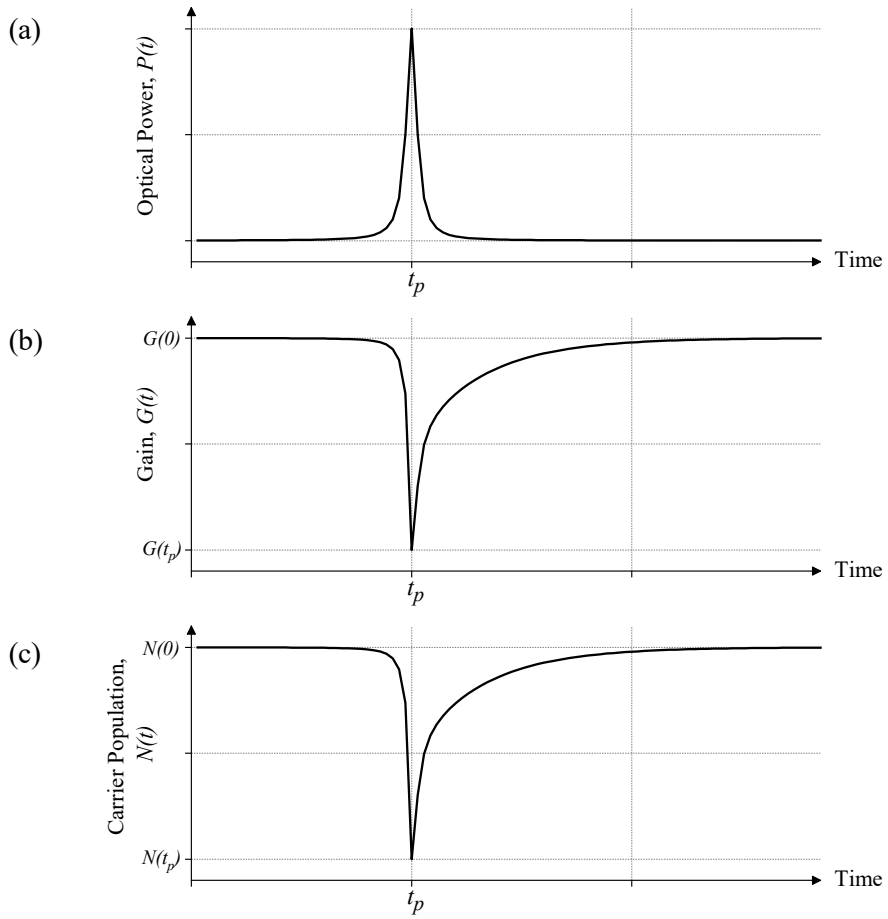

Figure 2-8: Illustration of the reaction of the SOA when the input is an optical short pulse: (a) input short pulse, (b) gain recovery, and (c) carrier population recovery [32].

The described process is governed by the population of excited carriers in the conduction band of the SOA, which influences not only the available gain, but also the refractive index of the medium [32]. Hence, a pulse in an SOA can experience both a saturation-induced *self-phase modulation* and *self-gain modulation* [32] [62].

In an SOA, the rate of change in the excited carrier population can be described by the equation below [6]:

$$\frac{dN(t)}{dt} = \underbrace{\frac{I}{q}}_{\substack{carrier\\ pumping}} - \underbrace{\frac{N(t)}{\tau_c}}_{\substack{spontaneous\\ recombination}} - \underbrace{\frac{\sigma_g(N(t)-N_0)}{\sigma_m h\nu}P_{in}}_{\substack{stimulated\\ recombination}} \qquad \text{Equation 2-18}$$

where, $N(t)$ is the carrier population.

N_0 is the carrier population required for transparency or unity gain.

I is the injection current.

σ_g is the gain cross section or differential gain.

σ_m is the cross-sectional area of the waveguide.

It is illustrative to consider how the gain of an SOA recovers after gain saturation. Considering an SOA that has just experienced deep saturation, we can assume that there are negligible numbers of excited carriers available and hence the stimulated term in Equation 2-18 can be neglected. According to R. Hui [32], the solution of Equation 2-18 in the absence of stimulated emission is:

$$N(t) = \left[N(t_p) - N(0)\right]e^{\left(-\frac{t-t_p}{\tau_c}\right)} + N(0) \qquad \text{Equation 2-19}$$

where, $N(t_p)$ is the minimum carrier population at the peak of the pulse, see Figure 2-8.

t_p is the time when the peak of the pulse occurred.

An illustration of Equation 2-19 for different lifetimes are plotted in Figure 2-9 (a). The carrier lifetimes $\tau_{c,1}$ is set to be 30 times shorter than $\tau_{c,2}$ for visualising the concept.

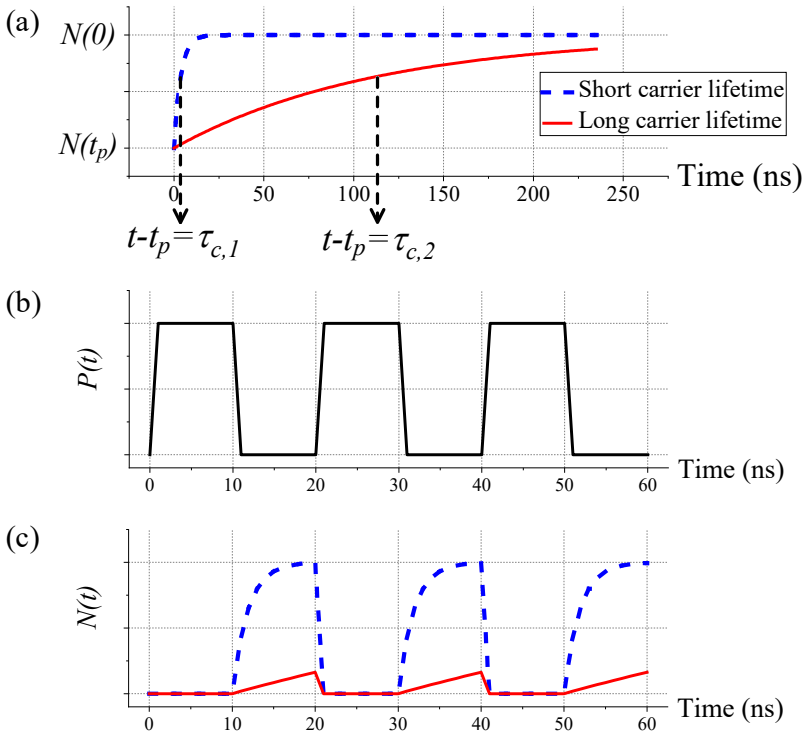

Figure 2-9: The effect of amplifier lifetime on carrier dynamics when the input signal is a square wave: (a) carrier population recovery, (b) input square wave, and (c) carrier dynamic.

Considering an optical square wave passing through the amplifier (Figure 2-9 (b)), a shorter carrier lifetime means that the population density of the excited carriers can recover more quickly compared to a longer lifetime, see Figure 2-9 (c). This effectively implies that a device with a short lifetime responds relatively quickly to changes in input power, whereas a device with a long lifetime will respond much more slowly (effectively only seeing the 'average' input optical power).

2.4.2 Raman Amplifiers

Raman amplifiers create amplification via an inelastic scattering process, stimulated Raman scattering (SRS). As briefly discussed in Section 2.1.4, Raman scattering involves an interaction between photons and optical phonons, a type of lattice vibration. The most common implementation of Raman amplification involves the scattering of a pump photon with higher frequency (energy) than the signal, to create an additional signal photon and an optical phonon. This process must naturally conserve energy before and after the scattering event and so the energy of the pump photon (E_{pump}) is equal to the sum of the energy of the signal (E_{signal}) and the energy of the generated optical phonon (E_{phonon}), as shown in Figure 2-10. The frequency

difference between the pump and the peak gain offered by typical Raman amplifiers in silica fibres is around 13.2THz [6] and is usually called the *Stokes shift* or *Raman shift*. Pumps with broad linewidths (much broader than 10-100MHz in silica fibres) are usually used to avoid stimulated Brillouin scattering (SBS) [63] [64] and the noise transfer from these pumps to the amplified signals can be mitigated by ensuring that the pumps and the signals walk past each other along the length of the gain fibre. This can be achieved, in a co-pumped scheme, using dispersion or in a counter-pumped scheme, simply by increasing the propagation length [65]. Moreover, Raman amplification exhibits a very short response time, typically around 3-6 fs [66].

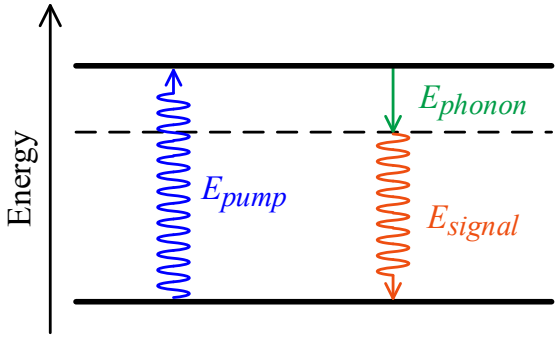

Figure 2-10: Diagram showing the change in energy level of an electron during Raman scattering.

Raman amplifiers can be split into two groups – discrete (lumped) and distributed amplifiers. The critical difference between the two is that distributed amplifiers use the transmission fibre itself as the gain medium, whilst discrete amplifiers use a dedicated gain medium. In this thesis, we only discuss discrete Raman amplifier in O-band transmissions, as these are a direct competitor to O-band SOAs and doped fibre amplifiers.

The broad bandwidth, as wide as 150nm (achieved using multiple pump wavelengths), is an important feature offered by Raman amplifiers which makes them a good candidate, especially for broadband communication applications [17]. However, a relatively high pump power is generally required for Raman amplification compared to that used in SOAs or doped fibre amplifiers. The pump power can be reduced by using a longer gain fibre, but the loss due to the intrinsic fibre attenuation will tend to increase the NF. Typically, the fibre lengths for discrete Raman amplifiers are measured in the hundreds of metres to several kilometres, whilst for EDFAs, fibre lengths are usually in the tens of metres.

Demonstrations of Raman amplification in the O-band date back at least to 1984 where a Raman amplifier with a gain of 20dB was demonstrated to amplify a 1.3µm signal [67]. Raman amplifiers are an attractive solution for O-band amplification, offering broad gain bandwidths approaching the full extent of the O-band (100nm, from 1260nm to 1360nm). The increase in Raman gain efficiency when the operating wavelength is decreased from 1550nm to 1310nm is also encouraging for its use in the O-band [49]. Gain efficiency can be increased by as much as 60% when operating in the O-band compared to in the C-band [49].

Generally, the performance of discrete Raman amplifiers can be compromised by Kerr nonlinearity effects. This is because fibres with a small cross-section core and hence a high nonlinear coefficient are often used to develop the Raman gain, in addition to the presence of high power and sometimes co-propagating pump. Even so, most of the Kerr effects can be managed by employing an appropriately designed gain fibre with carefully tailored values of dispersion and nonlinear coefficient [68] [69]. Other phenomena that contribute to noise in Raman amplification are spontaneous Raman scattering, due to optical phonons already present in the fibre, and backward or double Rayleigh scattering (DRS) [66].

2.4.3 Doped-Fibre Amplifiers

The gain mechanism in a doped fibre amplifier is similar to that of SOAs, as it creates optical gain based on stimulated emission from excited carriers. In contrast to SOAs, a doped-fibre amplifier, as its name suggests, uses a doped fibre as a gain medium and, as opposed to the electrical pumping of the SOA, they are optically pumped. The amplifier characteristics are mainly determined by the specific dopants used, although the glass host used (typically a silica-based fibre) can also have an effect. There are several elements used for doping the silica-based fibre to realise the gain ranging from $0.5\,\mu\mathrm{m}$ to $3.5\,\mu\mathrm{m}$. Most of the elements are rare-earth metals, for instance: praseodymium (Pr), neodymium (Nd), erbium (Er), thulium (Tm), and ytterbium (Yb). A main benefit of doping with rare-earth elements is the very long carrier lifetime, often a few milliseconds, which derives from the reliance on weakly allowed transitions for spontaneous emission [60]. As a result of the slow gain dynamics, distortion effects such as cross-gain modulation and patterning are largely insignificant in doped-fibre amplifiers, leading to its compatibility with high speed WDM systems.

Since the gain centres of the amplifier made of the dopant are scattered throughout the fibre, the populations in the ground and excited states (N_1 and N_2) fluctuate along the fibre length, being dependent upon the local signal and pump powers. Therefore, the spontaneous emission factor n_{sp} is considered to be averaged throughout the fibre [6]. The NF of doped-fibre amplifiers therefore depends upon the amplifier's fibre length and the pump power. The fibre length for typical EDFAs is usually in the 10's of meters. Given the long length of doped fibres, backscattering of ASE can degrade the amplifier efficiency, competing for gain with the signals, but backscattering is generally less of an issue than that occurring from the end facets of an SOA. Signals scattered backwards into the fibre can similarly create issues by depleting pumps and modulating signal gain, although this can typically be resolved by using an optical isolator at the output of the doped fibre (note that this solution may not be compatible with amplifiers in a double-pass configuration).

A few rare-earth metals offer gain in the O-band region, namely, neodymium [26] [70] and praseodymium [26], with the latter having some limited commercialisation. Whilst gain in the O-band region has been demonstrated in neodymium, performance is usually poor, with limited gain (4-5dB between 1310nm and 1370nm [70]), and a phenomenon called excited state absorption drastically limits gain when attempts are made to amplify at lower wavelengths in the O-band [71]. Additionally, a newly designed NDFA was developed to offer gain (reaching 30dB) for E-band amplification, mainly due to reduction in mode field diameter of the gain fibre [72]. The Praeseodymium doped-fibre amplifier (PDFA) is notable for offering gain across the 1270nm to 1330nm wavelengths [73], the most commonly used wavelengths in O-band communication [74]. Unfortunately, it also possesses a large phonon energy meaning that excited states can be effectively quenched through the production of multiple phonons, unless special host glasses are used (such as fluoride glass), which may be more difficult to handle than general silica fibre. This can reduce the gain and efficiency of the amplifier. Praeseodymium doped fibre amplifiers have been demonstrated with a bandwidth of 26nm (for and input signal power of -30dBm), a peak gain of 24dB and an NF of 6.5dB (for an input signal power of -20dBm) [75].

2.4.3.1 Bismuth-Doped Fibre Amplifiers

Unlike the previously mentioned dopants, bismuth is not a rare earth metal, but is rather a pnictogen or post-transition metal. By varying the composition of the glass

host, such as pure silica, aluminosilicate, phosphosilicate, and germanosilicate, and correctly selecting the pump wavelength, operating wavelengths ranging from 0.6μm to 1.7μm have been demonstrated in several designs of BDFA [76] [77] [78].

An important challenge in designing BDFAs so far is the nature of bismuth luminescence, which strongly relies on the fundamental structure of the bismuth active centres (BACs), rather than the total bismuth concentration in the fibre [76] [79] [80]. BACs can be activated through thermal treatment, with the outcome depending upon the temperature, dwell time and cooling rate [81]. The higher the temperature and the dwell time, the higher the thermal bleaching of BACs becomes [80]. It has been reported that the thermal activation of BACs could result in an increase in oxygen deficient centres (ODCs) which might then change the valency of bismuth ions in the BACs [76] [80]. This dependence on thermal processing can lead to some complexities of BDFA for fibre length optimisation, fabrication, and reproduction.

The first demonstration of a BDFA for O-band operation was presented in 2009 [19]. Before that, since the 1990s, early implementations of BDFAs were widely performed with fluoride glass hosts, as with praseodymium and neodymium [26] [70]. However, several drawbacks of fluoride glasses, including their fragility, limited chemical stability and cost have limited their practicality and cost effectiveness [52]. To date, many demonstrations of BDFAs have proven the amplifier to be a promising low-noise amplification solution for wavelengths around 1.3μm and one that may finally prove analogous to the ubiquitous EDFAs of the C-band. For instance, a BDFA with a phosphosilicate glass-host, offering gain in the O-band between 1300nm and 1340nm, was first demonstrated in 2009 [19] with a maximum gain of 24.5dB, using a single pump in a forward pumping scheme. A BDFA that was designed to operate within the commercially used region of the O-band was presented in [30] with careful selection of the pump wavelength in a simple, single-pump BDFA enabled a maximum gain of 19dB across a window of 1272-1310nm and a 5.5-dB NF was realised. This amplifier used 80-m bismuth-doped fibre. Another BDFA operating within the E-band and offering a 37-nm 3-dB bandwidth using a counter-pumping scheme at 1310nm was presented in [20].

2.4.3.1.1 Bismuth-Doped Phospho-Silicate Fibre Amplifier

This section is to provide the details of the O-band BDFA being investigated in this thesis. It is an in-house built amplifier and was firstly presented in [28]. A schematic

of the amplifier is shown in Figure 2-11. The amplifier contains a 150-m long bismuth-doped phosphosilicate fibre. This BDF has a background loss of ~14.6dB at 1550-nm wavelength and is readily spliced to SSMFs with the typical splicing loss of ~0.3dB at 1550-nm wavelength. The amplifier is bidirectionally pumped by laser diodes (LD) at two different wavelengths (1240nm and 1267nm) to broaden and flatten the gain spectrum [79]. The total pump power is 720mW. WDM multiplexers/demultiplexers are placed at each end of the gain medium to couple/decouple the signal. Optical isolators (ISOs) are used to control the propagation direction and prevent any backpropagation and reflection created within the amplifier.

The gain spectrum of the BDFA is provided in Figure 2-12 and shows that the amplifier has a 5-dB bandwidth between the wavelength of 1320nm and 1370nm (the range over which transmission was performed) of ~8.3THz. The BDFA has a peak gain of more than 25dB and a saturated output power of ~16dBm. The operating wavelength region of the BDFA was determined by the pump wavelengths, and these were chosen to extract the highest gain possible from the fibre [28]. Delivering gain around the more commonly used wavelength of 1310nm could have been achieved through an appropriate selection of pump wavelength, but would have resulted in reduced gain in the sample studied (although other BDF samples might have different characteristics). It is important to note that, because SSMF typically has its zero-dispersion wavelength around 1310nm, operating around a wavelength of 1310nm could result in greater penalty due to FWM compared to the wavelength region studied in this work [41] [48], but this benefit was incidental. Figure 2-13 shows the BDFA when fully boxed assembly for using in the actual experiments.

Recently, it has been demonstrated that the gain bandwidth of this O-band BDFA can be broadened to cover substantial parts of both the O- and E- band regions, as reported in [18].

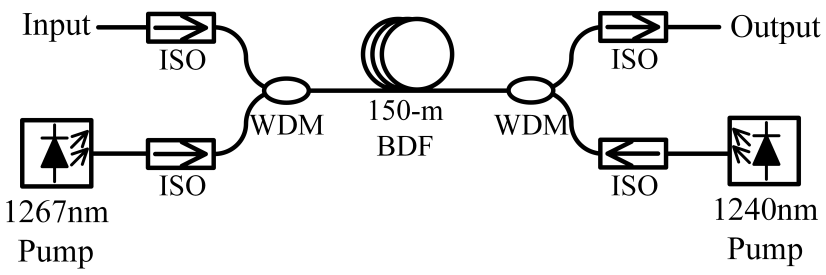

Figure 2-11: Configuration of the in-house built BDFA.

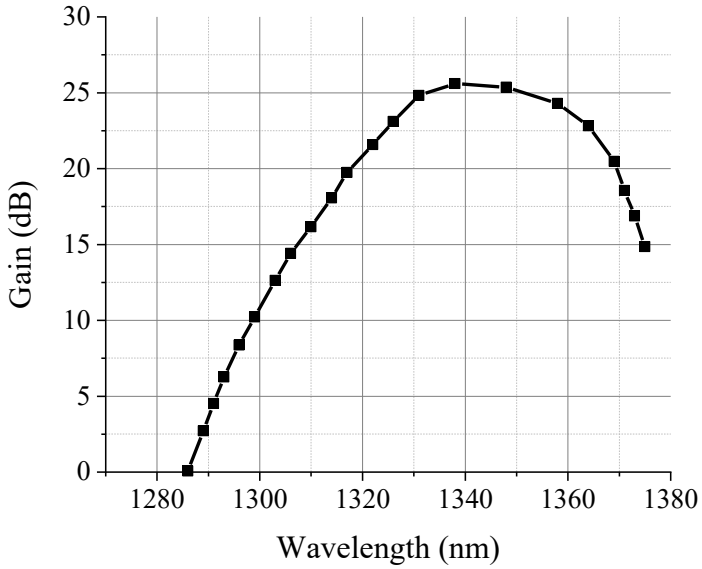

Figure 2-12: Gain spectra of the BDFA used in the work presented in this thesis. The gain was measured at an input power of -20dBm and the total pumping was 720mW.

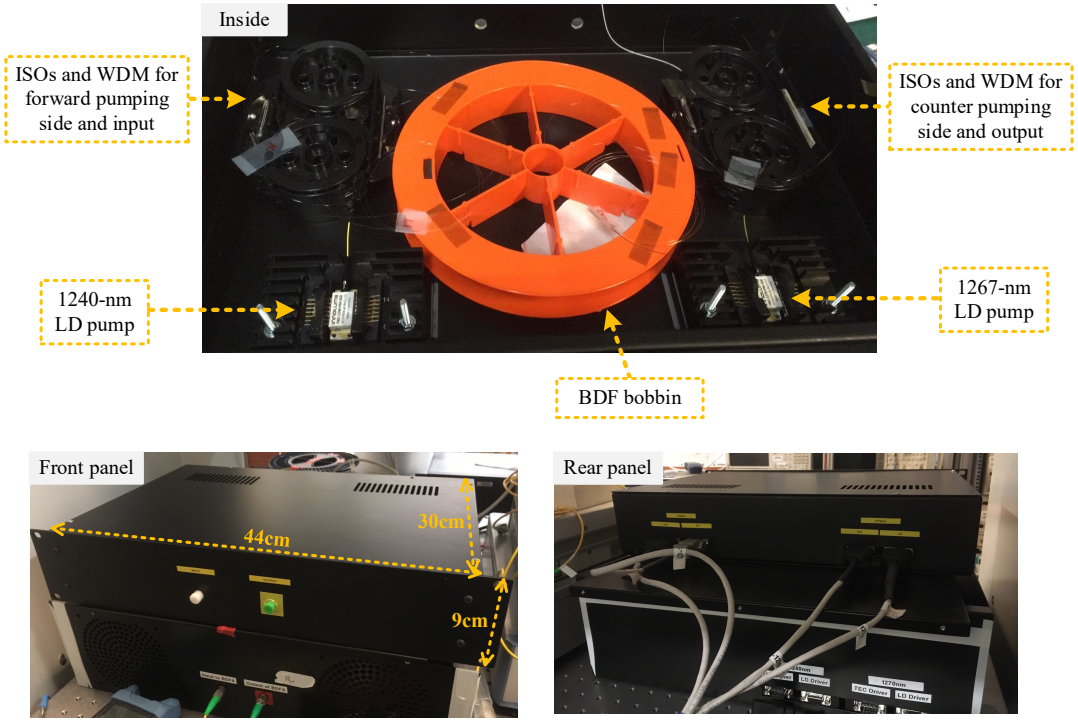

Figure 2-13: A fully boxed, in-house built BDFA.

As the discussion provided in this section has shown, the BDFA is a promising amplifier which may offer advantages relative to the currently available alternatives, such as the SOA and PDFA, in terms of the NF and nonlinearity. As detailed throughout this background chapter, there are a number of characteristics of an optical amplifier which determine its suitability for use in transmission systems.

Considering if the BDFA is to be adopted as the standard O-band amplifier, it will be important to understand its performance concerning these characteristics and to test its operation in realistic transmission systems.

2.5 Conclusion

In this chapter, the concepts necessary for the presentation of the work carried out in this thesis have been presented and discussed.

The chapter began by introducing the various linear and nonlinear impairments that a signal is subject to during propagation in an optical fibre and discussing some commonly used solutions to overcome them. The discussion was restricted to the phenomena of foremost relevance to the experimental work of this thesis – fibre attenuation, CD, nonlinearity (SPM, XPM, and FWM) and these effects were connected to their corresponding terms in the nonlinear Schrödinger equation. Afterwards, the specific characteristics of the O-band were described. This band is notably different to the C-band (the main region of WDM communications), owing to its higher loss and its low CD in SSMF. It will be essential to understand these transmission impairments to discuss some observations made in O-band transmission studies presented in this thesis in Chapter 5 and Chapter 6.

Afterwards, we introduced some general properties of optical amplifiers, covering the concepts of optical gain and NF. Although, the details of the former are quite brief, more advanced gain concepts will be discussed in the gain characterisations presented in Chapter 3. The discussion of NF in the background section covered its fundamental concepts from a theoretical perspective. In Chapter 4, these concepts will be connected to parameters that are more practical to measure to enable the measurement of frequency-resolved NF on real devices.

We then moved on to introduce three types of optical amplifiers that have been proposed and/or demonstrated for use in O-band telecommunications, namely SOAs, Raman amplifiers, and doped-fibre amplifiers. The operating principles of these amplifiers were briefly described, along with their notable characteristics, such as the effect of carrier dynamics or pump-RIN transfer, to aid a comparison between them. The discussion provided will be beneficial for understanding the work presented in the rest of this thesis (e.g., gain and NF characterisations in optical amplifiers and amplified O-band transmission demonstrations).

Finally, the chapter closed with a detailed description of the O-band BDFA, which might enable the O-band to become eligible for modern, long-haul WDM transmission. The BDFA presented will be used in every chapter of this thesis; its gain characteristics are studied in Chapter 3, followed by in depth NF characterisation in Chapter 4, before it is applied to data transmission in Chapter 5 and Chapter 6.

Chapter 3

Gain Characteristics of Novel O-band Optical Amplifier

3.1 Introduction

The best known example of a doped fibre amplifier is the EDFA, offering gain in the S-, L- and most notably, C-band. When the EDFA was first developed in the 1980s [7], it was subject to a series of characterisations which prepared it for deployment in real-world systems over the next decades [6] [50] [51]. The recently developed O-band BDFA potentially finds itself at the same point in history as the C-band EDFA was in its early stages of development and, therefore, it will be important to undertake the same kinds of characterisation that has been performed upon the EDFA to advise future applications of the BDFA.

In this chapter, a number of fundamental characterisations are presented, namely: gain tilt (both static and dynamic), transient response, polarisation dependent gain

(PDG), and cross-gain modulation (XGM). For comparison, these measurements are repeated with other commercial amplifiers (e.g., SOA and EDFA) to offer a complete picture of the amplifier's performance. This gain characterisation will be useful when operating in WDM systems with dynamically added/dropped channels. Although the measurements in this chapter have been carried out on one particular sample amplifier, this early report is considered to be indicative of what is at least possible in bismuth-doped fibres and we can reasonably expect the performance only to improve over time with further optimisation. Note that the work presented in this chapter was reported in Publications 1 and 2 listed in the Publications as First Author section.

The organisation of the chapter is as follows: an experimental characterisation of the amplifier's gain tilt, covering both static and dynamic gain, is presented in Section 3.2. Section 3.3 discusses the measurement of transient response. The effect of XGM is presented in Section 3.4. Section 3.5 contains a PDG characterisation, and Section 3.6 provides a brief summary of the results of this chapter.

3.2 Gain Tilt

The gain provided by an optical amplifier is, in general, a function of the optical wavelength. The gain tilt refers to the gradient of the variation of gain with wavelength. A low gain tilt is preferable for in-line amplification of multi-channel WDM communication signals in order to prevent the various channels from experiencing unequal gain, which will result in performance variations across the gain spectrum. The gain tilt may be further accentuated by either adding or dropping channels, and several methods have been proposed to control/reduce its effects, such as using an out-of-band signal of controllable power [82] and using gain flattening filters [83] [84].

There are two types of gain tilt typically defined: *static* and *dynamic*. The details of which are provided in the following sections.

3.2.1 Static-Gain Tilt Concept

The *static gain tilt* (m_{st}) is simply the derivative of the amplifier's gain spectrum, as shown by Equation 3-1:

$$m_{st}(\lambda_0, P_{in}) = \frac{G_{st}(\lambda_0 + \Delta\lambda, P_{in}) - G_{st}(\lambda_0 - \Delta\lambda, P_{in})}{2\Delta\lambda} \quad \text{Equation 3-1}$$

where, $G_{st}(\lambda_0 \pm \Delta\lambda, P_{in})$ is the signal gain measured at a wavelength of $\lambda_0 \pm \Delta\lambda$, as a function of its input power (P_{in}).

The static gain tilt is therefore related to the gain flatness of the amplifier and in practice, is measured using a single input signal. In particular, the static gain tilt is most relevant to single-channel systems and has a deleterious effect on systems sensitive to the combination of chirp and gain slope [85].

3.2.2 Dynamic-Gain Tilt Concept

In contrast to the measurement of the static gain tilt, measurement of the *dynamic gain tilt* requires two waves, a large signal and a probe. The gain experienced by the small probe signal is monitored in the presence of the large signal in its vicinity, the purpose of which is to saturate the amplifier. The dynamic gain tilt can imply a change in the amplifier's population inversion state caused by the amplifier's saturation when sweeping the large signal. This is because, when the amplifier begins to saturate, its ability to maintain the equilibrium state decreases. This eventually leads to cross-gain saturation, resulting in gain fluctuations on the small signal. The dynamic gain tilt (m_{dy}) is calculated from Equation 3-2:

$$m_{dy}(\lambda_0, P_h) = \frac{G_{sm}(\lambda_0 + \Delta\lambda, P_h) - G_{sm}(\lambda_0 - \Delta\lambda, P_h)}{2\Delta\lambda} \quad \text{Equation 3-2}$$

where, $G_{sm}(\lambda_0 \pm \Delta\lambda, P_h)$ is the small-signal gain measured at a wavelength $\lambda_0 \pm \Delta\lambda$ with a holding power (P_h) of the large signal, and $\Delta\lambda$ is the measuring range.

The dynamic gain tilt is most relevant to WDM systems, particularly those which include many amplified spans wherein the effects of gain tilt can accumulate, leading to intolerable differences in channel performance.

3.2.3 Experimental Characterisation

The experimental setup used for the gain tilt measurement is shown in Figure 3-1. Two wavelength-tuneable continuous-wave (CW) lasers (laser diodes LD-1 and LD-2) were coupled together with a 3-dB coupler and followed by an optical attenuator (ATT). The signals then passed through the BDFA and were finally analysed using

an optical spectrum analyser (OSA). The mutual tuneable range of both lasers were between the wavelengths of 1260nm and 1360nm.

To perform the static gain tilt measurement, LD-2 was switched off and the measurement was repeated for various input powers (P_{in}) of LD-1. Regarding the dynamic gain tilt measurement, both lasers were switched on. The wavelength spacing between the two lasers ($\Delta\lambda$) was kept constant at 2nm, and their power difference was set to 30dB. Note that the wavelength spacing was selected appropriately to spectrally resolve the probe and the saturating signal using the OSA (which was operated with a resolution of 0.1nm). The power of the large signal (P_h) was varied (while maintaining a 30-dB power difference between the two signals) to observe the saturation behaviour of the amplifier. Consequently, the total output power of the amplifier was effectively determined only by the saturating signal.

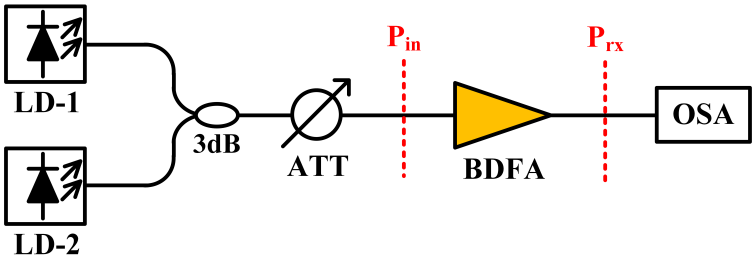

Figure 3-1: Experimental setup for gain tilt measurement.

3.2.4 Results and Discussion

The static gain tilt, measured for various input powers (-5, 0, 5, and 10dBm) into the BDFA, are shown in Figure 3-2. Note that the tested wavelengths were limited by the tunability of the CW laser. The static gain tilt decreases with increasing wavelength. The higher the input power, the broader the flat region of the static gain tilt. This means that increasing the input power can flatten the amplifier's gain spectrum, as is typical. All lines cross the 0dB/nm point at a wavelength of 1340nm, which is where the peak gain of the amplifier occurs. At even longer wavelengths, the static gain tilt becomes slightly negative (but still close to zero) as the measurement traces out the decreasing gain at the upper wavelength edge of the gain spectrum. The cluster of the static gain tilt plots around the zero line also indicates the gain flatness of the amplifier at the wavelength range 1340-1360nm. This characteristic is especially important for multi-span links where reach can be limited by an uneven band spectrum at the receiver due to accumulated gain tilt from successive amplification stages.

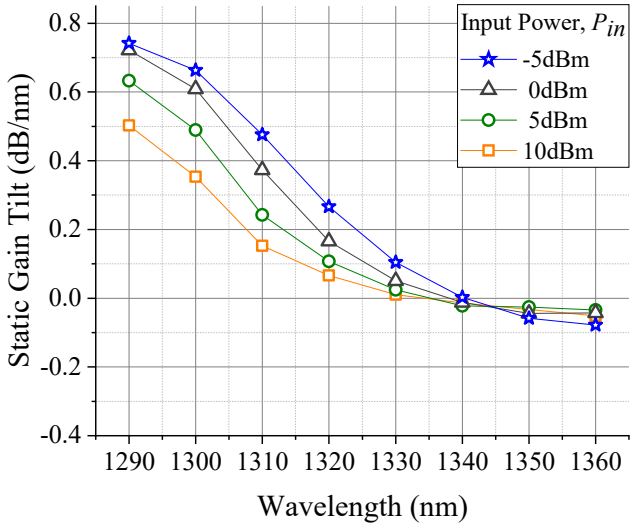

Figure 3-2: Static gain tilt results of the BDFA at various input powers into the amplifier.

Figure 3-3 shows the results of the dynamic gain tilt measurement tested at various holding powers of the (large) saturating signal. Note that the measurement points for the dynamic gain are subject to more measurement noise than for the static gain because the signal power measured in the former case is 30dB lower than the latter case. The plots of different P_h show similar behaviour in the range 1300-1320nm. However, they begin to spread out from one another in the region of peak gain (from 1330nm onwards). As the amplifier provides a maximum gain in this wavelength region, it becomes more sensitive to saturation at higher input power levels (high holding power), leading to more prominent cross-gain saturation. However, the amount of dynamic gain tilt arising in the BDFA (across the range where the gain is flattest, 1320-1360nm) is relatively low (<0.4dB/nm), which implies that the amplifier can tolerate changes in the input power, caused e.g., by adding or dropping WDM channels. Specifically, the BDFA exhibits a dynamic gain tilt of between -0.3dB/nm and 0.4dB/nm (for an input power of 0dBm) over the wavelength range 1320nm to 1360nm, which compares well to the EDFA's dynamic gain tilt of 0.6dB/nm at a wavelength of 1545nm and 0.2dB/nm at a wavelength of 1559nm for the same input power, as reported in [86].

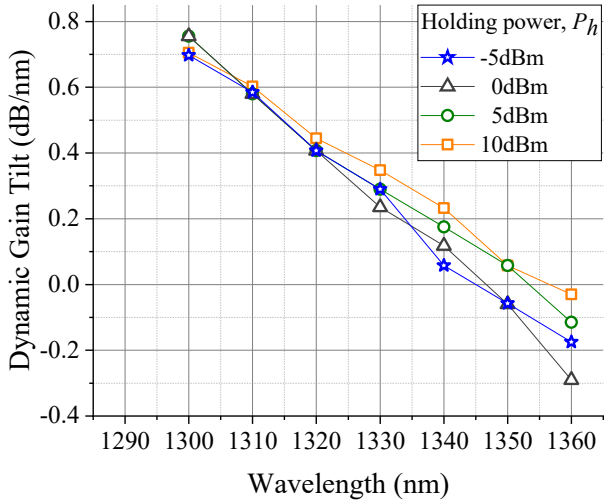

Figure 3-3: Dynamic gain tilt results of the BDFA at various holding powers of the large signal.

3.3 Transient Response

Since signals copropagating in an optical amplifier can (if the amplifier is homogeneously broadened) share the same source of gain (excited ions), a sudden change in the power of one signal can lead to a transient change in the gain of another, leading to a *transient gain response*, which may compromise the performance of the amplified signals. The response time of the process of transient response depends on the carrier lifetime of the amplifier: the shorter the carrier lifetime, the faster the response. Doped-fibre amplifiers often have a long lifetime relative to other amplifiers, such as SOAs [62] [79]. Therefore, the gain of a doped-fibre amplifier tends to vary slowly with input power. This, in turn, implies that only low-frequency variations in signal input power affect the amplifier gain and hence the signal gain only varies with the "average" signal input power. As a result, high-data rate signals do not trigger any substantial gain modulation even when operating in deep saturation.

The carrier lifetime in a typical SOA generally is <1ns, i.e., comparable to a baud rate of at least 1GBd [6] [87]. Therefore, amplifying such a signal using a saturated SOA will normally cause ISI due to patterning. In contrast, the lifetime of the BDF used in this amplifier was found in other work to be approximately 600μs [79], considerably (6×10^5 times) longer than that of a typical SOA. However, it should also be noted that the excited state of erbium-doped fibre has an extremely long carrier lifetime of ~10ms [6] [87], (at most) 20 times higher than that for the BDFA. As such,

we can expect the transient response of the BDFA to be substantially better than that of a typical SOA, but not quite as good as that of a typical EDFA. In this section we measure the transient response using a common, electro-optic technique.

3.3.1 Experimental Characterisation

Typically, the transient response can be measured from saturation-induced crosstalk on a small probe signal in a two-channel system. Note that the saturation-induced crosstalk is unaffected by the channel spacing since it is a result of decreasing the degree of population inversion or carrier density [88]. The transient response is measured by determining the power excursion of the probe signal. The setup used in this measurement is shown in Figure 3-4. As before, two laser sources were used at the transmitter. One channel at λ=1343nm was unmodulated and was used as a small probe signal. The other channel at λ=1360nm was modulated by a Mach-Zehnder modulator (MZM) with a square wave and was used as a saturating input signal with $P_{in,sat}$=5dBm. The frequency of the square wave was varied to observe the effect of the transient response. The average power ratio between the two signals was 30dB. After combining the two channels with a 3-dB coupler, they were launched into the amplifier. Then, the probe signal was selected out using an optical bandpass filter (OBPF) with an out of band optical rejection ratio of >45dB, detected using the photodetector (PD), and analysed with an oscilloscope (OSC).

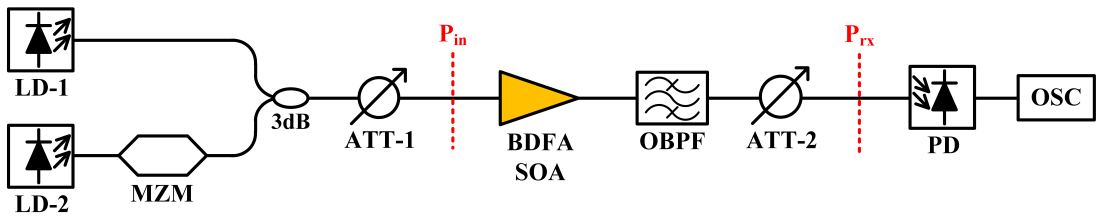

Figure 3-4: Experimental setup for transient response measurements.

3.3.2 Results and Discussion

An example of the optical signals modulated at 50kHz, as observed at the OSC after amplification in the BDFA, is shown in Figure 3-5 (a). The blue line is the amplified, saturating signal, while the orange line is the probe signal. The transient response is defined by the ratio of the maximum amplitude to the minimum amplitude of the power excursion [51], see the labels in Figure 3-5 (a). In addition, the transient response of the O-band SOA (BOA1036S, presented in Section 2.4.1) was also

measured in this section. The BDFA's and SOA's transient response results as a function of the modulation frequency (the square wave's frequency) are plotted in Figure 3-5 (b). The results show that, in stark contrast with the SOA, the BDFA's transient response noticeably drops with increasing modulation frequency, which is in accordance with the long carrier lifetime (slow response) in doped-fibre amplifiers. Specifically, the transient response of the BDFA drops below 0.5dB for a modulation speed of 150kHz (compared to ~6kHz in the EDFA, reported by [88]), whilst for the SOA, the transient response remains ~7dB, with no signs of dropping. Note that the carrier lifetime of the amplifier depends on the chemical composition of the gain medium (for instance, the dopant concentration and the host glass). Once again, the lifetime of the BDF used in this amplifier is reported in [79] as ~600μs.

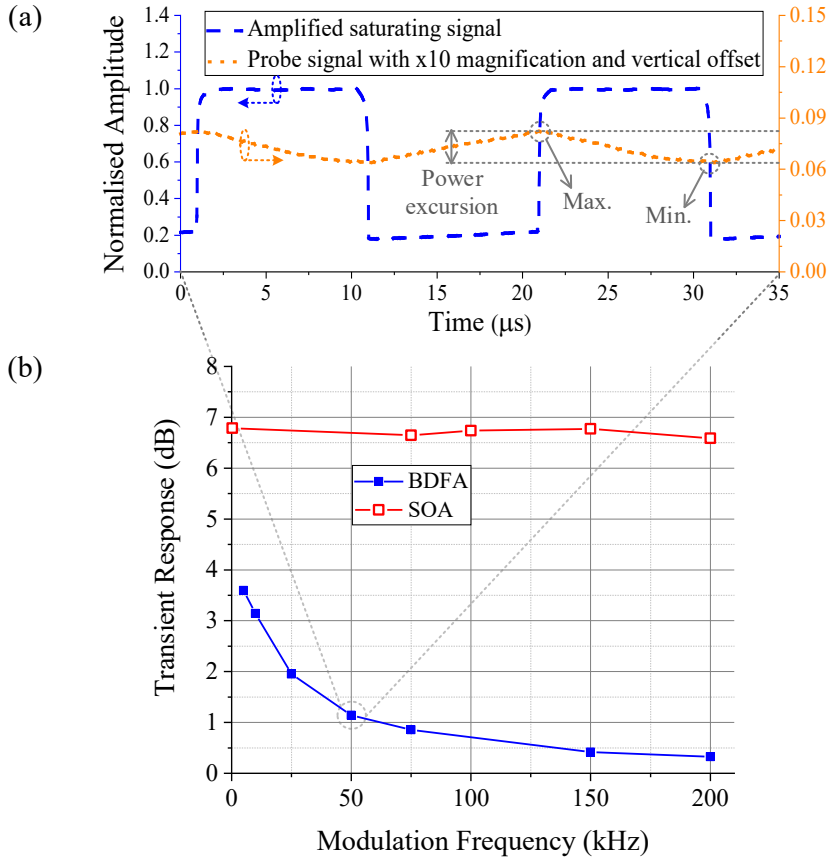

Figure 3-5: Transient response results – (a) OSC traces observed at 50-kHz modulation frequency measured in the BDFA and (b) transient response as a function of the modulation frequency measured in the BDFA and SOA.

3.4 Cross-Gain Modulation

In the previous section, the (low frequency) transient response of the BDFA was measured by launching into it a (higher powered) modulated saturating signal and a

(much lower powered) probe signal. In this section, to better emulate a WDM band, two signals of equal power, are launched into the BDFA, and the crosstalk between them is measured. We will label the cause of the crosstalk as the more generic term, *cross-gain modulation* (XGM), as, unlike the previous section, we do not identify the cause of the crosstalk.

Unlike the previous section, where one signal was modulated with a square wave, in this section we modulate one signal with a sinusoidal wave. Figure 3-6 shows the expected consequence in the presence of XGM, where the probe signal has been distorted by the modulated signal (in this case, with a π-phase shift, as is typical for many XGM phenomenon). The intensity-modulated input signal with a modulation frequency f_m at a wavelength of λ_1 and a CW probe at λ_2 are coupled and are passed into the amplifier. At the output of the amplifier, the result of XGM can be observed as two complementary intensity modulated signals at λ_1 and λ_2.

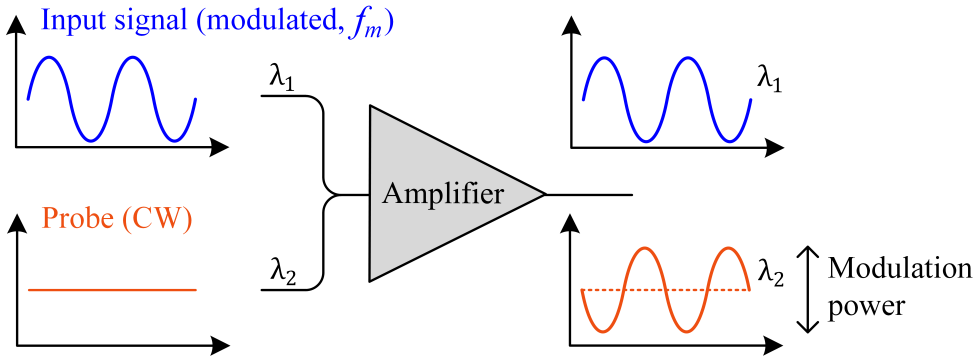

Figure 3-6: Illustration of the XGM in an optical amplifier [89].

3.4.1 Experimental Characterisation

As stated before, we characterised the XGM of the BDFA by launching into it two signals of the same average power. The experimental setup of the XGM measurement (shown in Figure 3-7) is similar to that used to measure the transient response (see Figure 3-4), but with one important difference, notably, the use of a network analyser. For our purposes, the network analyser was configured so as to be analogous to the diagram drawn within it in Figure 3-7. Effectively, a swept RF source (with frequency f_m) inside the network analyser was used both as a reference to the lock-in amplifier (within the network analyser) as well as the source to drive the MZM. At the receiver, the output of the photodiode was fed into the lock-in amplifier of the network analyser, allowing for a measurement of the power of the tone, f_m, in the photodetected signal,

relative to the power of the reference signal into the lock-in amplifier. This measurement will be labelled $Q(f)$ and measured in decibels.

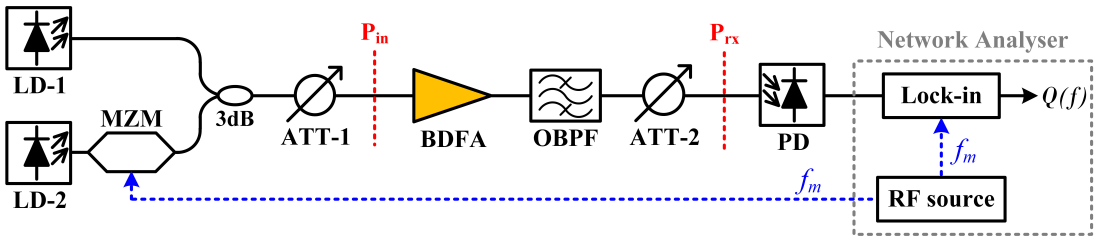

Figure 3-7: Experimental setup for XGM measurement. The blue arrows indicate the RF signal.

Using this setup, a reference measurement, $Q_r(f)$, of the modulated signal was first taken by tuning the OBPF to select the modulated signal. After tuning the OBPF to the unmodulated, probe signal, a second measurement can then be taken, $Q_d(f)$. Finally, the crosstalk induced by the BDFA was parameterised as $Q_c(f) = Q_d(f) - Q_r(f)$ (in dB).

3.4.2 Results and Discussion

The measurements were performed for two different frequency spacings between the two signals (100GHz and 200GHz) for two different input powers (-10dBm and -20dBm) and the results are shown in Figure 3-8. The results show there is little difference between the two frequency spacings tested, with only a slight increase in tonal power across the frequency range for the 100GHz measurement relative to the 200GHz measurement, possibly due to FWM or simply linear crosstalk.

Comparing the two results for the two different input powers, at higher input power, we expected to see higher sensitivity to XGM because the amplifier was operated closer to its saturation region. This expectation is largely supported, with the higher launch power of -10dBm showing much higher crosstalk, increasing with decreasing frequency, relative to the results for a launch power of -20dBm.

In all cases, the spectral crosstalk remains below -20dBm and is low frequency biased, something which supports the crosstalk originating predominantly from gain saturation effects, rather than FWM (which would be expected to have a much higher bandwidth, owing to its fast response).

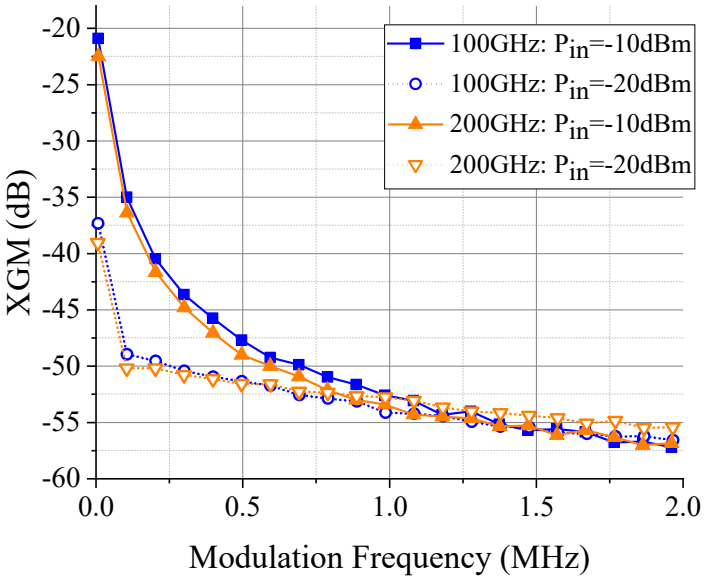

Figure 3-8: XGM results of the BDFA tested at the wavelength of 1344nm with two different channel spacings and input powers at 100GHz and 200GHz and at -10dBm and -20dBm, respectively.

3.5 Polarisation Dependent Gain

In general, optical amplifiers provide a different amount of gain on each polarisation, giving rise to the so-called *polarisation dependent gain* (PDG). Unlike SOAs, which often require the adoption of a polarisation diversity scheme in order to amplify signals of random polarisation [59], doped fibre amplifiers typically have low PDG [90] and are therefore more attractive.

3.5.1 Experimental Characterisation

The setup for the PDG measurement of the BDFA is shown in Figure 3-9. At the transmitter, one CW laser was followed by a polarisation scrambler (PolScr) with a 100Hz repetition rate, to traverse all polarisation states whilst a power meter (POW) was used to search for the maximum and minimum power of the amplified signal. The PDG was given by the difference between the maximum and minimum powers measured. Note that a comparison measurement with the O-band SOA was not performed since the SOA was designed as a single-axis device with a PDG >18dB. The polarisation dependent loss (PDL) of the measurement set-up was found to be less than 0.07dB.

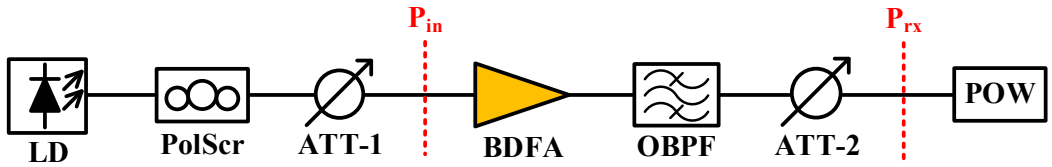

Figure 3-9: Experimental setup for PDG measurement.

3.5.2 Results and Discussion

The PDG results at a wavelength of 1350nm as a function of the input power into the BDFA are presented in Figure 3-10 (a). The PDG tends to decrease with an increase in input power. This is largely because the amplifier approaches saturation as the power increases. We also observe that the PDG of this BDFA decreases with increasing wavelength (see Figure 3-10 (b)). This could be due to a polarisation mode dispersion (PMD) induced "scrambling" of the relative polarisation states of the pumps and signal, which increases with increasing pump-signal wavelength separation [91]. The PDG from the plot is at all points less than 0.64dB.

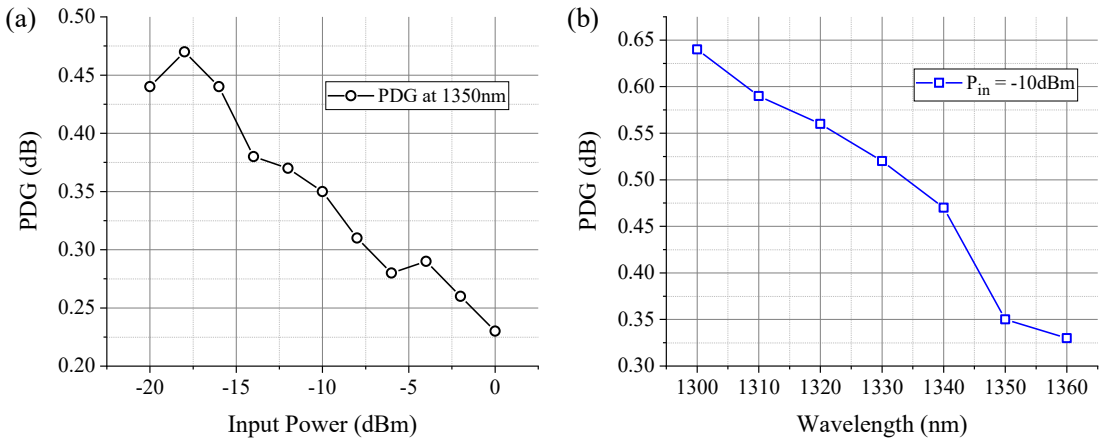

Figure 3-10: PDG results of the BDFA (a) at 1350nm with varied input power and (b) wavelength dependent PDG at -10-dBm input power. The input power was measured at the input of the amplifier, P_{in} measurement point denoted in the setup above.

3.6 Conclusion

The work in this chapter contributes to the developing, comprehensive characterisation of phosphosilicate O-band BDFAs. A set of experimental measurements was presented covering gain tilt, transient response, XGM, and PDG,

following the parameterisation of the EDFA early in its history. The BDFA was shown to have a broad flat gain region, of near-zero slope from a wavelength of 1320nm to at least 1360nm, corresponding to a frequency bandwidth of ~6.7THz. The transient response, important for understanding crosstalk in saturation conditions or power ripples due to adding and dropping channels, rapidly dropped to <1dB at modulation frequencies beyond 60kHz. A comparison has shown that the BDFA has a much slower response than a typical O-band SOA. No excess crosstalk due to XGM was observed in the BDFA, even for a channel spacing as small as 100GHz (as indicated by the induced crosstalk always being measured to be less than -20dB). In addition, our measured PDG value of this BDFA was <0.64dB across the tested wavelengths, which is in line with conventional doped-fibre amplifiers. The results of these measurements are quite promising for the application of the BDFA to WDM transmission, presented later in the thesis and for the deployment of BDFAs in real-world systems.

Chapter 4

Noise Figure Measurement of Novel O-band Optical Amplifier

4.1 Introduction

Gain and noise figure (NF) are two fundamental parameters that largely describe optical amplifier performance in an optical transmission link. Determining these parameters as they vary with wavelength, input power, and polarisation is generally sufficient to predict the linear performance of a broadband WDM link equipped with the characterised amplifier.

In Chapter 3, we discussed the gain characteristics of an O-band BDFA in terms of gain tilt, transient response, polarisation dependent gain, and cross gain modulation and in this chapter we will determine the NF of the amplifier as it varies with a number of parameters. The concept of NF was already introduced in Section 2.3.2, but methods to measure it experimentally were not detailed. In this chapter

procedures to measure NF will be described and then applied to a number of different optical amplifiers.

The NF is often measured in the frequency domain and there are several ways to measure it. The results of the measurements often depend on the capabilities of the test equipment used, in particular, the resolution bandwidth. For instance, diffraction grating based OSAs often have resolution bandwidths as low as 0.01nm (1.25GHz). As a result, optical methods based on the use of OSAs, despite their typical simplicity, cannot be used to observe noise effects that occur over bandwidths smaller than this. In contrast, electrical methods, based on radio-frequency spectrum analysers (RFSAs) can offer even Hz-level resolution bandwidths and so can be used to observe much slower effects, such as multi-path interference (Rayleigh scattering), saturation-induced patterning effects, and pump to signal relative-intensity-noise (RIN) transfer [51] [65] [92].

In this chapter, we will perform frequency resolved NF measurements via the electrical method to, firstly, determine the noise performance of the O-band BDFA and benchmark it against an EDFA (perhaps the most studied optical amplifier), as well as the commercial O-band SOA that has been studied throughout this thesis. Secondly, we perform NF characterisation on a number of other interesting optical amplifiers – namely, a double-pass BDFA and a Raman amplifier. The NF results of the last two amplifiers will clearly show the merit of using the frequency-resolved measurement (electrical method). Note that the work presented in this chapter was reported in Publications 1 and 2 listed in the Publications as First Author section.

The organisation of this chapter is as follows: a brief discussion of the methodology of NF measurements is presented in Section 4.2. It is followed by the description for the procedure to measure the NF for both the optical method and the electrical method in Section 4.2.1 and Section 4.2.2, respectively. Then, the experimental measurement results using the electrical method of several amplifiers are presented in Section 4.3. The order of the tested amplifiers is as follows: EDFA (Section 4.3.1), BDFA (Section 4.3.2), SOA (Section 4.3.3), double-pass BDFA (Section 4.3.4), and broadband Raman amplifier (Section 4.3.5). Finally, the conclusion of the NF characterisation is provided in Section 4.4.

4.2 NF Measurements: Methodology

As presented in Section 2.3.2 the NF of an amplifier can be formulated as Equation 2-17:

$$NF = 10\log\left(2n_{sp}\frac{(G-1)}{G}+\frac{1}{G}\right)$$

Although it is difficult to directly measure the spontaneous emission factor (n_{sp}), assuming that a narrow linewidth laser is used to probe the NF of the amplifier under test, the spectral power density of the ASE of the amplifier can be estimated through spectral analysis and this can be linked to n_{sp} with the following equation [50] [51]:

$$\rho_{ASE} = 2n_{sp}hv(G-1) \qquad \text{Equation 4-1}$$

where, ρ_{ASE} is the ASE power spectral density [W/Hz].

Substituting Equation 4-1 into Equation 2-17, we obtain:

$$NF = 10\log\left(\frac{\rho_{ASE}}{Ghv}+\frac{1}{G}\right) \qquad \text{Equation 4-2}$$

This equation implies that the NF of an amplifier can be determined by measuring the ASE of the output (assuming a shot-noise limited input source) and to do so, there are two commonly used methods (as discussed in Section 4.1):

- The optical method – implemented using an OSA
- The electrical method – implemented using an RFSA

Each method requires different instrumentation to complete the measurement, hence giving different features in the results, which will be described in the following sections.

4.2.1 Optical Method

The optical method is perhaps the most commonly used technique to measure the NF of an amplifier, due to its low equipment requirements and simple procedure. The measurement setup is shown in Figure 4-1. It contains a shot-noise limited CW tuneable laser diode (LD), an optical amplifier (the device under test (DUT)), and an OSA at the receiver. The input signal power (P_{in}) can be varied by using an optical

attenuator (ATT). This setup was used later in this thesis for measuring the optical NF of the BDFA in Section 4.3.2.

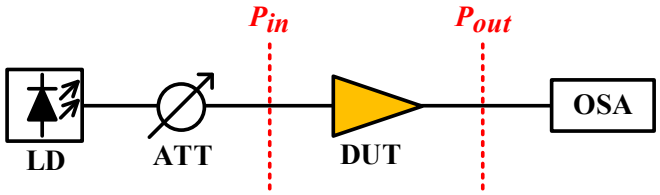

Figure 4-1: Experimental setup for the optical-method NF measurement.

To achieve an accurate optical NF measurement, the input signal optical signal-to-noise ratio (OSNR) must be high enough (>60dB [51]) to ensure that the signal power of the source is much larger than its own noise.

As an OSA is capable of performing spectral analysis on the light itself, the power spectral density of the ASE in the output of the amplifier, $\rho_{ASE} = \frac{P_{ASE}}{B_o}$ [W/Hz] (where B_o is the resolution bandwidth of the OSA) can be measured directly, as illustrated in Figure 4-2 by the label P_{ASE}. In terms of P_{ASE}, the NF in Equation 4-2 can be written as:

$$NF = 10\log\left(\frac{P_{ASE}}{GhvB_o} + \frac{1}{G}\right) \qquad \text{Equation 4-3}$$

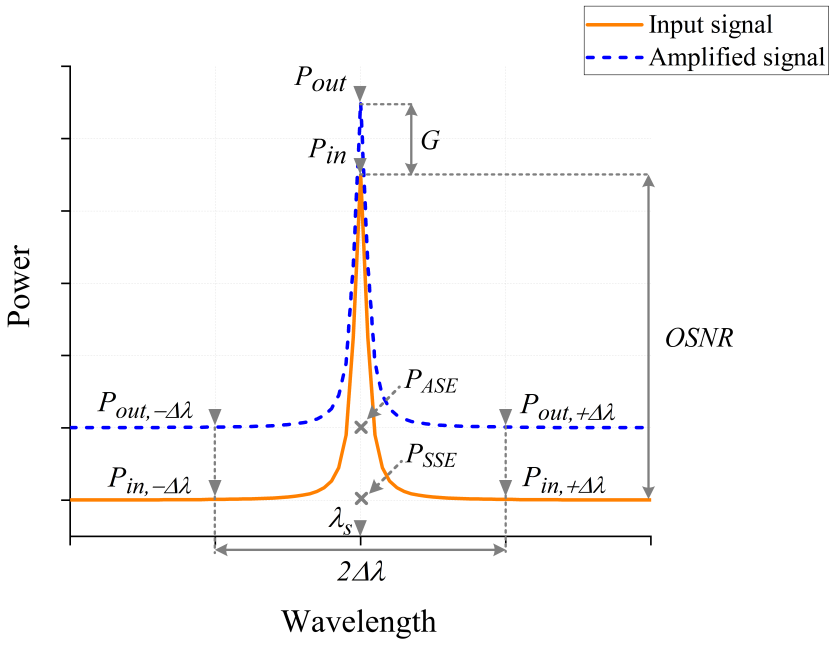

Figure 4-2: Illustration of signal spectral powers for the optical source-subtraction method. The triangles represent the measuring points, whilst the crosses denote the average points.

To perform the NF measurement, the following variables need to be obtained at the signal wavelength (λ_s): P_{in} [W], P_{out} [W], P_{ASE} [W] and ν [Hz]. It shall be assumed that the OSA has already been calibrated accurately in both power and wavelength.

To take the measurement, firstly, the laser is tuned to the frequency to be tested, ν, and the power of the laser set with the ATT to the power desired. To obtain P_{in}, the DUT is bypassed and then the peak power of the signal can simply be read with the OSA, as shown in Figure 4-2. After installing and configuring the DUT, P_{out} can be similarly obtained and the gain of the amplifier can be determined as $G = P_{out} - P_{in}$ [dB]. As can be seen from Figure 4-2, determination of P_{ASE} at the signal frequency is more complicated, since it is hidden by the power of the signal itself. Therefore, P_{ASE} is usually estimated using some form of interpolation. For instance, two points on the ASE curve, $P_{out,-\Delta\lambda}$ and $P_{out,+\Delta\lambda}$ (labelled in Figure 4-2) can be measured and the results are simply averaged to obtain an estimation: $P_{ASE} \approx \frac{P_{out,-\Delta\lambda}+P_{out,+\Delta\lambda}}{2}$.

This discussion has assumed that the laser source used is shot noise limited. However, if the laser noise is large enough that it cannot be neglected, we can apply the so-called source spontaneous emission (SSE) correction [51]:

$$NF = 10\log\left(\underbrace{\frac{P_{ASE}}{GhvB_o}+\frac{1}{G}}_{Noise\ factor} - \underbrace{\frac{P_{SSE}}{hvB_o}}_{\substack{\text{SSE}\\ \text{correction}}}\right) \qquad \text{Equation 4-4}$$

where, P_{SSE} is the SSE power, effectively the noise of the laser source.

An estimate for P_{SSE} can be obtained similarly to that for P_{ASE}, as illustrated in Figure 4-2. The power spectral density of the SSE (ρ_{SSE}) can also be determined from the OSNR (in dB) of the laser source, by $\rho_{SSE} = -10\log\left(\frac{10^{OSNR/10}}{B_{o,nm}}\right)$ where $B_{o,nm}$ is the OSA resolution bandwidth in nm. According to [51], the error in NF calculation caused by the SSE becomes negligible when $\rho_{SSE} \leq -70$dBm/nm. It is noted that the laser source used in the experiments in this thesis exhibited an OSNR of 90dB for the 0.1-nm OSA resolution, equivalent to -100dBm/nm. Therefore, the SSE correction term in Equation 4-4 was negligible.

Whilst the optical method is simple to perform and has modest equipment requirements, practical implementations generally suffer from the relatively coarse resolution of modern OSAs. This leads to an inability to determine the low-frequency

behaviour of the DUT and can cause an underestimation of its NF. Although this makes the optical method a great choice for measuring amplifiers that are known not to suffer from any low-frequency phenomena (such as excessive Rayleigh scattering or Brillouin scattering), it is unsuitable for confirming that novel amplifiers, such as the BDFA, do not suffer from any such effects.

4.2.2 Electrical Method

Electrical methods to measure NF, whilst generally being more complicated to perform and having more complex equipment requirements, can resolve the noise of an amplifier down to very low frequencies. As such, they are an appropriate choice for proving that a given amplifier does not suffer from any low-frequency phenomena that would be missed using the optical method. Given that the BDFA is much less mature than the EDFA, performing this kind of frequency-resolved NF measurement will provide a more complete characterisation.

Figure 4-3 shows the testbed that was used in this thesis for the NF measurement using the electrical method. The system consists of a shot-noise limited CW laser diode source (90-dB OSNR), followed by ATT-1 to control the input power into the DUT amplifier. At the amplifier output, an optical bandpass filter (OBPF) is used to control the detected optical bandwidth. This arrangement reduces the total spontaneous-spontaneous beat noise and ensures that the signal-spontaneous beat noise dominates the system [93]. After the DUT, another attenuator, ATT-2, is placed to control and fix the detected power at the photodetector (PD), P_{rx}. In this way, saturation of the PD can be prevented and the change in PD response between measurements can be minimised to improve accuracy. The intensity noise is then detected by the PD and the current through it (I_{PD}) measured. Subsequently, the power spectrum of the RF signal from the PD is captured and analysed by an RFSA.

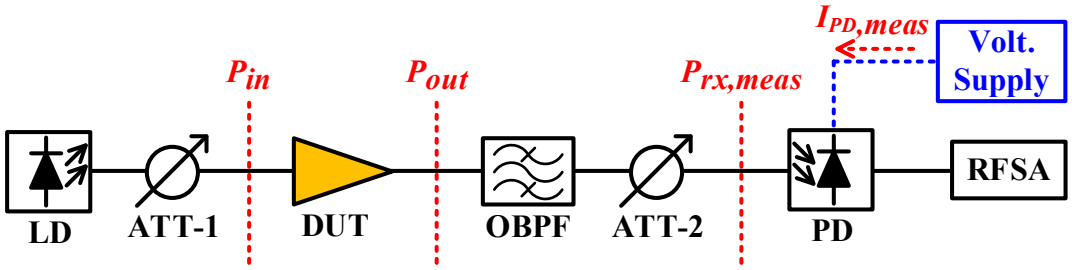

Figure 4-3: Experimental setup for the electrical-method NF measurement. The filter bandwidth used for the O-band was 1.2nm (fixed), while bandwidth of the C+L band filter could be adjusted. The subscript '*meas*' denotes the parameters obtained from the measurement.

Unlike in the optical method, the electrical method does not offer a direct measurement of the ASE. Rather, the spectrum measured by the RFSA originates from the beating between the signal and the noise. As such, a slightly different form is taken for the power spectral density of the ASE: $\rho_{ASE} = \frac{S_n(f)}{2P_{out}}$ [W/Hz] (where $S_n(f)$ is the power spectral density of optical intensity noise [W^2/Hz] and P_{out} is the amplifier output power [W]). It is noted that the factor 2 arises from the signal-noise beating at the PD. In terms of $S_n(f)$, the NF in Equation 4-2 can be expressed as, derived from [51]:

$$NF(f) = 10\log\left(\underbrace{\frac{S_n(f)}{2hvG^2P_{in}}}_{\substack{Excess\ noise\\ factor}} + \underbrace{\frac{1}{G}}_{\substack{Shot\ noise\\ factor}}\right) \qquad \text{Equation 4-5}$$

where, P_{in} is the input power of the amplifier [W].

The flat frequency response, low noise and ability of an OSA to directly measure the ASE of an amplifier mean that performing the calibration for a measurement of the NF of an amplifier is relatively straight-forward. However, the same is not true for the electrical method. A non-flat frequency response, the nature of signal-noise beating at the detector and the comparatively higher noise of electrical components mean that obtaining an accurate estimation of $S_n(f)$ requires a number of additional corrective terms to be applied to the RFSA's measurement of the amplifier emission, $S_{RFSA,meas}(f)$, an example of which is shown in 'Trace A' of Figure 4-4. We identify four corrective terms that must be applied:

- Thermal noise correction
- Loss correction
- Receiver calibration
- Shot-noise correction

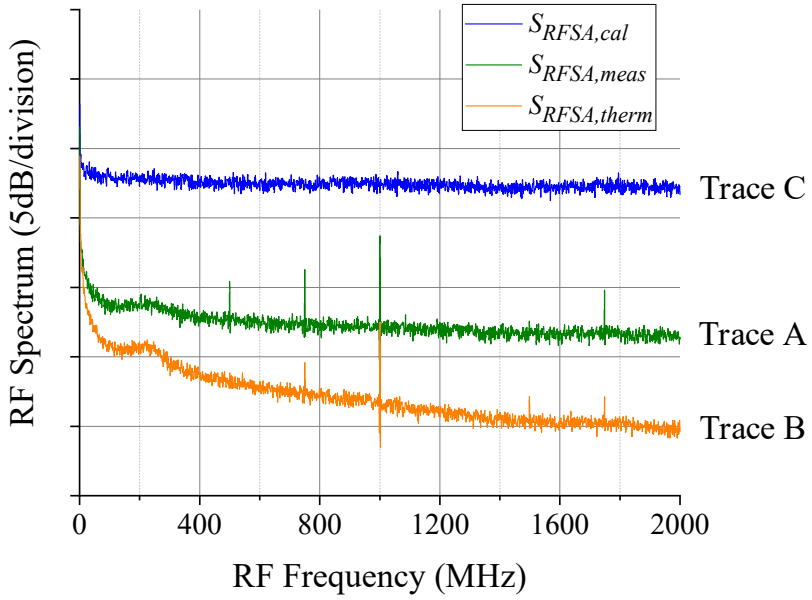

Figure 4-4: An example of electrical or RF power spectra measured by the RFSA that were used to determine the electrical NF of the O-band BDFA at the wavelength of 1350nm with the input power (P_{in}) of -20dBm. Note that the spikes in the traces A and B are from the internal clock of the RFSA.

According to [51], with these terms the corrected measurement of $S_n(f)$ can be written as:

$$S_n(f) = \frac{S_{RFSA,meas}(f) - S_{RFSA,therm}(f)}{\alpha^2 \times RFSA_{cal}} - N_{shot} \qquad \text{Equation 4-6}$$

where, $S_{RFSA,meas}(f)$ is the uncorrected amplifier noise spectrum [W].

$S_{RFSA,therm}(f)$ is the thermal noise correction [W].

α is the loss correction.

$RFSA_{cal}$ is the receiver calibration [Hz /W].

N_{shot} is the shot-noise correction [W^2/Hz].

The acquisition of these terms will be detailed in the following sections.

4.2.2.1 Thermal Noise Correction

Owing to the wide bandwidth of the electrical components used in a typical setup for the electrical methods, the thermal noise of the receiver cannot be ignored. Briefly, the thermal noise arises from the intrinsic noise of all of the electrical devices in the system and its magnitude varies with device quality and operating temperature. Fortunately, it is simple to take thermal noise into account, simply by treating it as background noise and subtracting it from $S_{RFSA,meas}(f)$.

To take the measurement of thermal noise, $S_{RFSA,therm}(f)$, an RF spectrum is acquired using the RFSA in the setup in Figure 4-3, but with all optical emission deactivated. An example of the measurement of $S_{RFSA,therm}(f)$ is shown in 'Trace B' of Figure 4-4. This can be subtracted directly from $S_{RFSA,meas}(f)$ with no further computation, as seen in Equation 4-6.

Besides this, it is important to note that the signal-spontaneous noise power generated at the PD must exceed the thermal noise of the receiver so that it is not hidden by the intrinsic thermal noise of the receiver. Hence, it is beneficial to illuminate the PD with as high a power as possible, meaning that PDs with a high saturation power are preferable, as long as there is no compromise in terms of bandwidth (response speed). A photodiode with a bandwidth that is wide (fast) enough to observe the frequency-dependent behaviour of the noise (generally >1GHz) is required. Alternatively, the thermal noise of the receiver can be reduced by cooling the operating temperature or improving the quality of the RF devices.

4.2.2.2 Loss Correction

The attenuator, ATT-2, is included into the system (Figure 4-3) to prevent saturation of the PD and is set to an attenuation of α (in linear units). As the RFSA is used to measure the signal-spontaneous beating, a reduction in the power of emission of the DUT by a factor of α results in a reduction in the RF power measured by the RFSA by a factor of α^2.

4.2.2.3 Receiver Calibration

Another major difference between the optical method and the electrical method is the difficulty of calibrating the receiver. The electrical components of the receiver – the PD, RFSA and any cables used, all typically have non-flat frequency responses over

the bandwidth scales of interest to the NF measurement. As such, the frequency response of the system must be calibrated. In this case, it is called $RFSA_{cal}$ in Equation 4-6.

This process uses the RIN-transfer technique [51]. The RIN-transfer technique is a way of determining the frequency response of the receiver by comparing a measurement of broadband ASE taken with the receiver to a measurement of the same ASE taken with an OSA. The spectral envelope of an ASE source which falls on a PD determines the shape of the RIN that will be measured by the PD. Knowing the spectral envelope allows us to calculate the RIN of the ASE source and therefore comparing this calculated RIN to the RIN measured using the receiver allows for determination of its frequency response. To obtain an accurate measurement of the ASE spectral envelope, an OSA can be used because of its broad bandwidth frequency-flat response. Once an ASE source has been measured with the OSA, the expected value of RIN can be calculated according to the following equation, derived from [51]:

$$RIN_{OSA,cal}(f) = \frac{\mathcal{F}\left(\left|\mathcal{F}^{-1}(S_{OSA,cal}(v))\right|^2\right)}{\left(\int S_{OSA,cal}(v)dv\right)^2} \qquad \text{Equation 4-7}$$

where, $RIN_{OSA,cal}(f)$ is the frequency-dependent RIN obtained from the OSA RIN-transfer technique calibration [1/Hz].

$\mathcal{F}$ and $\mathcal{F}^{-1}$ denote the Fourier transform and inverse Fourier transform, respectively.

$S_{OSA,cal}(v)$ is the measured optical power spectrum from the OSA as a function of optical frequency, v, [W].

The setup shown in Figure 4-5 (a) is used to perform the RIN transfer using the OSA. It consists of an unpolarised ASE-noise source, which is normally implemented using an optical amplifier operated with no input signal. The ASE noise is then partially filtered by an OBPF with a bandwidth wider than the electrical operating bandwidth of the PD (generally a bandwidth wider than 1nm is used). Then, at the receiver, the OSA is used to detect the optical power spectrum, $S_{OSA,cal}$. See Figure 4-6 (a) for the ASE spectrum from the OSA for an O-band calibration measurement. Its corresponding frequency-dependent RIN calibration trace obtained by applying Equation 4-7 is shown in Figure 4-6 (b).

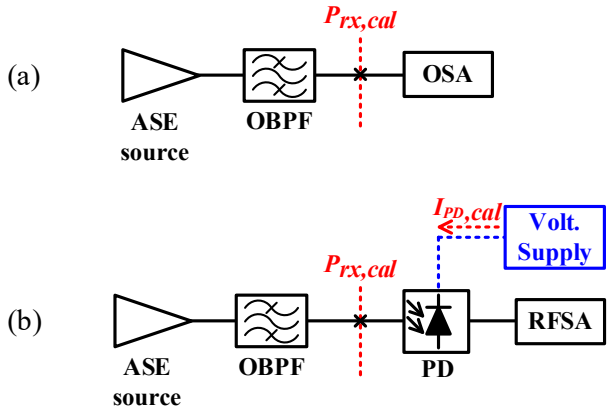

Figure 4-5: Experimental setup for the RIN-transfer calibration technique for (a) RIN from the OSA and (b) RIN from the PD and RFSA. The subscript '*cal*' denotes the parameters obtained from the calibration process.

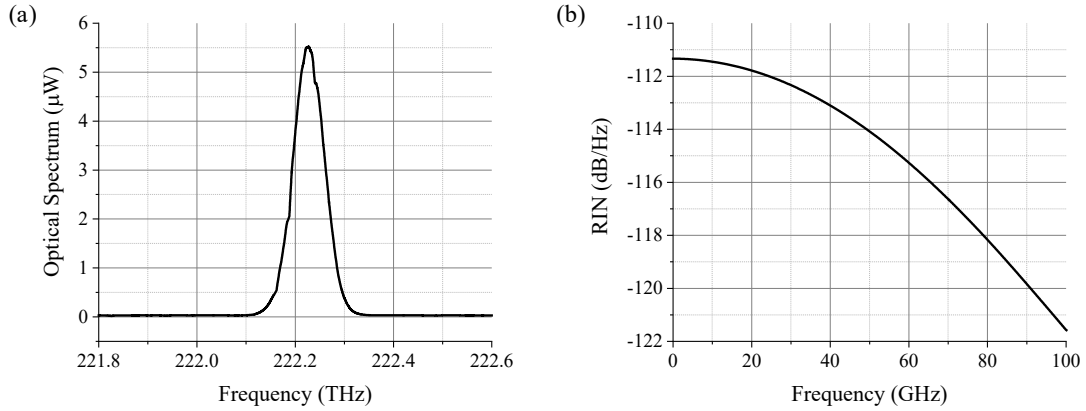

Figure 4-6: Receiver calibration using the RIN-transfer calibration technique measured at the wavelength of 1350nm for the O-band amplifier characterisation. (a) Measured optical power spectrum from an OSA. (b) Calculated RIN spectrum.

The next step is to find the RIN of the ASE source captured at the PD and the RFSA used in the electrical method. The setup shown in Figure 4-5 (b) is used to perform this measurement. The ASE source and the filter remain unchanged, whilst the receiver is replaced with a PD followed by an RFSA. The measured RF power spectrum, $S_{RFSA,cal}$, corresponding to that measured with the OSA is shown in 'Trace C' in Figure 4-4.

Consequently, the receiver calibration term, $RFSA_{cal}(f)$ in Equation 4-6, is acquired from the comparison between this measured RIN captured from the RFSA to the calculated RIN from the OSA, which can be expressed as, derived from [51]:

$$RFSA_{cal}(f) = \frac{S_{RFSA,cal}(f)}{RIN_{OSA,cal}(f) \times P_{rx,cal}^2}$$ Equation 4-8

where, $S_{RFSA,cal}(f)$ is the RFSA spectrum for RIN-transfer calibration [W].

$P_{rx,cal}$ is the detected power at the receiver in the calibration step [W].

Note that the scaling factor, $P_{rx,cal}^2$, in the equation takes into account the detected power at the PD in the electrical method.

4.2.2.4 Shot Noise Correction

Whereas the OSA provides a direct measurement of the power spectrum of the output of an amplifier, when the OSA is replaced by a PD and RFSA, it is actually the beating between the spectral components of the light that is detected. In detail and as discussed in Section 2.3.2, the amplified signal from a shot-noise limited source, detected by an ideal PD contains the three main types of noise: PD shot noise (N_{shot}), spontaneous-spontaneous beat noise (N_{sp-sp}), and signal-spontaneous beat noise (N_{sg-sp}). Among these noises, it is only the N_{sg-sp} term that represents the noise added by the amplifier and which determines the SNR degradation. N_{sp-sp} can be minimised by restricting the bandwidth of the ASE falling upon the PD (using an OBPF), whilst the contribution to $S_n(f)$ from the N_{shot} can be estimated mathematically from the PD responsivity or the measured drawn current when operating the PD. According to [51], the shot noise correction can be given by:

$$N_{shot} = \frac{2qI_{PD,meas}}{\left(\frac{I_{PD,cal}}{P_{rx,cal}}\right)^2}$$ Equation 4-9

where, $I_{PD,cal}$ is the current drawn by the PD during the calibration [A].

$I_{PD,meas}$ is the current drawn by the PD during the NF measurement [A].

To perform the shot-noise correction measurement, the two photocurrents, $I_{PD,meas}$ and $I_{PD,cal}$, are simply measured at the PD in their corresponding setups shown in Figure 4-3 and Figure 4-5 (b), respectively. This also includes measuring the optical power at the receiver, $P_{rx,cal}$, in the latter setup using an optical power meter.

4.2.2.5 NF Calculation

After calibrating the receiver and performing the correction for the meaurement noise, by substuting Equation 4-8 and Equation 4-9 into Equation 4-6, the corrected measurement of the spectral density of optical intensity noise $S_n(f)$ can be written as (with the labels indicating the corresponding factors of the terms):

$$S_n(f) = \frac{\overbrace{S_{RFSA,meas}(f) - S_{RFSA,therm}(f)}^{RFSA\ spectral\ traces}}{\underbrace{\alpha^2}_{Loss} \times \underbrace{\frac{S_{RFSA,cal}(f)}{RIN_{OSA,cal}(f) \times P_{rx,cal}^2}}_{Receiver\ calibration}} - \underbrace{\frac{2qI_{PD,meas}}{\left(\frac{I_{PD,cal}}{P_{rx,cal}}\right)^2}}_{PD\ shot\ noise} \quad \text{Equation 4-10}$$

Finally, the NF equation for the electrical-method measurement can be derived by substuting Equation 4-10 into Equation 4-5.

4.3 Frequency-Dependent NF via Electrical Method

This section provides the characterisation of the NF of several different optical amplifiers by using the electrical method that was discussed in Section 4.2.2. Firstly, a NF test on a commercial C-band EDFA will be presented in Section 4.3.1, which will form a benchmark characterisation. It will be followed by the results of the O-band BDFA and O-band SOA that have been studied throughout this thesis, in Section 4.3.2 and Section 4.3.3, respectively. Comparing these two amplifiers will illustrate the benefit of having an effective low-noise doped fibre amplifier in the O-band region. After this, the BDFA will be reconfigured into a double-pass topology in Section 4.3.4. Here, it is interesting to observe the frequency-dependent noise performance of this type of amplifier since it is expected to have higher gain and higher NF than that of the single-pass BDFA. Finally, the NF of a broadband Raman amplifier is presented in Section 4.3.5. This Raman amplifier is constructed to operate outside the O-band region, but its study is interesting because Raman amplifiers are also possible candidates for O-band amplification and their physics is very different to the other amplifiers presented in this section.

Note that the NF measurements for the amplifiers tested were performed with the setup shown in Figure 4-3 by replacing the DUT amplifier in the diagram accordingly. Moreover, separate calibration for each operating band (O- and C-bands) was required for accurate results.

4.3.1 EDFA

This section provides the preliminary test of the frequency-resolved NF measurement of a benchmarking EDFA. The amplifier tested is designed to be used as a pre- or inline- amplifier, and the manufacturer is Optokon-CLA (Czechlight Amplifier Devices). The testbed for the NF measurement shown in Figure 4-3 was used. A laser diode at 1550-nm was used at the signal source. The amplifier was set to operate in a constant-current mode with an input power of -20dBm. The amplified signal was then passed through a tuneable C-band filter, arriving at the PD, and analysed by the RFSA. The RF spectra captured from the RFSA for the NF measurement of the EDFA and the frequency-dependent NF result are shown in Figure 4-7.

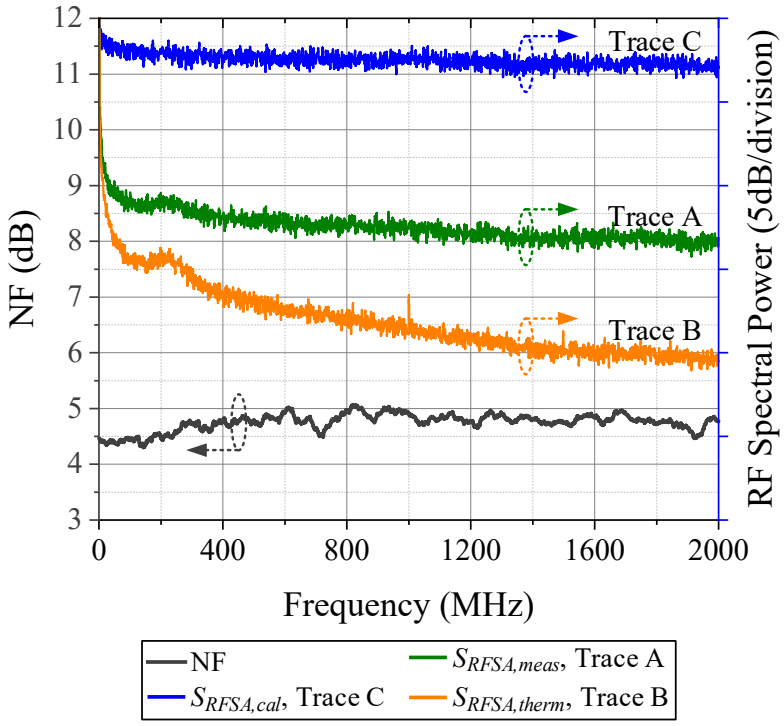

Figure 4-7: Frequency-dependent NF result of the EDFA tested at 1550nm and the spectral traces (calibration, thermal noise, and measured excess noise of the amplifier) from the RFSA.

The EDFA's NF trace throughout the 0-2GHz frequency range is around 4.5-5dB and does not exhibit any distinct features. The corresponding average NF value is 4.77dB at 1550nm. This value also agrees well with the specification on the device datasheet, which is between 4.3dB and 4.8dB. In summary, the result confirms the effectiveness of our implemented electrical NF measurements. This EDFA result will be used as the benchmark for the O-band BDFA, which will be presented next.

4.3.2 BDFA

This section presents the NF characterisation of the novel O-band BDFA. A description on the construction of this BDFA can be found in Section 2.4.3.1.1 and measurements on its gain characteristics were presented in Chapter 3. The test results at the input power of -20dBm at various wavelengths are shown in Figure 4-8 (a). Note that this input power was selected to prevent the amplifier from operating in saturation. We observe that the BDFA's NF exhibits a thoroughly flat frequency response across the frequency range of interest, with no pronounced low-frequency noise components [93]. Figure 4-8 (b) shows the average NF between 0MHz and 2000MHz as it varies with wavelength (blue solid line). The minimum NF is observed to be approximately 6.3dB at 1340nm and increases towards both edges of the plot, reflecting the shape of the gain profile (orange dashed line in Figure 4-8 (b), repeated here for convenience from the gain spectrum plot presented in Figure 2-12). Note that the upper testable wavelength range was limited by the maximum wavelength of the tuneable O-band laser diode used (1360nm).

For comparison, the NF was also measured with the optical method described in Section 4.2.1. These results are plotted in Figure 4-9 alongside the averaged NF results from the electrical method presented in Figure 4-8 (b). It can be seen that the shape of the NF curve is similar between the results obtained using the electrical and optical method, although the electrical method proves that there is no unexpected low frequency noise. The difference between the values measured using each method could simply be due to random measurement error. However, it could also be due to the differing frequency resolution of the two methods; the optical method, with its much coarser frequency resolution compared to the electrical method, will include more of the ASE surrounding the carrier in its estimation of signal power. Otherwise, unwanted spontaneous-spontaneous beat noise (which is present in the electrical method, but not in the optical method) could also contribute to making the results of the two methods different (see their power spectral density of the ASE, ρ_{ASE}, that contributes to the difference in their NF equation shown in Equation 4-3 and Equation 4-5).

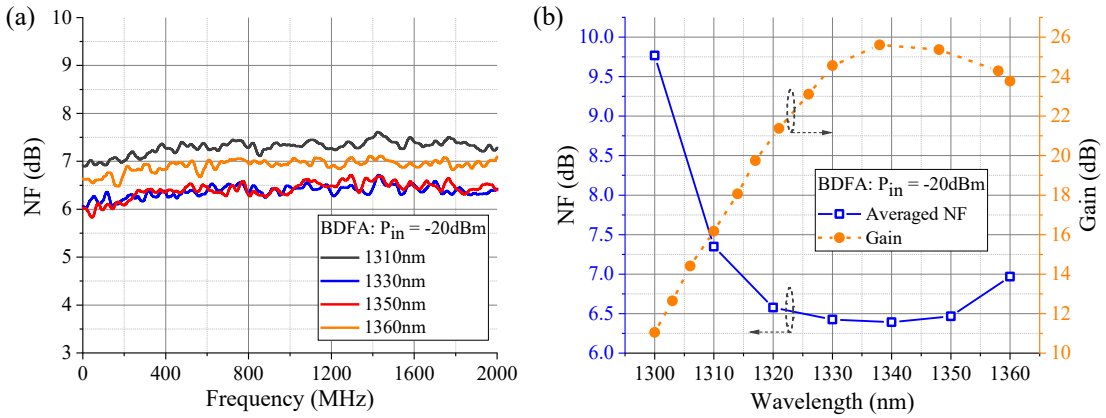

Figure 4-8: (a) Frequency-dependent NF of the BDFA and (b) averaged NF of the BDFA as it varies with wavelength.

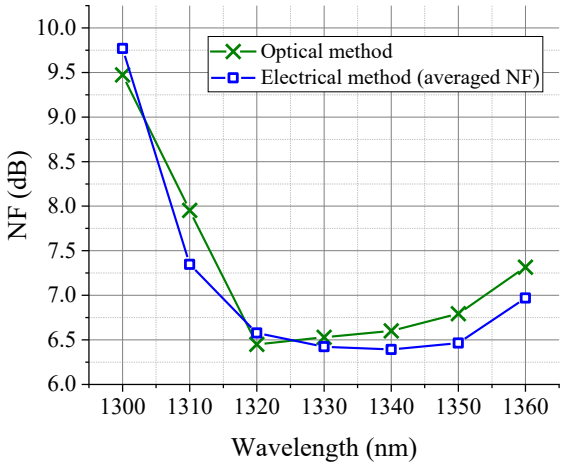

Figure 4-9: Measured NF values of the BDFA using the optical method and the electrical method (averaged NF values). The OSA resolution used in the optical method was 0.01nm.

Moreover, in comparison with the commercial C-band EDFA tested and presented in Section 4.3.1, the BDFA's frequency-dependent NF traces are as flat as the reference pre-amp EDFA presented earlier, although 1-2dB higher. It is possible that this is because of the length of the BDFA (150m) which was much longer than that of a typical EDFA (which commonly has a length of tens of meters). The necessarily long fibre length implies a risk of elevated low-frequency NF (which was not observed) and elevated frequency-flat NF due to the intrinsic loss (per unit length) of the fibre [94]. An experimental study of the gain performance of the BDFA provided in [79] showed that by increasing the bismuth concentration and reducing the diameter by 20%, the fibre length could be reduced to 98m, although the outcome resulted in a lower gain. This could be due to gain quenching effects at high dopant concentration [95], unsaturable loss, and the amount of OH absorption [79]. Additionally, the long fibre

directly affects pump absorption, with the pump gradually depleting along the length of the fibre [94].

Furthermore, to demonstrate the effect of amplifier saturation on the BDFA's performance, a characterisation of the input power dependence of the averaged NF was performed, measured again using the electrical method. The result is shown in Figure 4-10, tested at a wavelength of 1350 nm. The NF increases with increasing input power, a general characteristic of optical amplifiers, induced by the optical gain compression owing to the onset of saturation [50]. This phenomenon can also be examined from the NF equation in Equation 4-5.

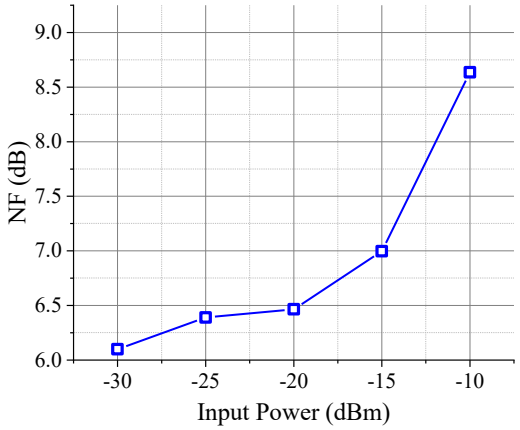

Figure 4-10: Averaged NF of the BDFA at the wavelength of 1350nm as it varies with input power.

4.3.3 SOA

Here, we provide frequency-resolved NF measurements for an O-band SOA since it is the most typical amplifier used in O-band transmission. Therefore, it is interesting to observe the frequency-dependent NF and be able to compare its noise performance with that of our BDFA. The SOA tested here is the same as the one used in the transient gain characterisation of Section 3.3.

A similar methodology was performed as in the previous section and the results are shown in Figure 4-11 (a) and Figure 4-11 (b) for the frequency-dependent NFs and their corresponding averaged NF values, respectively. Predictably, the results obtained from the SOA confirm the superior performance of the BDFA, since the SOA shows both a lower gain and a higher NF. The high NF of the SOA is most often a result of the high coupling loss between chip and fibre (typically around 1.5-2dB), in particular,

the loss from coupling into the input facet of the SOA can be especially detrimental to NF [96].

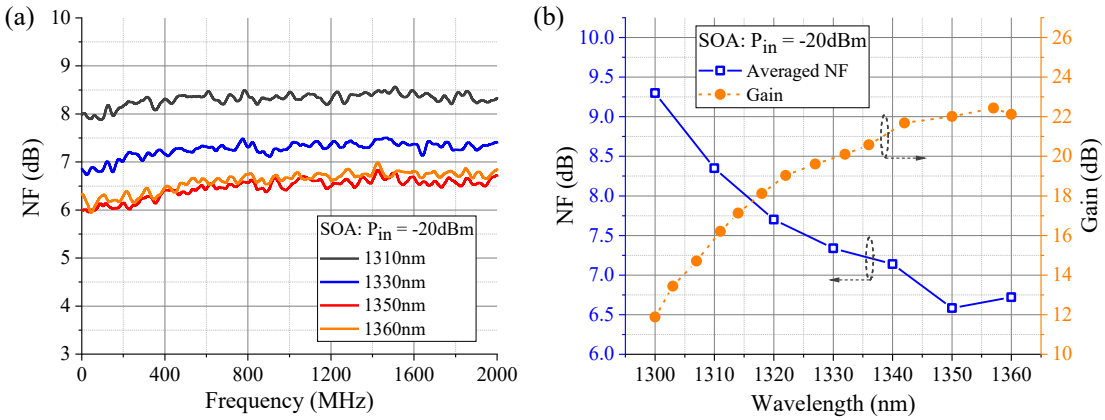

Figure 4-11: (a) Frequency-dependent NF of the SOA, and (b) Averaged NF of the SOA as it varies with wavelength.

4.3.4 Double-Pass BDFA

So far, the noise performance of the BDFA was compared to a reference EDFA as well as a commercial O-band SOA. In this section we consider a different BDFA that possesses a double-pass configuration. The motivation for its implementation was to improve the amount of gain over the original single-pass amplifier by means of circulating the amplified signal twice through the gain fibre, although a higher NF could be expected [79] [97] [98]. The tested double-pass BDFA here is based on the BDFA that we previously presented in Section 4.3.2. The resulting gain of this amplifier in the 1330-1360nm region is approximately 29dB at 1360nm, thus improving the gain by a maximum of 7dB compared to the single-pass configuration. See [79] for more details on this amplifier, including the optical characterisation of its gain and NF.

For convenience, we provide the diagram of the double-pass BDFA in Figure 4-12. Similar to the pumping scheme used in the single-pass BDFA, see Section 2.4.3.1.1, the BDF here is also bi-directionally pumped at 1270nm and 1240nm from pump laser-diodes 1 and 2 (Pump LD-1 and Pump LD-2), respectively. The signal is launched into the isolator and is directed from port 1 to port 2 of the first circulator (CIRC-1). Next, it is combined via a WDM multiplexer (WDM-1) into the BDF for the first pass in the fibre. Afterwards, the amplified signal is directed by WDM-2 towards a second circulator (CIRC-2) whose ports have been configured so that it acts as a mirror (ports 1 and 3 are connected), redirecting the signal back through the BDF for the second

pass. Subsequently, after being amplified twice, the signal propagates back into port 2 of CIRC-1 and is directed out to port 3, which is the output port of the double-pass BDFA.

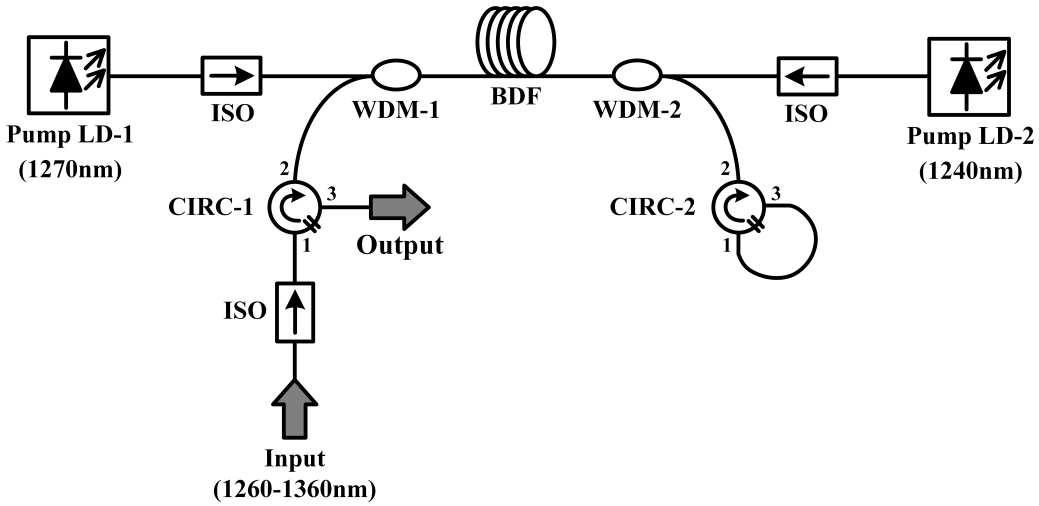

Figure 4-12: Schematic diagram of the double-pass BDFA.

The NF characterisation results tested at two different input powers are presented in Figure 4-13. Whilst the tails of the NF traces in both cases are relatively flat, it is clear that there is a prominent low-frequency noise appearing at the longer wavelengths of the testing range. This becomes significant at an input power of -23dBm at 1350nm (see Figure 4-13 (a)), whereas at 1330nm it can already be observed at -20dBm (see Figure 4-13 (b)). To further investigate the effect of the input power on this low-frequency noise, we also performed measurement for various input powers at a wavelength of 1350nm. The NF traces and the corresponding average NF results at various input powers are shown in Figure 4-14 (a) and (b), respectively. The results show further growth in low-frequency noise when the input power is increased, especially the significant increase at -10dBm.

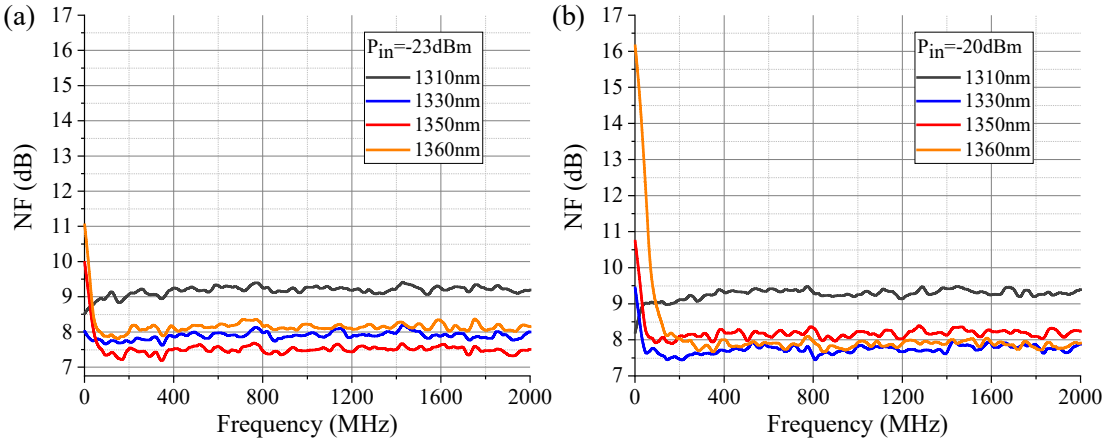

Figure 4-13: Frequency-dependent NF of the double-pass BDFA at the input powers of (a) -23dBm and (b) -20dBm.

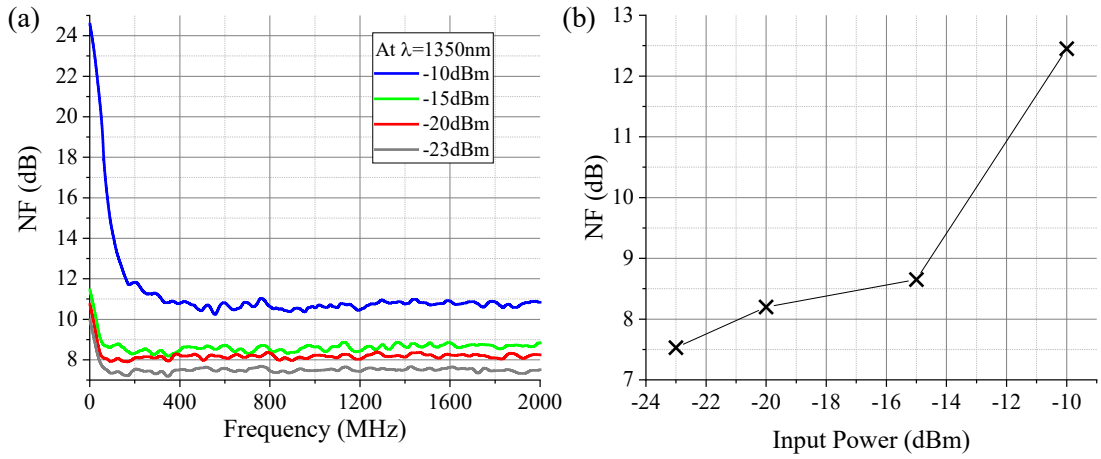

Figure 4-14: NF measurement results at 1350nm of the double-pass BDFA for (a) frequency-dependent NF with varying the input power and (b) averaged NF (from 0Hz to 2000MHz) at various input powers.

By virtue of the two passes in the active fibre, this configuration should offer a higher gain than its single-pass counterpart. Although, a higher gain might be expected to result in a lower NF, this is often not true for practical implementations of double-pass amplifiers. This is because, if the gain saturates during the signal propagation (in what is now effectively too long an active fibre length) then this implementation is likely to deliver a higher NF (due to the gain suppression effect discussed in Section 4.3.2). Since the double-pass configuration was intended to offer higher gain than the single-pass version, saturation of the gain in the first pass of the fibre renders the double-pass configuration needless. Furthermore, additional loss at the input of the amplifier caused by the inclusion of a circulator is responsible for a frequency-flat degradation in noise performance. However, apart from this frequency-flat NF

degradation, the distinctive features of the measurements in Figure 4-13 (a) and (b) and Figure 4-14 (a) were the noise peaks observed at low frequencies. In transmission, these low-frequency components of NF can be observed as a slow power variation in the transmitted waveform (similar to scintillation) which results in a similar variation in received SNR, complicates detection and thus can cause errors [99]. This slow power variation can become even worse when cascading amplifiers (e.g., if the frequency of the noise is lower than the carrier lifetime of the amplifiers).

There are several factors that could contribute to the increased noise at low frequencies: 1) leakage from the circulators, 2) Rayleigh scattering, and 3) patterning effect induced from gain depletion. The leakage depends upon the effectiveness of the circulator in terms of directivity and return loss, which are typically greater than 50dB. Since the amplifier can provide 29-dB gain in total, the impact of any leakage, for example at the first circulator, from the input signal (-20dBm) to the output signal (9dBm) is expected to be insignificant.

With regards to Rayleigh scattering, it is always possible that back scattering can contribute some interference to the propagating signal and this effect has been studied before [95] [100]. The term patterning is typically used to refer to a modulation of the gain of an amplifier (e.g., an SOA) due to the pattern of a signal transmitted through it. Such an effect could be defined as temporal patterning, as it depends upon carrier dynamics driven by the carrier lifetime of the amplifier and gain recovery [101]. In contrast, in the double-pass BDFA we see what could be described as spatial patterning, as gain is instead modulated by two counter-propagating signals, each competing for the same gain (when the amplifier is saturated). This patterning effect, which is induced from the gain depletion can only take place when the amplifier is saturated, in which case the gain will be governed by slow noise components [92]. Furthermore, we also already observed a very similar effect during the cross-gain modulation characterisation, see Figure 3-8 in Section 3.4. With that in mind, if the input power is -20dBm, the power of the amplified signal entering the BDF a second time will be 2dBm (single-pass gain is 22dB [79]), assuming that the gain in the double-pass amplifier is not saturated and the pump power is not depleted. Considering this input power (2dBm), it is very likely that the amplification in the second pass will consequently operate in the saturation regime, hence causing the patterning effect at low frequencies. This analysis of saturation-induced patterning

effect also supports the results shown in Figure 4-14 (a) (the higher the input power, the stronger the low-frequency noise).

It is clear that the double-pass configuration suffers a much greater degradation in NF under saturation than does the single-pass configuration, so saturation should be avoided at all costs. Other than this, the insertion loss of all additional optical components included in the design, most notably the first circulator that the signal passes through, should be reduced and the isolation of the circulators improved.

After providing a substantial set of analysis of the double-pass BDFA's noise performance, we can confirm that the electrically measured NF is a necessary characterisation, since it can reveal such frequency-dependent noise effect that would be completely hidden from the optical method. This is, once again, because an OSA cannot be used to measure noise possessed of a frequency lower than its resolution bandwidth. It is interesting to note, however, that the NFs reported for a number of double-pass optical amplifiers (e.g., [79] [97] [98]) were measured using the optical method and hence the possibility that these amplifiers exhibit excess low-frequency noise that could not be detected.

4.3.5 Broadband Raman Amplifier

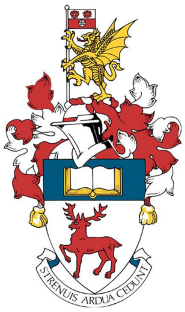

Content in this section has been embargoed

References used in this section are as follows: [49] [65] [102] [103] [104] [105] [106] [107] [108].

4.4 Conclusion

In this chapter, methods were presented to characterise the NF of optical amplifiers, covering both the more prevalent optical technique as well as the more complete electrical technique. Although the optical technique has simpler equipment

requirements and is more straight-forward to perform, it importantly cannot resolve NF over the fine frequency scales that the electrical method is capable of.

The electrical method was applied to the measurement of the NF of a number of optical amplifiers. Firstly, the functioning of the scheme was confirmed by measuring the NF of a typical EDFA and the results used as a benchmark, given that the EDFA is the most popular optical amplifier in use today. After this, the scheme was used to measure the NF of the BDFA, which was found to be as low as ~6.3dB. It was also confirmed that the BDFA did not suffer from excess low-frequency noise, a result which supports the suitability of the BDFA for use in data transmission. The SOA exhibited a NF of ~6.6dB, which was slightly higher NF compared to the BDFA, but also lacked excess low-frequency noise.

The absence of excess low frequency noise was the preferred result for the BDFA, but to really take advantage of the frequency-resolved NF measurement offered by the electrical method, the technique was also applied to the characterisation of a double-pass BDFA and a broadband Raman amplifier.

With regards to the double-pass BDFA, it is interesting to note that the double-pass configuration has historically been understood to offer in increased gain, but the low-frequency noise does not seem to have been investigated [79] [97] [98]. The application of the electrical method revealed that the double-pass BDFA suffered from excess low-frequency noise which became worse with increasing input power. This could mainly be attributed to saturation-induced patterning effects. Meanwhile, the broadband Raman amplifier also showed an excess of low-frequency noise, but for very different reasons. In this case, the noise arose from pump RIN transfer. In both cases, the abundance of low-frequency noise could have been overlooked if the NF was measured using a typical OSA, due to its coarse resolution bandwidth.

Overall, the benefits of the electrical method were made clear in this chapter and it can be concluded that, for any novel or experimental amplifier, adopting the electrical method is essential to provide confidence that the amplifier being tested does not exhibit unexpected low frequency noise.

Chapter 5

WDM O-band Transmission

5.1 Introduction

Several characterisation studies of the BDFA in terms of gain and additive noise were presented and discussed in the previous chapters, and in these, from a transmission perspective, the BDFA generally outperformed the commercial O-band SOA to which it was compared. Despite this promising characterisation, it is possible for there to be unexpected deleterious optical effects within the amplifier. Therefore, it is important to prove the capability of the BDFA in a realistic O-band transmission.

In this chapter, the first ever demonstration of wavelength-division multiplexed (WDM) O-band transmission using a BDFA will be presented. Both coarse-WDM (CWDM) and dense-WDM (DWDM) systems were considered, to give a valuable indication of real-world performance. Specifically, the motivation for performing CWDM transmission was to prove acceptable performance across as much of the BDFA gain bandwidth as possible, by using six equally spaced channels across the wavelength region 1321-1371nm. Since the transmission reach in these experiments was limited by the achievable launch power into the first fibre span, in order to extend the reach of the demonstrations, the number of channels was reduced from six to four, resulting in an increase in reach from 100km to 120km.

Although the CWDM case can prove suitable functioning of the amplifier over a broad bandwidth, there are a number of causes of signal degradation (such as FWM) that are diminished by the broad channel spacing used in this scenario. Therefore, to provide confidence in the amplifier's functioning with a small channel spacing of 100GHz, a DWDM scenario was considered. Equipment availability limited the number of channels to three. In this case a reach of 120km was achieved. Similar to in the CWDM cases, a reduction in channel count from three to two in a 200-GHz channel spacing DWDM experiment permitted a reach extension from 120km in the three-channel case to 140km in the two-channel case. As this work stands as an early demonstration of WDM transmission using an O-band BDFA, OOK was selected as the test format, to give readers an intuitive understanding of the results and conclusions. Finally, a supplementary investigation of the nonlinear performance of the amplifiers used in the experiments was performed to give an early indication of the behaviour of the BDFA under deep saturation. Note that the work presented in this chapter was reported in Publications 3 and 4 listed in the Publications as First Author section.

The organisation of the chapter is as follows. Firstly, the CWDM scenario will be presented in Section 5.2, with the main results for the six-channel and four-channel CWDM case presented separately in Section 5.2.2.1 and Section 5.2.2.2, respectively. Section 5.3 is dedicated to DWDM transmission, in which the three-channel and two-channel DWDM results are presented in Section 5.3.2.1 and Section 5.3.2.2, respectively. Section 5.4 provides the results of the nonlinear performance measurement of the SOA and the BDFA. Finally, Section 5.5 summarises the results of this chapter.

5.2 CWDM Transmission

This section provides the experimental work of the CWDM amplified O-band transmission with channel spacing of 10nm. Firstly, the details of the experimental setup used in the work will be presented and then followed by the experimental results.

5.2.1 Experimental Setup

The configuration of the multi-channel transmission system with inline amplification used in the CWDM experiments is shown in Figure 5-1. The transmitter contained six lasers (LASs), four of which (λ_2, λ_3, λ_4, and λ_6) were distributed feedback (DFB)

lasers, and two (λ_1 and λ_5) were tuneable external cavity lasers. The wavelength of each laser/channel was $\lambda_1 = 1321\text{nm}$, $\lambda_2 = 1331\text{nm}$, $\lambda_3 = 1341\text{nm}$, $\lambda_4 = 1351\text{nm}$, $\lambda_5 = 1361\text{nm}$, and $\lambda_6 = 1371\text{nm}$. The transmission window used in this CWDM case spanned 50nm, i.e., from 1321nm to 1371nm, corresponding to a bandwidth of ~8.3THz, or approximately 1.9 times broader than the bandwidth of a typical C-band EDFA.

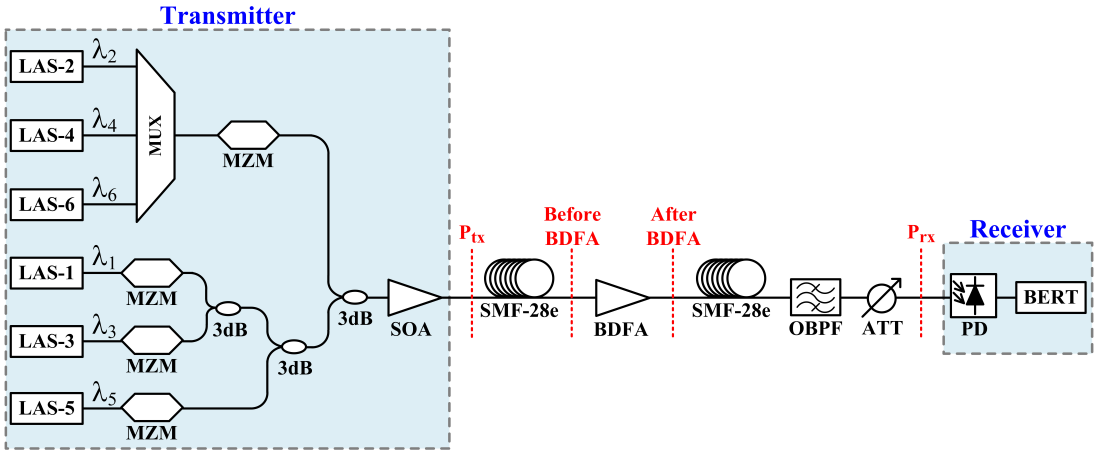

Figure 5-1: Experimental setup of CWDM transmission link with inline-BDFA amplification.

The lasers for the odd channels λ_1, λ_3, and λ_5 were modulated in separate modulators (MZM) before being combined through a network of 3-dB couplers, whilst the even channels λ_2, λ_4, and λ_6 were firstly combined in a planar lightwave circuit multiplexer (MUX) before being modulated, as shown in Figure 5-1. Consequently, after multiplexing all the wavelengths, no two neighbouring signals carried the same synchronised data. All the lasers were modulated to carry 9.953Gbit/s OOK 2^{31}-1 pseudorandom bit sequences (PRBS). After combining all the channels, the signals were amplified using the O-band SOA to provide sufficient launch power.

The maximum total launch power after adjusting the powers and states of polarisation of all laser sources (to ensure the powers of all channels were identical at the output of the SOA), was approximately 10-dBm total launch power, at P_{tx} point in Figure 5-1. It is noted, once again, that the SOA exhibited a strong PDG – its polarisation extinction ratio (PER) was about 16dB [61] – thus preventing it from being used at any point other than just after the transmitter, where the states of polarisation of the different wavelength channels could be ensured and be aligned relative to one another.

After boosting the signal launch power by the SOA, the signals were transmitted into the transmission fibre. Various lengths of SMF-28e were used in the experiments, with an average loss of 0.34dB/km at the wavelengths of interest. All experiments involved two spans of fibre, with the BDFA employed in the middle to compensate for the link loss. The gain provided by the BDFA was higher than 20dB in all the cases that were studied. After the second span of transmission fibre, one of the WDM signals was selected using an optical bandpass filter (OBPF) with a bandwidth of 1.2nm, before being detected using a photodetector (PD) and passed to a BER tester (BERT). The BER measurements are provided relative to the received optical power, P_{rx} point labelled in Figure 5-1, which was controlled through an optical attenuator (ATT) placed before the PD.

5.2.2 Experimental Results and Discussions

In this section, a discussion of the CWDM transmission results will be provided to demonstrate the capability of the BDFA across as wide a bandwidth as possible. The discussion will be divided into the two scenarios that were experimented with – transmission with six channels and transmission with four channels. In the experiment, the launch power was limited because of the performance of the SOA, which effectively determined the number of channels that could be transmitted.

5.2.2.1 Six-Channel CWDM over 100-km Transmission

The transmission reach of the six-channel CWDM was limited to 100km in total, i.e., 50-km span length (~17dB span loss). The spectra of the six-channel CWDM transmission are presented in Figure 5-2. Note that some gas absorption lines (the sharp lines around 1360nm) can be observed in these spectra due to the presence of water vapour in the air within the OSA. Figure 5-2 (a) shows the spectrum taken at the SOA output at the transmitter with the OSNR of every channel adjusted to be approximately identical. By comparing Figure 5-2 (b) and Figure 5-2 (c), it is found that the OSNR degradation of each signal after in-line amplification was approximately 2.8dB. The spectrum at the receiver is shown in Figure 5-2 (d), in which the reduction in OSNR was ~5dB relative to that of the transmitter, mainly due to the ASE of the amplifiers. Additionally, it is noted that no evidence of FWM is seen in the spectra, owing to the broad spacing between the optical carriers.

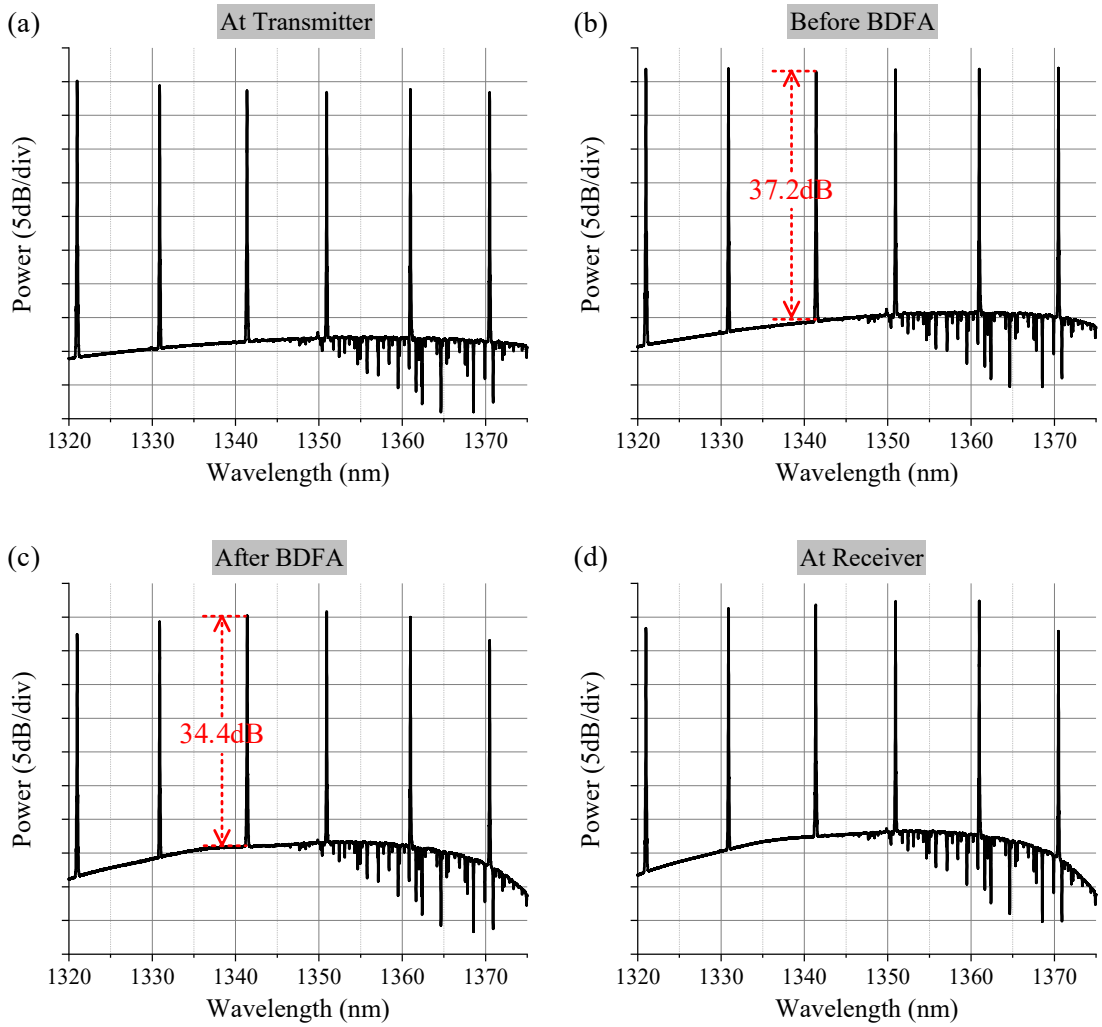

Figure 5-2: Optical spectra measured at various positions of a 100-km transmission system for an experiment considering six channels at coarse spacing – (a) at the transmitter, (b) before the BDFA, (c) after the BDFA, and (d) at the receiver.

Figure 5-3 (a) to (f) provide BER plots of the six channels. The plots obtained after transmission (circle) are compared to those taken immediately after the transmitter (triangle). All signals show negligible change in receiver sensitivity after amplification. Note that the results for $\lambda_4 = 1351$nm (Figure 5-3 (d)), contain an error floor in both the back-to-back and post-transmission cases due to excessive noise from the source laser at the transmitter. A number of the BER curves after transmission can be seen to have a better receiver sensitivity than the back-to-back BER curves, which would imply a negative receiver sensitivity. This improvement with transmission is quite possibly due to the interaction between the chirp of the single-drive modulators and the dispersion of the transmission fibre, which essentially results in mild pulse compression, improving eye opening [109].

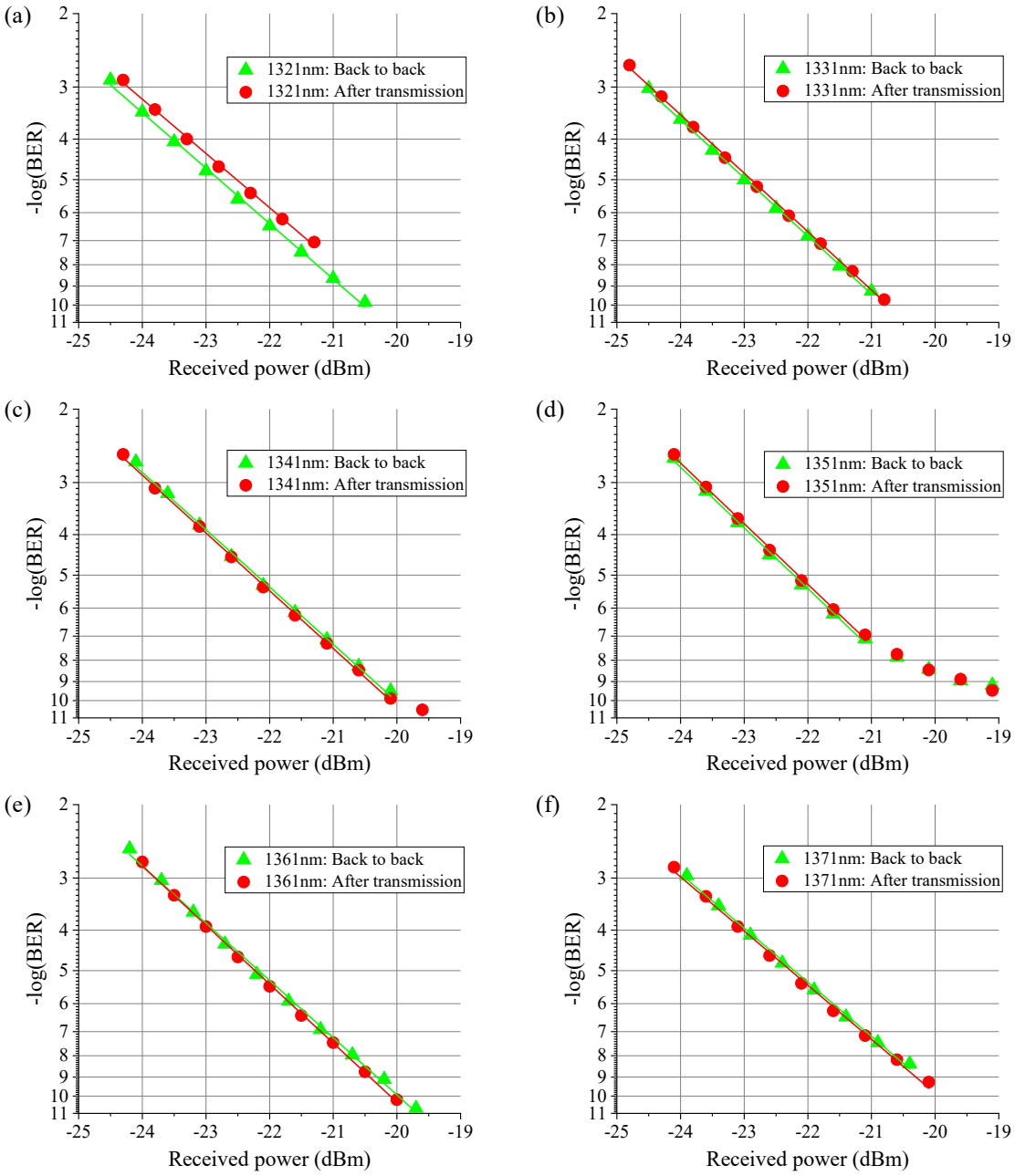

Figure 5-3: BER curves of the six-channel CWDM transmission for back-to-back and after 100-km transmission at the wavelengths of (a) 1321nm, (b) 1331nm, (c) 1341nm, (d) 1351nm, (e) 1361nm, and (f) 1371nm. The symbols, both triangles and circles, in the plots represent the measured BERs and the lines are the linear fit of those sets of measured data.

5.2.2.2 Four-Channel CWDM over 120-km Transmission

By deactivating the signals at λ_1 and λ_6, the number of channels was reduced to four in total. Consequently, due to the increased power per channel in the link (as high as ~3.5-dB improvement), the span length could then be extended to 60km (~20.4dB span loss), for a 120km total transmission length. The spectra of the four channels in the CWDM transmission are presented in Figure 5-4, showing the transmitted wavelengths of 1331nm, 1341nm, 1351nm, and 1361nm.

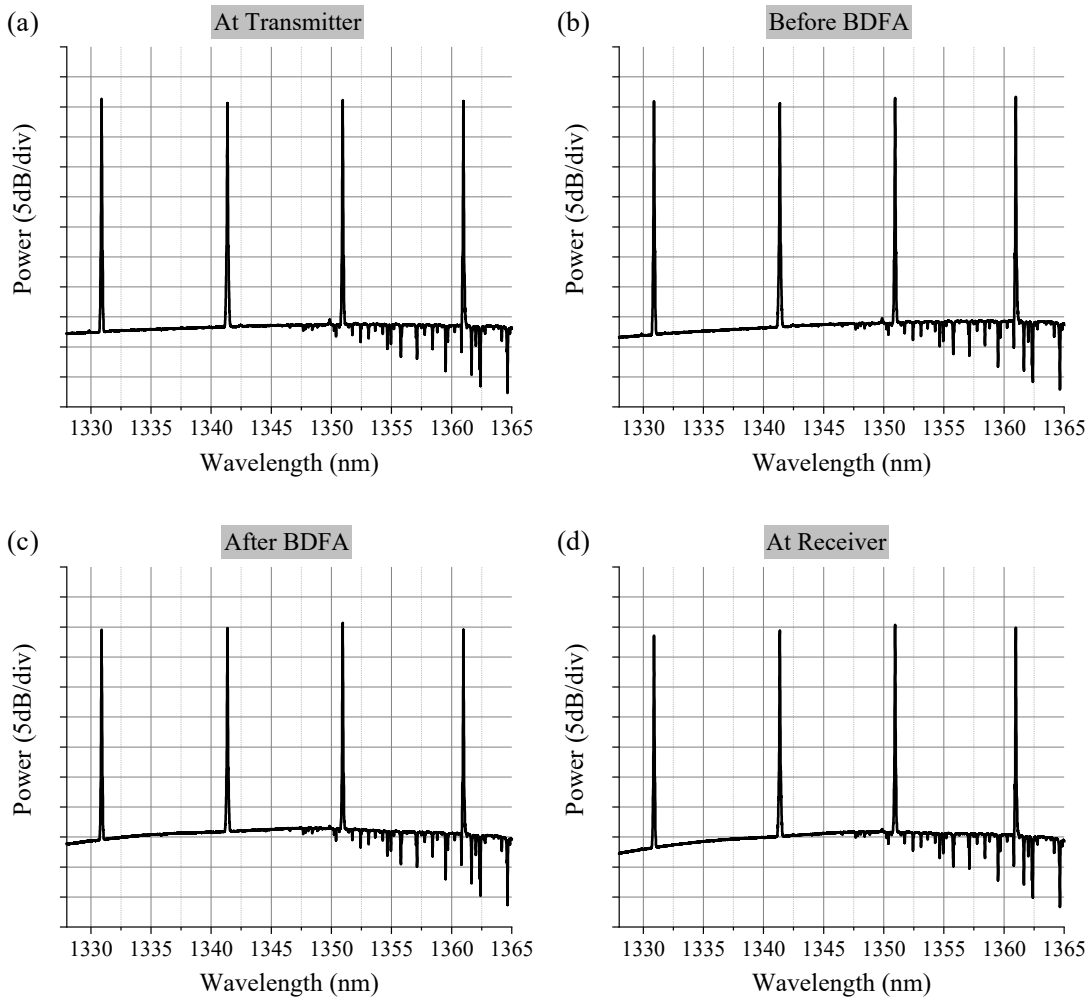

Figure 5-4: Optical spectra measured at various positions of a 120-km transmission system for an experiment considering four channels at coarse spacing – (a) at the transmitter, (b) before the BDFA, (c) after the BDFA, and (d) at the receiver.

BER curves for the transmission are presented in Figure 5-5 (a) to (d). Similar performance as in the six-channel case presented in Section 5.2.2.1 was observed. (Note again that the error floor observed at 1351nm that was due to the source laser itself).

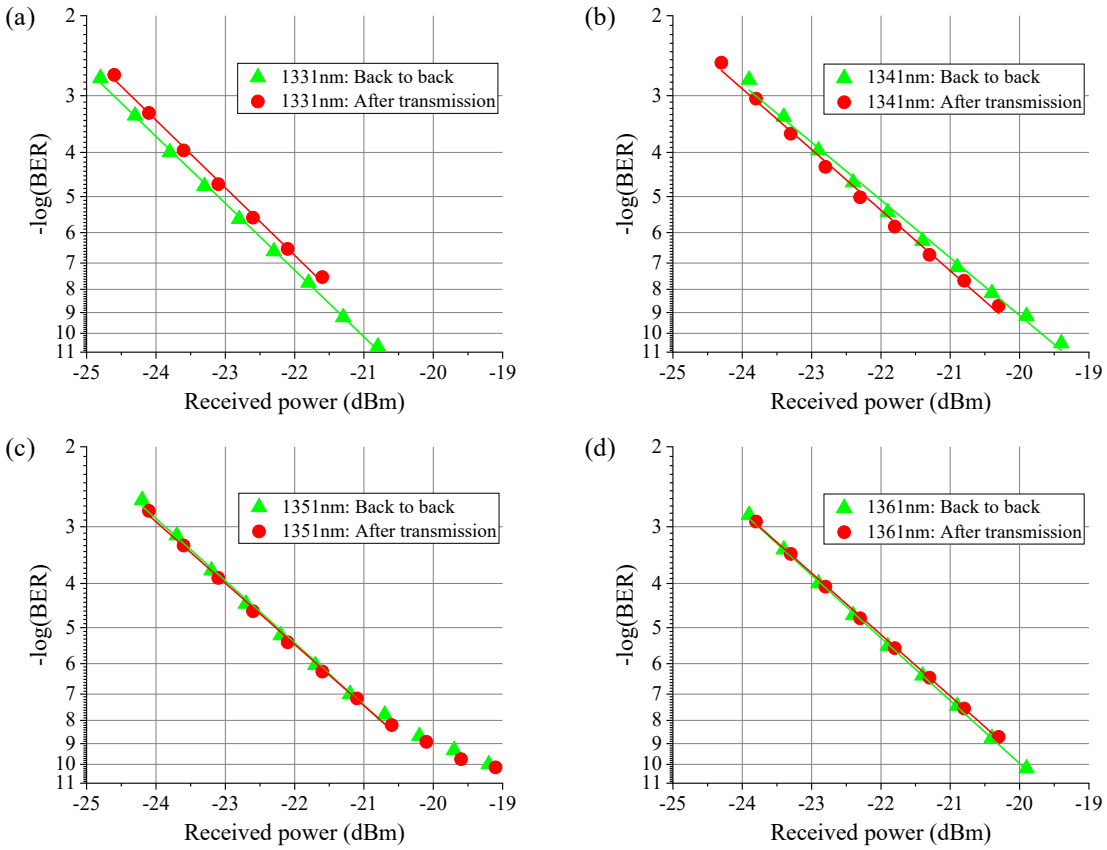

Figure 5-5: BER curves of the four-channel CWDM transmission for back-to-back and after 120-km transmission at the wavelengths of (a) 1331nm, (b) 1341nm, (c) 1351nm, and (d) 1361nm. The symbols, both triangles and circles, in the plots represent the measured BERs and the lines are the linear fit of those sets of measured data.

5.3 DWDM Transmission

In this section, the amplified O-band DWDM transmission experiment for three channels and then two channels will be presented. The total transmission reach for each case was 120km and 140km for the three and two channels, respectively, and the transmission fibre used was SMF-28e.

5.3.1 Experimental Setup

The experimental setup for the three-channel DWDM transmission is shown in Figure 5-6. It is essentially the same as for the CWDM case, but with three wavelengths deactivated (λ_2, λ_4, and λ_6) and their connected 3-dB coupler was bypassed (as shown in the grey shaded parts at the transmitter). Meanwhile, the two tuneable sources, λ_1

and λ_5, were set to 1342.4nm and 1343.6nm, respectively, the channel for λ_3 remained at 1343nm, to experiment on a dense wavelength 100-GHz grid (~0.6nm spacing).

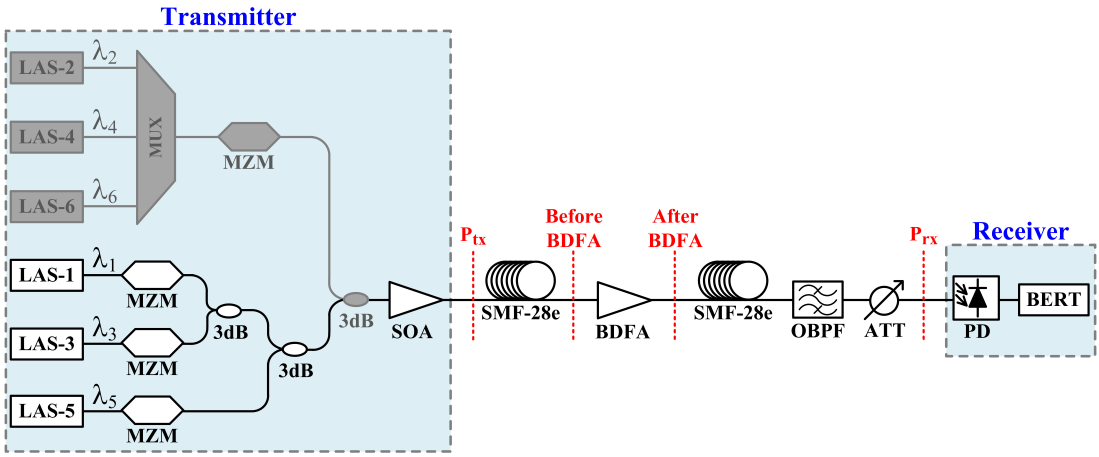

Figure 5-6: Experimental setup of DWDM transmission link with inline-BDFA amplification.

5.3.2 Experimental Results and Discussions

In this section, a discussion of the DWDM transmission results will be provided to demonstrate the performance of the BDFA with a realistic channel spacing for DWDM. The discussion will be divided into the two scenarios that were experimented with – transmission with three channels and transmission with two channels. Once again, the launch power was limited in the experiment because of the performance of the SOA, which effectively determined the number of channels that could be transmitted.

5.3.2.1 Three-Channel DWDM over 120-km Transmission

Figure 5-7 (a) shows a spectral trace of the three DWDM signals at the transmitter output, which illustrates some weak FWM components that were generated after amplification in the SOA. A comparison between the spectra presented in Figure 5-7 (a) and Figure 5-7 (b) reveals that transmission along the fibre enhanced the FWM due to the Kerr effect. A small (but negligible) further enhancement of the FWM products (of ~0.7dB) was observed after in-line amplification in the BDFA (Figure 5-7 (c)). As with the first span, propagation along the second span of fibre also increased the FWM as can be seen in Figure 5-7 (d). BER measurements for the three channels in this transmission experiment are presented in Figure 5-8 (a) to (c) and confirm there was no power penalty due to the transmission and that the FWM did not affect the transmission performance.

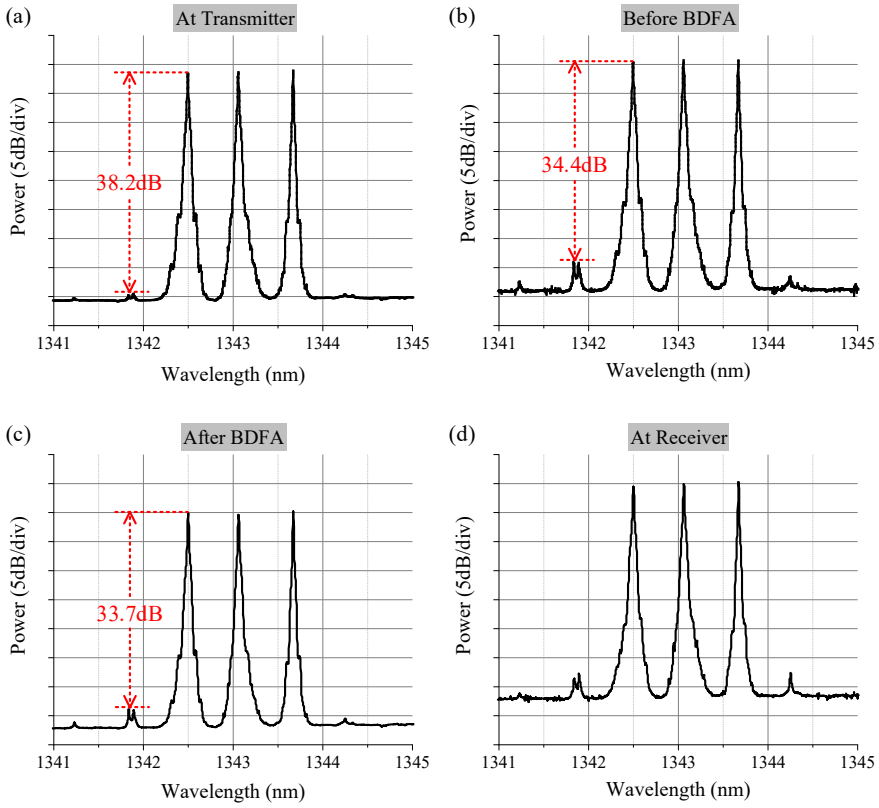

Figure 5-7: Optical spectra measured at various positions of a 120-km transmission system for an experiment considering three channels at dense spacing.

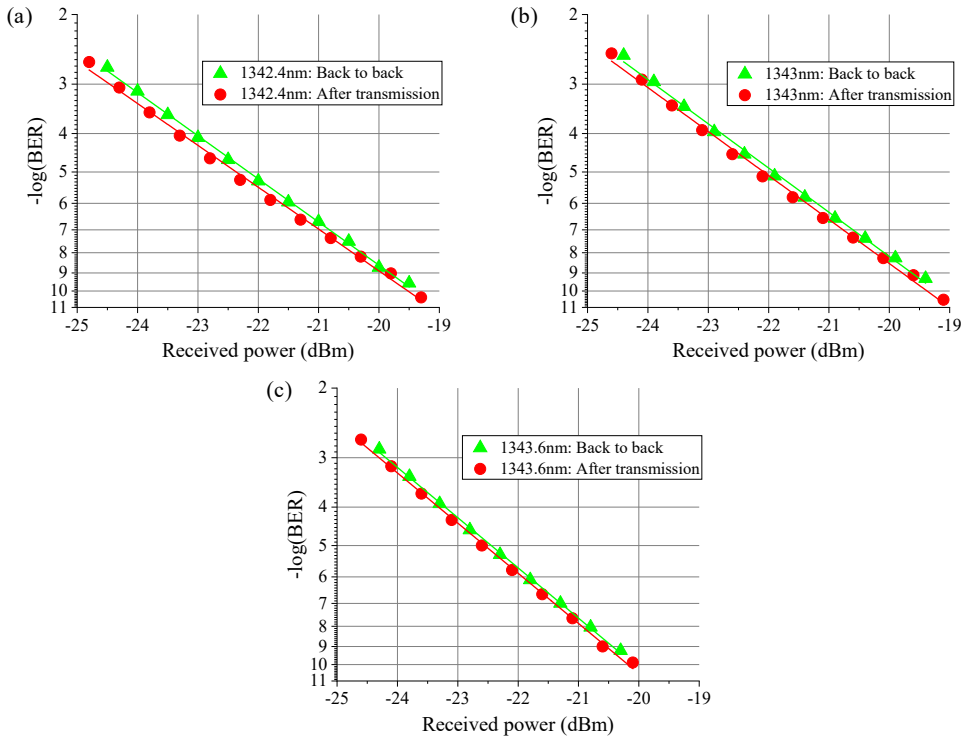

Figure 5-8: BER curves of the three-channel DWDM transmission for back-to-back and after 120-km transmission. The symbols, both triangles and circles, in the plots represent the measured BERs and the lines are the linear fit of those sets of measured data.

5.3.2.2 Two-Channel DWDM over 140-km Transmission

Finally, by removing one channel, λ_3, (meaning that the channel spacing became 200GHz) it was possible to extend the span length to 70km per span, resulting in 140km total reach. BER measurements for this case are summarised in Figure 5-9 (a) and (b). Note that, due to the extra loss induced by the additional fibre length, the maximum optical power at the receiver was -21.5dBm. This prevented us from carrying out a full power scan in our BER measurements, however as in the previous cases, the trend indicates no performance degradation in the transmitted signal.

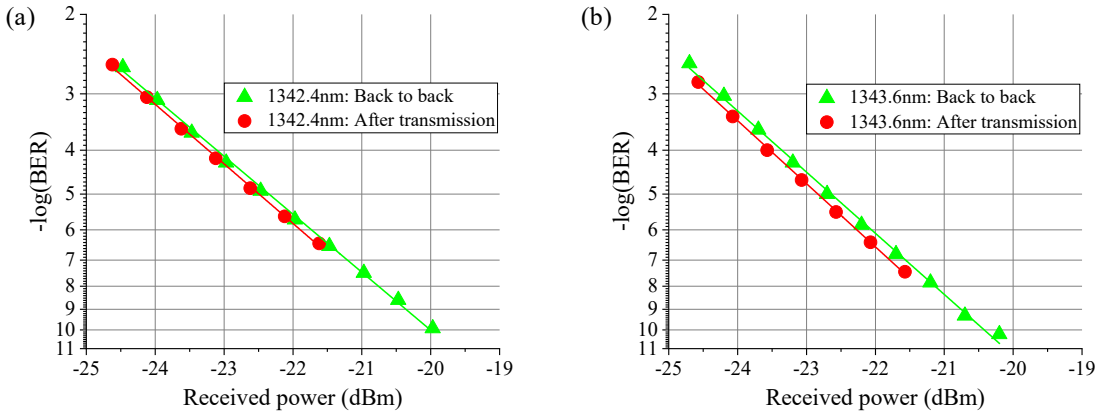

Figure 5-9: BER curves of the two-channel DWDM transmission for back-to-back and after 140-km transmission. The symbols, both triangles and circles, in the plots represent the measured BERs and the lines are the linear fit of those sets of measured data.

5.4 Nonlinear Performance of SOA and BDFA

Since some evidence of FWM was seen in the DWDM transmission experiments, it was constructive to perform some additional measurements of nonlinear performance of the SOA and BDFA. The setup for this measurement is shown in Figure 5-10. The measurement performed at the wavelength of 1341nm (or λ_3 in the previous transmission experiments). To provide sufficient power to perform the test, when one amplifier was being tested for its nonlinear performance, the other was used as the transmitter booster. After filtering the out-of-band ASE with the optical bandpass filter, a constant attenuation was applied to the amplified signal to prevent saturation of the photodetector. Finally, the BER was taken at the receiver as a function of input power to the amplifier under test (DUT) to determine its nonlinear performance.

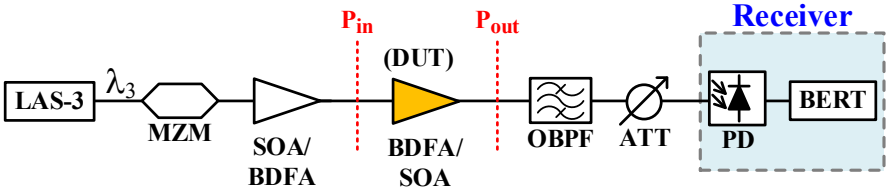

Figure 5-10: Experimental setup to measure the nonlinear performance measurement of SOA and BDFA.

The BER result of the BDFA performance is presented in Figure 5-11 (a) for a range of input powers from -13dBm to 10dBm. Figure 5-11 (b) shows further plots (the output power and gain) to indicate the saturation power of the BDFA, which happens at a -10-dBm input power (at 3-dB gain compression point). The BER curve of the BDFA is linear, implying that the BDFA exhibited no measurable nonlinearity, even when operated in deep saturation. This is to be contrasted to the performance of the SOA, see Figure 5-12 (a) for its nonlinearity measurement, which possesses a "u" shaped curve, with a minimum BER occurring at an input power of -10dBm, beyond this, BER increases rapidly. Figure 5-12 (b) shows that the 3-dB gain compression point for the SOA occurred when the input power was -3.5dBm, suggesting that signal degradation occurs due to saturation effects, such as patterning [110] [111]. It is important to note that the absolute values of BER (shown in Figure 5-11 (a) and Figure 5-12 (a)) should not be compared between the BDFA and SOA in this measurement, as each test was effectively performed using different booster amplifiers.

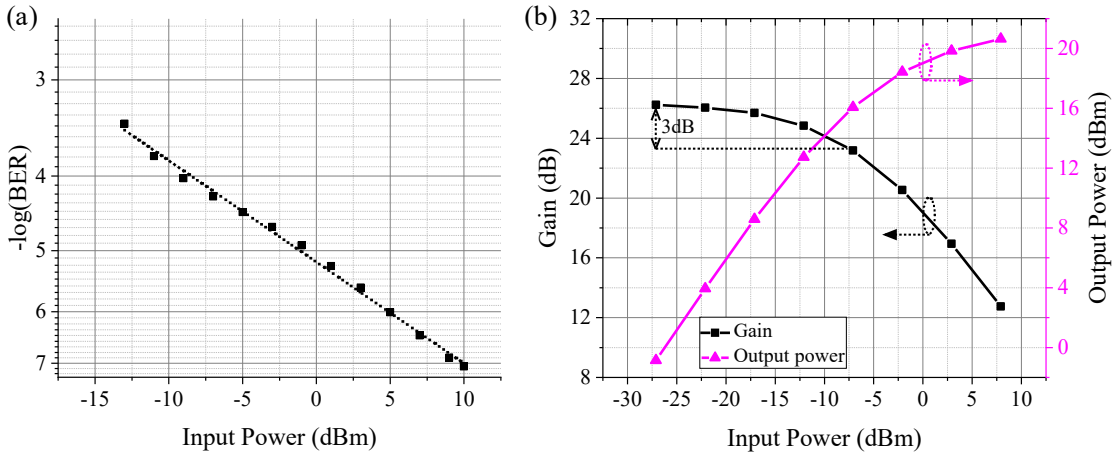

Figure 5-11: BDFA performance measurements at 1341nm in terms of (a) BER curve for nonlinearity measurement when varying the input power into the BDFA (the dashed line represents the linear fit) and (b) the gain curve (16-dBm saturated output power) [28].

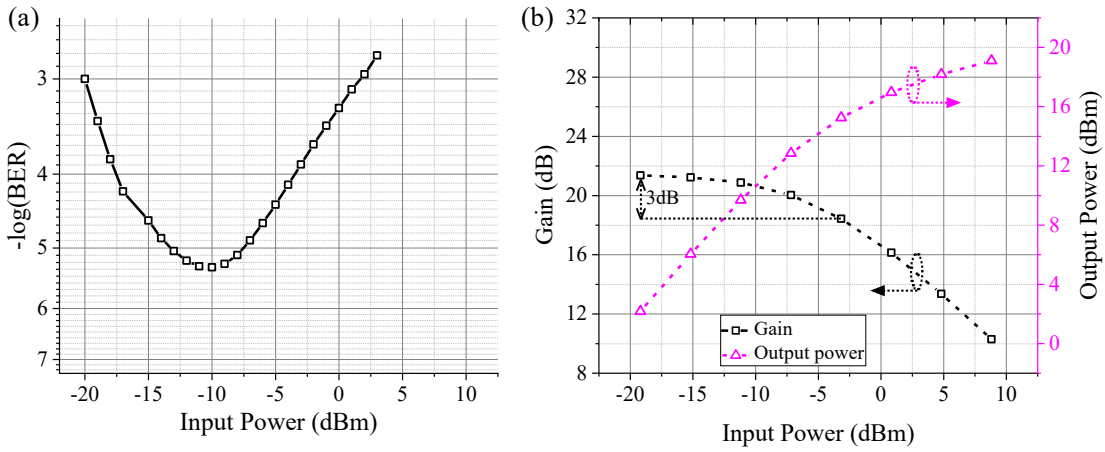

Figure 5-12: SOA performance measurements at 1341nm in terms of (a) BER curve for nonlinearity when varying the input power into the SOA and (b) the gain and power saturation characteristics (15.3-dBm saturated output power) [61].

5.5 Conclusion

The work in this section was carried out to demonstrate the capability of the BDFA for use in actual WDM transmission after its performance (in terms of gain and NF) was investigated (presented in Chapter 3 and Chapter 4). The WDM transmissions were performed in both CWDM and DWDM scheme with ~10Gbit/s OOK signals. The results from the CWDM cases (transmission with four channels and six channels) prove that using the BDFA as an in-line amplifier with a broad bandwidth of 50nm (~8.3THz) (in this study from 1321-1371nm), over at least 100km of SMF-28e is achievable with negligible receiver sensitivity penalty. The DWDM results (even in the longest reach case of 140km) also show a similar conclusion of negligible power penalty at the receiver. Together these results support the suitability of the BDFA for use in practical DWDM systems with channel spacings as close as 100GHz. In all experiments, the main limitation in channel counts came from SOA gain and useable output power, whilst the transmission reach was imposed by the available power at the receiver. The additional nonlinear studies show that the BDFA exhibits no measurable nonlinearity, even when operated in deep saturation, in contrast to the behaviour of the SOA, which rapidly degraded signals when operated under saturation.

For future demonstrations, we anticipate that the use of an additional BDFA as either an in-line amplifier and/or a pre-amplified receiver will facilitate an extended transmission reach in O-band transmission. Further investigations could include testing whether the BDFA is transparent to C-band light (so that O+C, multi-band transmission can pass through the same amplifier).

Chapter 6

Alternate-Mark Inversion for Nonlinearity Mitigation in O-band Transmission

6.1 Introduction

So far in this thesis, a number of characterisations for the SOA and BDFA under test have been provided. After this, the SOA and BDFA were applied to the demonstration of the first amplified WDM transmission in the O-band, with a recorded reach of 140km in SMF-28e, using a simple OOK signalling format. Some nonlinearities were, however, observable in the band after transmission (either from inter-channel FWM or SPM in SOA), as discussed in the results section of the previous chapter. In the meantime, the higher loss of SSMF in the O-band compared to the C-band will likely encourage the use of higher optical launch powers to compensate the loss. However, increasing the launch power will in turn expose the system to higher nonlinear distortion. Furthermore, all other parameters being the same, Kerr nonlinearity is approximately 1.5 times stronger in the O-band (at 1310nm) than in the C-band (at 1550nm), as indicated by the equation for the nonlinear coefficient, $\gamma = \frac{2\pi}{\lambda}\frac{n_2}{A_{eff}}$

(assuming that n_2 is constant across the two bands [112], the mode-field diameter (MFD) at the 1310-nm and 1550-nm wavelengths is ~9.2μm and ~10.4μm, respectively [5] and $A_{eff} \propto \mathrm{MFD}^2$). Coupled with the comparatively lower dispersion in the O-band compared to the C-band, which would otherwise help to suppress nonlinear impairments (such as FWM and XPM [41]), practical and cost-effective methods for mitigating nonlinear distortion will likely be all-the-more valuable in the O-band.

So far, direct-detection formats have proven to be more cost effective than coherent formats [113] [114] and given the comparatively higher loss of O-band transmission in a typical SMF, it is likely that amplified WDM O-band transmission will see its first application in high-capacity, but relatively short-haul, direct-detection transmission links. The partial response formats, alternate-mark inversion (AMI) and duobinary (DB), have been the subject of many demonstrations, with the former known for its nonlinearity mitigation and the latter for its CD tolerance [41]. Despite being relatively well-studied in C-band transmission, there is a comparative lack of demonstrations of these formats in the O-band, where the ecosystem is markedly different.

In this chapter, the effectiveness of these partial response formats in the O-band will be investigated. The name 'partial response' derives from the application of an additional, non-data-carrying modulation to the signal which is used to improve its transmission characteristics, and which is not detected at the receiver. For understandability, the concept of (classic) 2-level AMI and DB will be introduced in Section 6.2 and the results of an experimental study will be presented and discussed in Section 6.3. Afterwards, these concepts will be extended to their 4-level equivalents and their first ever demonstration will be presented and discussed in Section 6.4. In both cases, the implemented partial response formats will be compared to their traditional intensity modulation and direct detection (IMDD) counterparts, i.e., OOK and 4-level pulse amplitude modulation (PAM4). The benefit of these partial response formats is examined when using the different available amplifiers, the SOA and BDFA, given that the former tends to exhibit higher nonlinearity than the latter. After this, in Section 6.4.2, the results of a simulation study will be presented to provide a comprehensive understanding of the operating mechanism of partial response formats. Finally, the results of this chapter will be concluded altogether and presented in Section 6.5 with some directions for future work suggested. Note that the work presented in this chapter was reported in Publications 5, 6, and 7 listed in the

Publications as First Author section. It is reminded that the characteristics of the SOA and the BDFA used in this chapter were presented in Chapter 3 and Chapter 4.

6.2 Partial Response Formats

A partial response format is a correlative-coding data modulation format [41] which enforces a correlation between the encoded data and some other property of the optical wave, e.g., phase. The benefit of appropriate partial response modulation in optical transmission is the improvement of the IMDD signal's robustness against some transmission impairments, e.g., inter symbol-interference due to dispersion and nonlinearity, which can be achieved by means of the auxiliary-phase modulation [41].

To explain the application of auxiliary-phase modulation in partial response formats, Figure 6-1 presents an illustration of a code word '1011001' encoded using both OOK, AMI, and DB (Figure 6-1 (a), (b), and (c), respectively). Plots of the optical field and detected power envelope are presented, along with phasors indicating the corresponding phase for each transmitted symbol. In all three cases, the oscillatory optical field can be seen when a '1' bit is transmitted, with the notable difference being the presence of 'π' phase shifts in the AMI and DB examples, which are absent in the OOK example.

The phasor (or constellation) diagrams corresponding to the presented OOK, AMI, and DB formats are presented in the right side of Figure 6-1 (a), (b), and (c), respectively. For OOK, it can be seen that there are only two points in the signal's constellation, whilst AMI and DB have three points, due to the additional π-phase shifted symbols which must be transmitted.

Given the use of a square-law detector, the receiver is blind to the underlying phase of the symbols and hence will only respond to their power envelope (hence AMI and DB being described as partial response formats). Square-law detection means that the signals captured at the receiver both appear as simple OOK signals, meaning that all of the formats can be detected using the same receiver, a notable benefit of the adoption of these partial response formats compared to more complicated alternatives. This is illustrated in the 'detected signal' in Figure 6-1, where it can be seen that, regardless of the format and the underlying phase shift in OOK, AMI or DB, the power envelope remains unchanged.

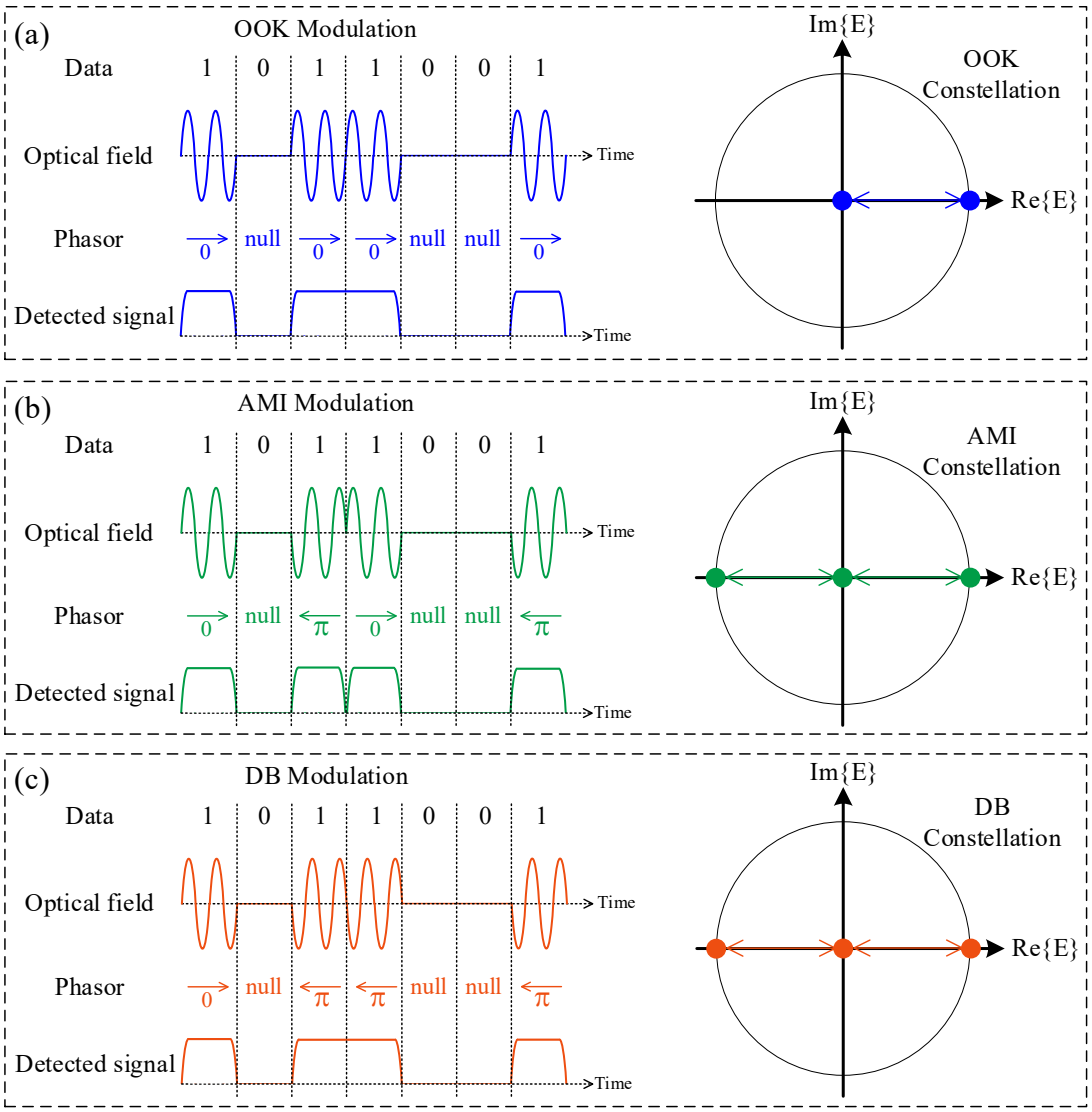

Figure 6-1: Illustrations of the optical waveform, phasor, detected (power) waveform, and constellation diagram of (a) OOK, (b) AMI, and (c) DB. Re{E} and Im{E} denote real part and imaginary part of the complex optical field (E), respectively.

The partial-response modulation formats that will be discussed in this chapter, AMI and DB, will be presented in more detail in the following sections.

6.2.1 Alternate-Mark-Inversion

The simplest way to describe AMI is by its rule for its auxiliary-phase modulation:

- A non-zero symbol **always** has a π-phase shift relative to its nearest preceding non-zero symbol [41].

This rule implies that a consecutive series of '1's will have an alternating 0 – π phase shift and if the format is implemented using a dual-drive MZM (DD-MZM), the waveform will be a form of return-to-zero (RZ) signalling, with the power passing through zero every time there is a π-phase shift. The repeated phase alternation of AMI is known to improve the performance of IMDD signals with respect to nonlinear inter-symbol interference by suppressing intra-channel FWM-induced ghost pulses [115] [116] [117] [118]. An illustration of this ghost-pulse suppressing ability is provided in Figure 6-2. On the top row (Figure 6-2 (a)), a short sequence of an AMI signal in the time domain (corresponding to the codeword '11011') is shown, without any distortion. Exposure to SPM and dispersion will lead to the formation of ghost pulses before and after each symbol, as shown in Figure 6-2 (b). Without the application of AMI to these signals, the overlapping ghost pulses from the two '1' symbols would interfere constructively, raising the power of the '0' symbol and reducing the eye opening of the signal. However, when AMI is applied, these ghost pulses will possess a π relative phase shift, resulting in destructive interference and helping maintain an open eye. Detailed explanation of the observable benefits of AMI will be provided in the work presented in Section 6.3 and Section 6.4.

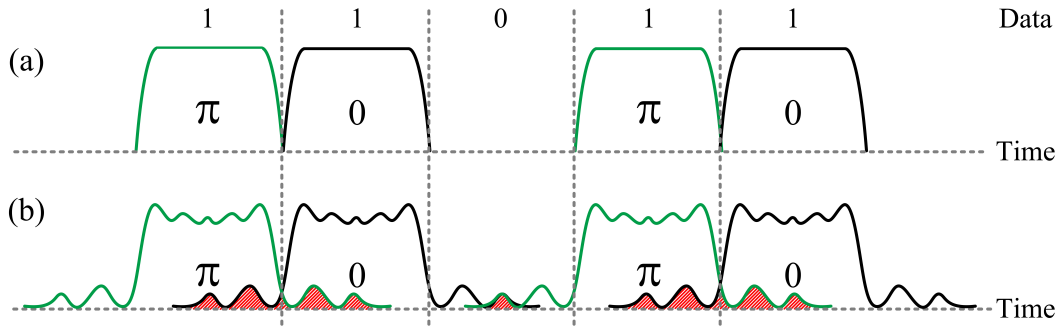

Figure 6-2: Illustration of the optical power waveform of AMI (codeword '11011') showing destructive interference between ghost pulses – (a) the waveform in its initial state and (b) the waveform after experiencing SPM and dispersion. The shaded areas (red) indicate ghost pulses experiencing destructive interference. The 0 and π labels denote the symbol phase.

There have been a number of notable experimental studies demonstrating the benefit of AMI in optical transmission. In a C-band study involving the transmission of an AMI signal over 1920km of SSMF using EDFA and Raman amplification, a reduction in BER of about two orders of magnitude (~3dB Q-factor improvement) was observed compared to a similar RZ-OOK signal [115]. However, in another C-band study using

2000km of non-zero dispersion shifted fibre (NZDSF) and dispersion compensation with DCF [117], the authors found a much smaller ~1dB Q-factor improvement. This was understood to be due to the relatively smaller dispersion [115] [117] and it is thought that improvements in signal quality using AMI are due to the mitigation of degradation caused by the combination of dispersive and nonlinear effects, rather than nonlinearity alone [116] [117]. Although the dispersion is low in the O-band, it is not zero and often no attempts are made to physically compensate the dispersion of the transmission link (e.g., using DCF). The discussed studies support the idea that there may be an advantage to adopting AMI in the O-band, given its uncompensated dispersion [116] [117].

6.2.2 Duobinary

Like AMI, duobinary (DB) modulation is best described by its rule for phase modulation:

- A non-zero symbol has a π-phase shift relative to its preceding non-zero symbol **only** if they are separated by an odd number of zero symbols [41].

In contrast to AMI, in DB consecutive non-zero symbols will all possess the same phase and DB tends to look much like a regular non-return-to-zero (NRZ) OOK signal. The well-known advantage of DB is improved dispersion tolerance compared to traditional binary OOK signals. This is because the encoding scheme of the DB signal causes ISI to be destructive to the underlying optical field (since interfering symbols will have a π-phase shift relative to each other) [41]. An illustration of this ability to suppress ISI is provided in Figure 6-3. On the top row (Figure 6-3 (a)), a short sequence of a DB signal in the time domain (corresponding to the codeword '11011') is shown, without any distortion. Exposure to dispersion will lead the edges of the '1' symbols to broaden and, in extreme cases, overlap. Without the application of DB coding to these signals, the overlapping symbol edges would interfere constructively, raising the power of the '0' symbol and reducing the eye opening of the signal. However, when DB is applied, these ghost pulses will possess a π relative phase shift, resulting in destructive interference and maintaining an open eye. The dispersion tolerance in the frequency domain can be seen by the narrower bandwidth of DB relative to OOK.

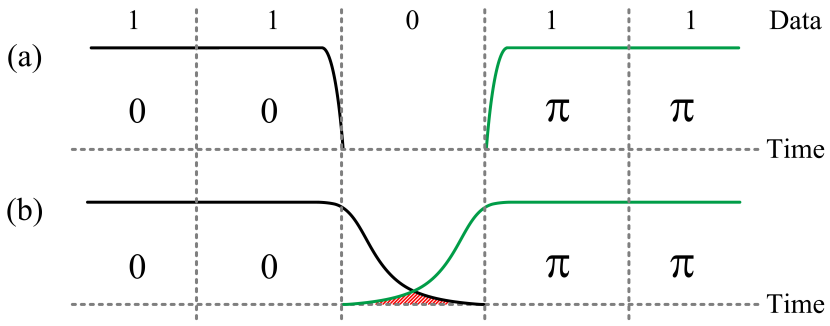

Figure 6-3: Illustration of the power waveform of DB (codeword '11011') showing destructive interference – (a) the waveform in its initial state and (b) the waveform after experiencing dispersion. The shaded area at the middle indicates the destructive interference. The 0 and π labels denote the symbol phase.

Although dispersion in the O-band region is relatively low compared to the C-band, where the dispersion tolerance of DB has most often been demonstrated [41] [119] [120], the dispersion of the O-band still has an impact upon the performance of direct-detection formats, especially at longer wavelengths and at higher baud rates. Indeed, there have been a number of demonstrations of techniques to avoid fading in the O-band (which can occur for signal bandwidths as low as ~20GHz [121]), such as single-sideband modulation and Kramers–Kronig (KK) detection [122]. As such, it is still useful to demonstrate the performance of DB in the O-band and its performance to help separate the effects of dispersion and nonlinearity on the tested OOK and AMI signals in the O-band transmission tests.

6.3 2-level Formats

Firstly, the 'traditional' binary versions of AMI and DB will be demonstrated in the O-band. During this demonstration, no BDFA was available and the SOA was the only O-band amplifier that could be used at that time. As such, the SOA was used as a booster amplifier and an unamplified photodiode was used at the receiver.

The benefits of AMI and DB signalling (improved nonlinearity tolerance and improved dispersion tolerance, respectively [41]) derive from their underlying phase modulation and corresponding power waveform. Hence, these advantages can be obtained regardless of the approach by which these formats are implemented. For example, several techniques have been demonstrated for the generation of partial response

waveforms including, using an optical delay line interferometer [117] [118], using a delay-and-add circuit in the electrical domain [41].

In this work, we apply the rules defined above for generating AMI or DB during an encoding stage applied to the logical data prior to up-sampling and pulse shaping, which were implemented using offline DSP in MATLAB.

6.3.1 Signal Generation Methodology

The requirements for the generation of OOK are different from those for the generation of AMI and DB, as the former has no need to impart an auxiliary phase modulation upon the signal whilst the latter two formats do. However, in the interests of comparing the performance of the studied formats themselves, rather than the performance of their implementation, we designed a realistic testbed which could be used to generate all three formats without modification, keeping the effective cost of implementation constant and providing a fair performance comparison between them. Note that, once again, this auxiliary phase encoding does not affect the IMDD square-law detection and so no modification was needed at the receiver.

The inset of Figure 6-4 shows a simple visualisation of the commonly used MZM in optical telecommunications that contains two electrical drive ports: 1) a high-speed data port driven by an AC RF signal and 2) a low-speed biasing point driven by a DC signal used for biasing the modulator. It is known that if the phase modulation of an ideal MZM depends linearly on the drive voltage (phase $\propto$ voltage) [41] [123], the power transfer function (T_P) will only rely on the differential drive voltage between the two arms (ΔV) and the bias voltage (V_{bias}) which can be given by Equation 6-1, derived in [41].

$$T_P = cos^2\left(\frac{k\Delta V}{2} + \frac{kV_{bias}}{2}\right) \quad \text{Equation 6-1}$$

where, k is the linear factor of the relationship between phase and drive voltage of the modulator.

As shown in Equation 6-1, changes in the differential drive voltage, ΔV, in an ideal DD-MZM, impart no phase shift on the modulated signal. An analytical plot of the normalised power transfer function of such an ideal device as it varies with the bias voltage is provided in Figure 6-4.

To modulate an optical signal, the fast RF data port is normally driven with a bipolar RF data signal, which drives the operating point of the modulation about a fixed 'centre' point on the power transfer curve of the modulator whose location is determined by the bias voltage. The transfer curve of Figure 6-4 has been labelled to illustrate the extent of the RF data drive voltage for each format and the bias points for the cases of OOK, AMI, and DB.

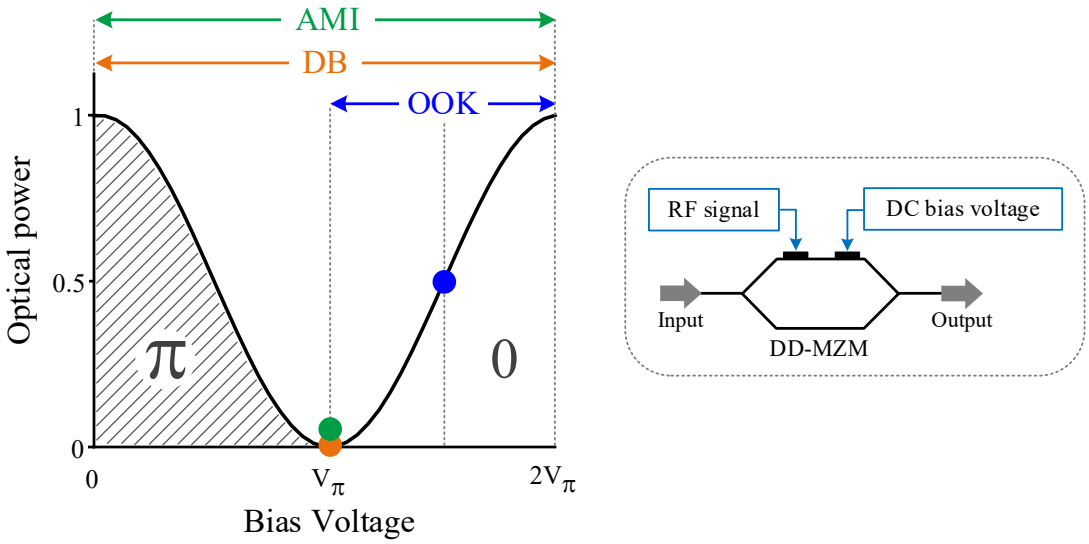

Figure 6-4: Modulation transfer function with specification of the location of the bias point (circle) and the voltage range of the RF signal (arrow) of the OOK, AMI, and DB in blue, green, and orange, respectively. V_π is the voltage for switching the modulator output from full transmission to full extinction, which is equivalent to the voltage required to induce a phase shift of π. The inset is a MZM diagram with electrical driven ports.

To generate OOK signals, the modulator is biased at the point indicated by the blue circle in Figure 6-4 (known as the quadrature point). It can be seen that keeping the peak-to-peak voltage (V_{pp}) of the RF signal to be less than V_π ($V_{pp} \leq V_\pi$) provides a one-to-one mapping of drive voltage into optical power suitable for the generation of the purely intensity-modulated OOK signal. The one-to-one mapping that exists in this scenario means that a 2-level electrical drive signal is required for OOK generation that is reminiscent of the optical OOK signal itself, as shown in the top row in Figure 6-5 (for convenience, optical waveforms are illustrated along with the RF signals that are used to generate them).

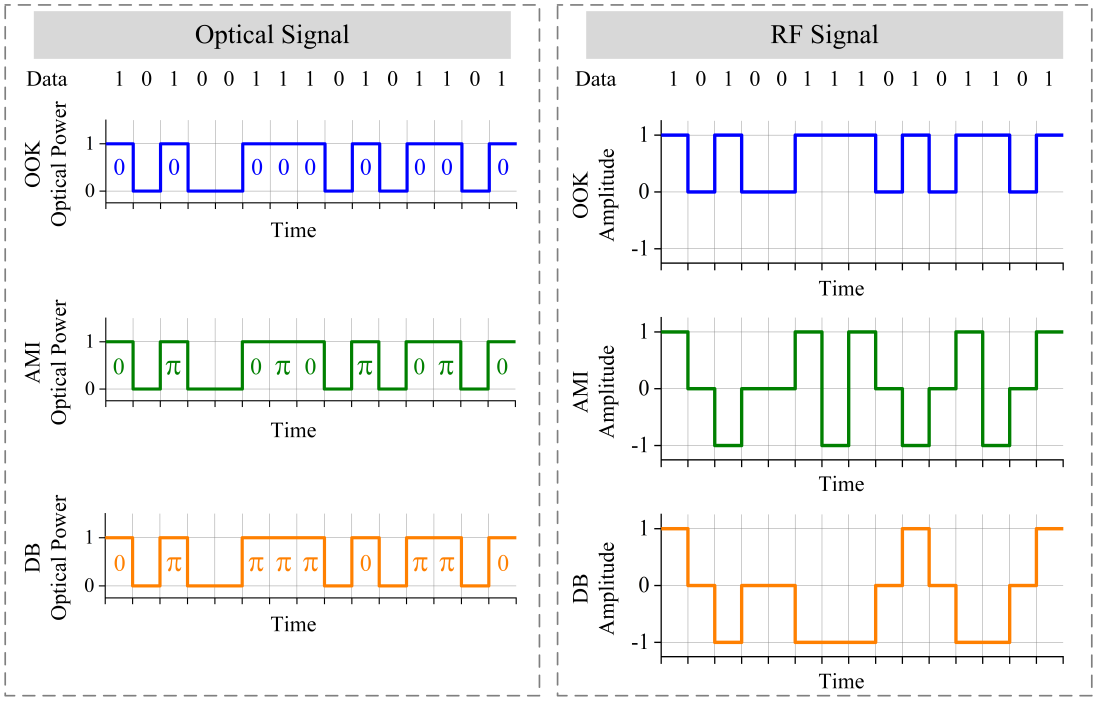

Figure 6-5: OOK, AMI, and DB in the domain of optical power (left) and RF signal (right) for side-by-side representation. The amplitude and square shape of the waveforms are only for visualisation, and do not reflect the pulse shape of the signals in the experiments.

In contrast, for the generation of AMI and DB, we must be able to produce, with the same modulator, signals with a relative π-phase shift between them. As such, for the generation of AMI or DB signals, the modulator is biased at the point indicated by either the green or orange point in Figure 6-4 (known as the minimum point). In this configuration, driving the RF port either positively or negatively by the same magnitude voltage would result in an optical output of an equal optical power but opposing phase and therefore, keeping the total drive voltage $\leq 2V_\pi$ allows for the optical signal to be modulated in power with the desired phase. Both AMI and DB each express 3 different optical states, as, in addition to the 'zero' symbol present in all of the discussed formats, the non-zero symbols must be transmittable with either a 0 or π phase shift, which gives rise to the constellation diagram that we discussed earlier in Figure 6-1 (b) and (c) for AMI and DB, respectively. After modulation, the resulting power profile of the optical signals resembles that of OOK.

6.3.2 Experimental Setup

Figure 6-6 shows the testbed used in this work to investigate the performance of a single-channel transmission link in terms of robustness to nonlinearity for the purpose of reach extension in O-band data transmission. For convenience, some relevant parameters are tabulated in Table 6-1.

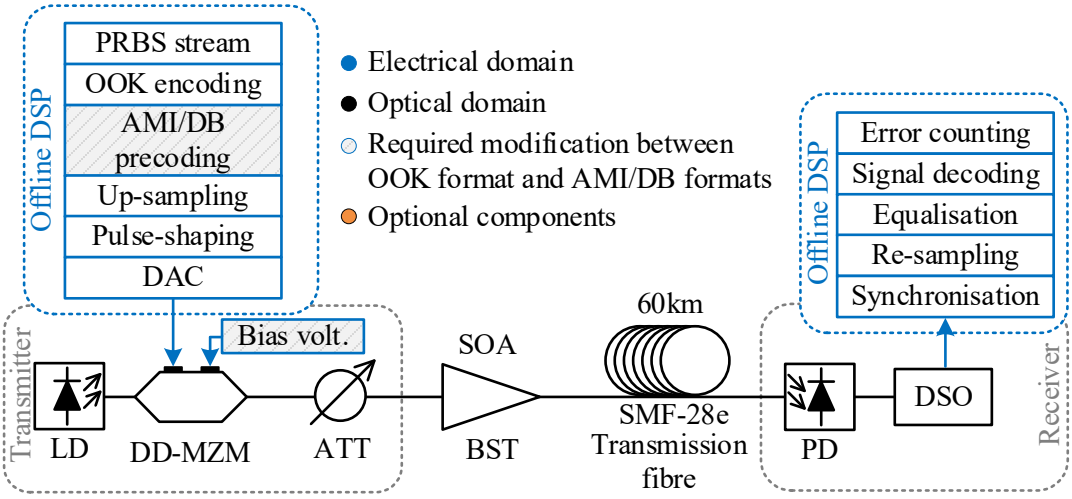

Figure 6-6: Experimental setup for the 2-level formats, including the block diagrams for offline DSP used at the transmitter and the receiver.

2-level Format Transmission	Value
Carrier wavelength	1343.2 nm
Max launched power into transmission fibre	13 dBm
Transmission fibre length	60 km
Bit rate (baud rate)	32 Gb/s (32 GBd)
Tx up-sampling rate	90/32 GSa/s
Tx DAC	8 bits
Rx re-sampling rate	1/8 GSa/s

Table 6-1: Signal generation and detection parameters for the 2-level signals transmission.

At the transmitter, a distributed feedback (DFB) laser diode (LD) is used to produce an optical carrier at the wavelength of 1343.2nm. The carrier signal is then passed to a DD-MZM to be modulated with a pre-coded data waveform with the modulator set at the corresponding bias voltage for each format (shown by the blue input arrows in Figure 6-6). The bandwidth of the modulator is 32GHz. The block diagram at the

transmitter side in Figure 6-6 shows the offline DSP used to generate the data waveform, the process of which is as follows (note that, for the encoding step and all stages of the receiver, I developed the code myself using MATLAB):

- From the top DSP block, one 2^{15}-1 pseudorandom binary sequence (PRBS) stream is encoded onto an IMDD OOK symbol stream.
- A precoding step is added for generating AMI and DB waveforms, which follows the rules for RF signal generation described in the previous section.
- Then, an up-sampling step is required to match the signal symbol rate to the sampling rate of an arbitrary waveform generator (AWG) device (sampling rate is 90GSa/s).
- Afterwards, the up-sampled signal is filtered by a raised-cosine filter with a 0.35 roll-off factor (this value is chosen to ensure that the bandwidth of the detected signal lies well within the 32GHz bandwidth of the digital storage oscilloscope (DSO)) for pulse shaping.
- Subsequently, the digitally processed data stream is uploaded to digital-to-analogue converter (DAC) module of the AWG whose output is directly connected to the DD-MZM. The vertical resolution of the DAC is fully occupied for all formats, IMDD and the partial response, with the RF power adjusted as needed.

At the modulator output, the optical signal power is then varied using an optical attenuator (ATT) to observe the response of the O-band SOA at various input powers. The gain of the SOA is sensitive to the polarisation of the signal and therefore needs to be operated in conjunction with a polarisation controller placed at its input. Afterwards, the signal is fed into the transmission fibre, which is SMF-28e.

At the receiver, a photodetector (PD) is used directly after transmission. An optical bandpass filter was found to be unnecessary as the link reach was limited by received power rather than out of band noise. The optical power detected at this point was dependent upon the launch power and the reach. Next, the detected signal is captured by a DSO with a sample rate of 80GSa/s. The captured output waveform is passed to an offline DSP unit to process the signal (see block diagram in Figure 6-6). The processing steps of the offline DSP at the receiver are described below:

- From the bottom of the DSP block, the waveform is synchronised and re-sampled to prepare for the processing data in the next stage.
- A decision-feedback equaliser (DFE) is used here for equalisation in conjunction with a recursive least squares (RLS) algorithm. The number of the DFE's forward taps, feedback taps, and RLS's forgetting factor are 12, 11, and 0.99, respectively.
- Finally, the equalised signal is decoded based on thresholds determined by a histogram of the signal intensity levels and the signal performance is determined through a BER measurement by direct error counting.

6.3.3 Experimental Results

As there was no receiver amplifier, the linear system performance was limited by the received power, which in turn was limited by the SOA output power and behaviour under saturation. As the SOA was known to exhibit nonlinear behaviour under saturation (as shown in Section 5.4), the SOA was considered to be part of the link and the power launched into it varied to study the benefit of the AMI and DB formats in mitigating the nonlinearity of both the SOA and the transmission fibre.

The SOA offered a gain between 19dB and 21.7dB, depending upon the input power, resulting in output powers between 9.7dBm and 13dBm, which were subsequently launched into the fibre. The transmission distance in the SMF-28e was 60km, equivalent to a loss of ~20dB.

For the three formats investigated, Figure 6-7 shows spectra before and after the SOA to illustrate the signal distortion caused by amplification in the SOA as well as the spectra at the receiver after transmission over 60km of SMF-28e fibre. The carrier suppressed nature of the AMI and DB signals compared to OOK can easily be seen in these spectra and arises from the repeated phase shifting of the former two formats. It is interesting to observe that amplification induced considerable nonlinear distortion on the signal and this can be seen as asymmetry in the spectra after the SOA (see the grey and pink spectra). After transmission, the nonlinear distortion due to the Kerr effect of the fibre has caused notable spectral broadening (see the pink and blue spectra).

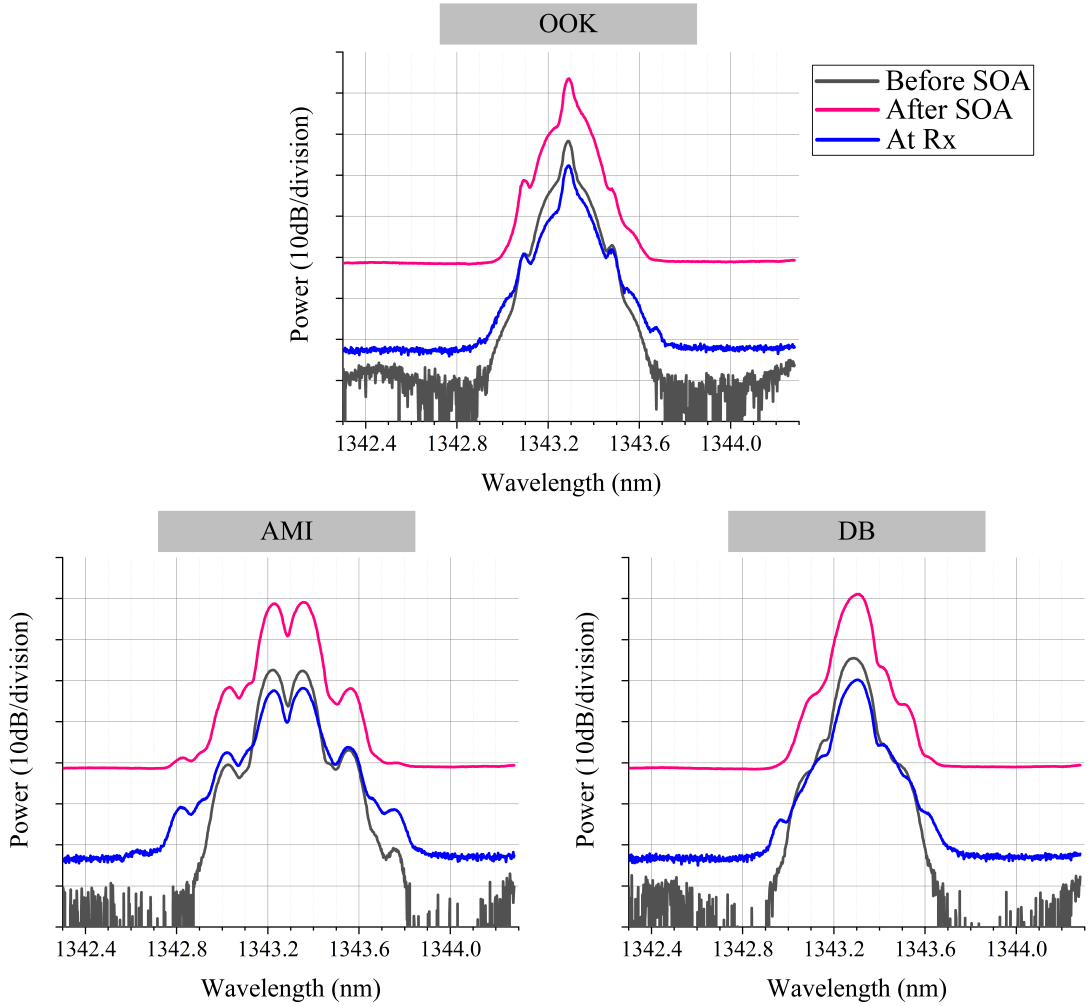

Figure 6-7: Spectra of the 2-level signals at the SOA input (Before SOA), SOA output (After SOA), and at the receiver after 60-km transmission (At Rx). These spectra were captured by using an OSA with 0.01-nm resolution.

A more intuitive picture of these results can be seen in the eye diagrams shown in Figure 6-8. Eye diagrams are presented for the three formats, at three different launch powers into the fibre, points A, B, and C. The characteristic of each point is as follows: Point A – negligible nonlinear distortion, Point B – nonlinear distortion has started but signals still detectable, and Point C – signals are heavily deteriorated by nonlinearity. At point A, the AMI format can be seen to have a wider eye opening than the DB or OOK and this is due to the RZ nature of the AMI. For points B and C, the AMI is far less distorted than the OOK and DB, confirming the improvement in nonlinear tolerance.

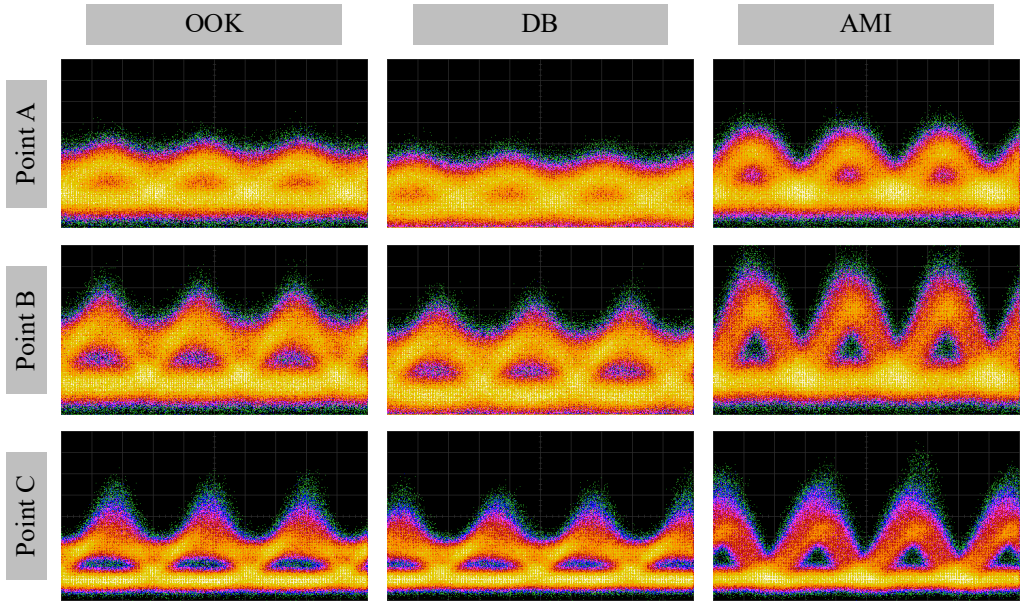

Figure 6-8: Eye diagrams after 60-km transmission at various launch powers into fibre, points A, B, and C in the BER curves. These eye diagrams were measured/captured using a sampling oscilloscope.

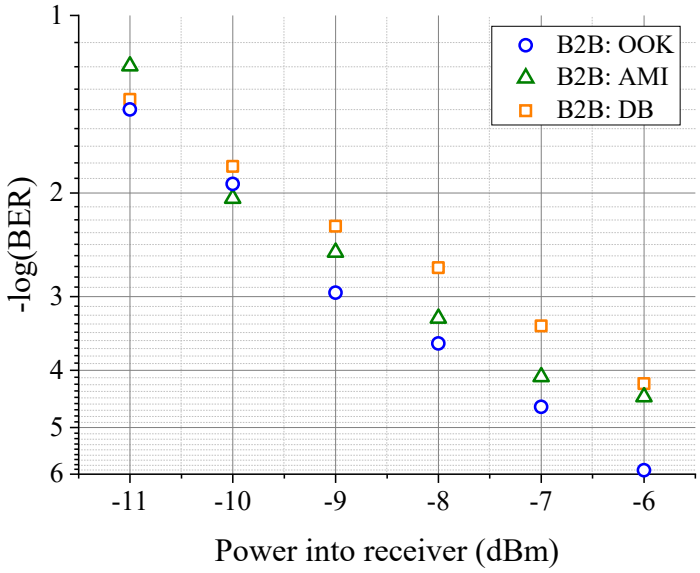

Figure 6-9: Back-to-back BER results for the OOK, AMI, and DB.

Finally, BER plots are present before and after transmission so that the improvement in performance due to the adoption of AMI can be quantified. Figure 6-9 provides a back-to-back (B2B) measurement of BER versus received optical power. The data were taken immediately after the modulator and with the SOA and transmission fibre bypassed. It can be seen that all three formats show performance within ~0.5dB of each other, although the OOK is slightly better than the other two formats, possibly

due to the use of the full DAC range of our driving AWG for only two levels, rather than three.

Figure 6-10 provides plots of BER as it varies with the launch power into the fibre (equivalent to the output power of the SOA) for the three formats taken after the SOA and transmission fibre. BERs were measured for various powers launched into the fibre (by adjusting the input power of the SOA). In this case, there is a marked difference in the performance between the three formats. For powers less than 11.5dBm, OOK and DB can be seen to offer similar performance. This is to be expected, as they possess very similar waveforms in the time domain. For powers higher than 11.5dBm, the OOK signal is quickly degraded, becoming unable to reach the 7% hard-decision forward-error-correction (FEC) limit (BER $= 3.8 \times 10^{-3}$ or $-\log(\text{BER}) = 2.42$), and is outperformed by DB. The AMI, in contrast, shows much better performance, reaching an optimum BER for a launch power of 12.4dBm at point Q_3 with the Q-factor (converted from the BER) of 12.7dB. For the OOK and DB, the optimum launch powers are lower than that of the AMI case (see points Q_1 and Q_2) which give the Q-factor of 8.03dB and 8.9dB, respectively. Correspondingly, the two partial response formats provide improvement in Q-factor compared to OOK of 0.87dB for DB and 4.67dB for AMI.

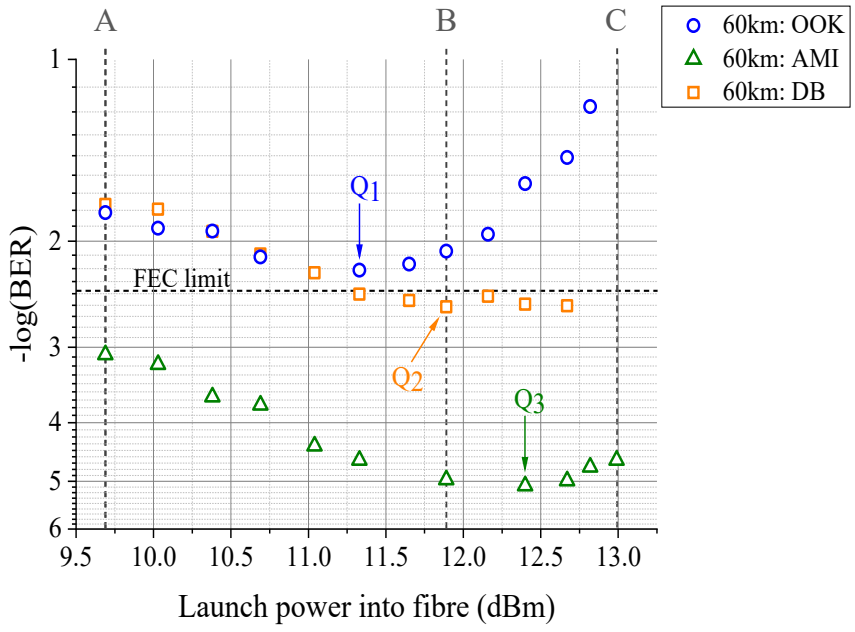

Figure 6-10: BER curves after the 60-km transmission as it varies with launch power into the fibre (equivalent to the output power of the SOA). Points A, B, and C indicate each signal's eye-diagram measurement point. Points Q_1, Q_2, and Q_3 denote the BER at optimum launch power of each signal.

6.4 4-Level Formats Experimental Transmission

The success of the 2-level AMI experiment and the industry adoption of PAM4 for 400G links [74] motivated the following study into combining these two concepts. In this section, we demonstrate for the first time, the combination of AMI signalling with a higher order IMDD signal, traditional PAM4, which we refer to as 4-level AMI (AMI4), to mitigate nonlinearity in the O-band. The transmission performance of AMI4 was compared to that of conventional PAM4 as well as to a 4-level adaptation of DB (DB4). In this experiment, a 40-Gb/s single-channel signal was transmitted over several tens of km of SMF-28e and used a booster amplifier to provide sufficient launch power. In this experiment, the BDFA had become available and so the amplifier was selected from either the SOA or the BDFA.

6.4.1 Experimental Work

The experimental setup used to generate the PAM4, AMI4, and DB4 symbols is shown in Figure 6-11 and is very similar to that shown in Section 6.3.2 (only the precoding step in the DSP block at the transmitter is different). Parameters for this experiment can be found in Table 6-2.

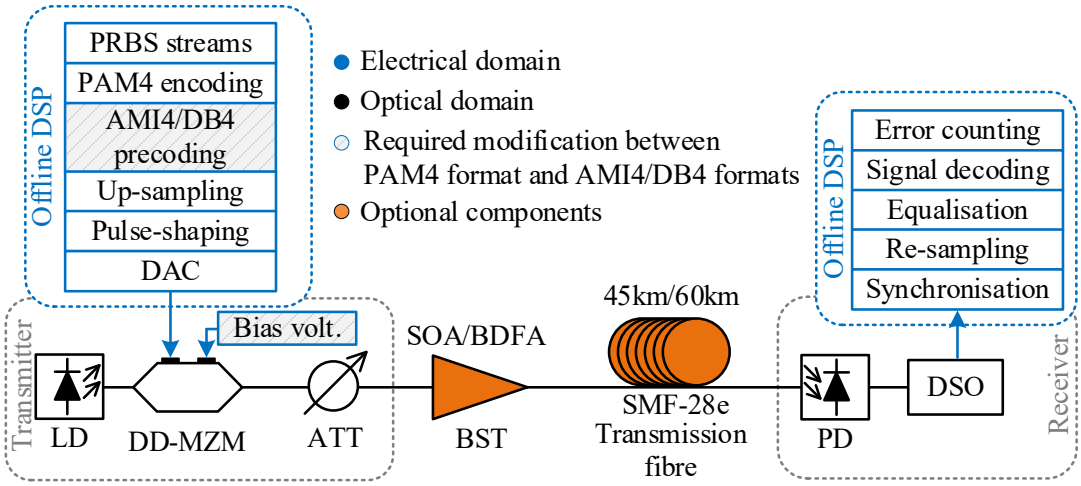

Figure 6-11: Experimental setup for the 4-level formats, including the block diagrams for offline DSP used at the transmitter and the receiver.

4-level Format Transmission	Value
Carrier wavelength	1330.7 nm
Max launch power into transmission fibre (boosted by SOA)	10.6 dBm
Max launch power into transmission fibre (boosted by BDFA)	14.4 dBm
Transmission fibre length for the SOA link	45 km
Transmission fibre length for the BDFA link	45 km / 60 km
Bit rate of 4-level formats	40 Gb/s
Baud rate of 4-level formats	20 GBd
Tx up-sampling rate	9/2 GSa/s
Tx DAC	8 bits
Rx re-sampling rate	2/8 GSa/s

Table 6-2: Signal generation and detection parameters for the 4-level signals transmission.

To generate the AMI4 and DB4 signals in this experiment, we need to translate the concept of 2-level partial response modulation to a 4-level equivalent. Although this is straight-forward for AMI, the same is not true for DB. There is more than one way to translate the concept of DB to its 4-level version and we selected a way which we believe retains the most commonly promoted benefit of DB, namely dispersion tolerance due to reduced optical bandwidth. As such, it was decided to apply a π-phase shift in DB only after passing through one or more '0' level symbols.

Figure 6-12 in the left column shows an illustration of the nominal signal power waveforms of PAM4, AMI4, and DB4 in the time domain, whilst the right column of Figure 6-12 shows the RF signals used to drive the modulator in each case. The RF drive waveforms required to generate AMI4 or DB4 signals visually appear as PAM7 signals to express the seven different optical states (the non-zero symbols with 0 and π phases (six states) and the zero symbol (one state)).

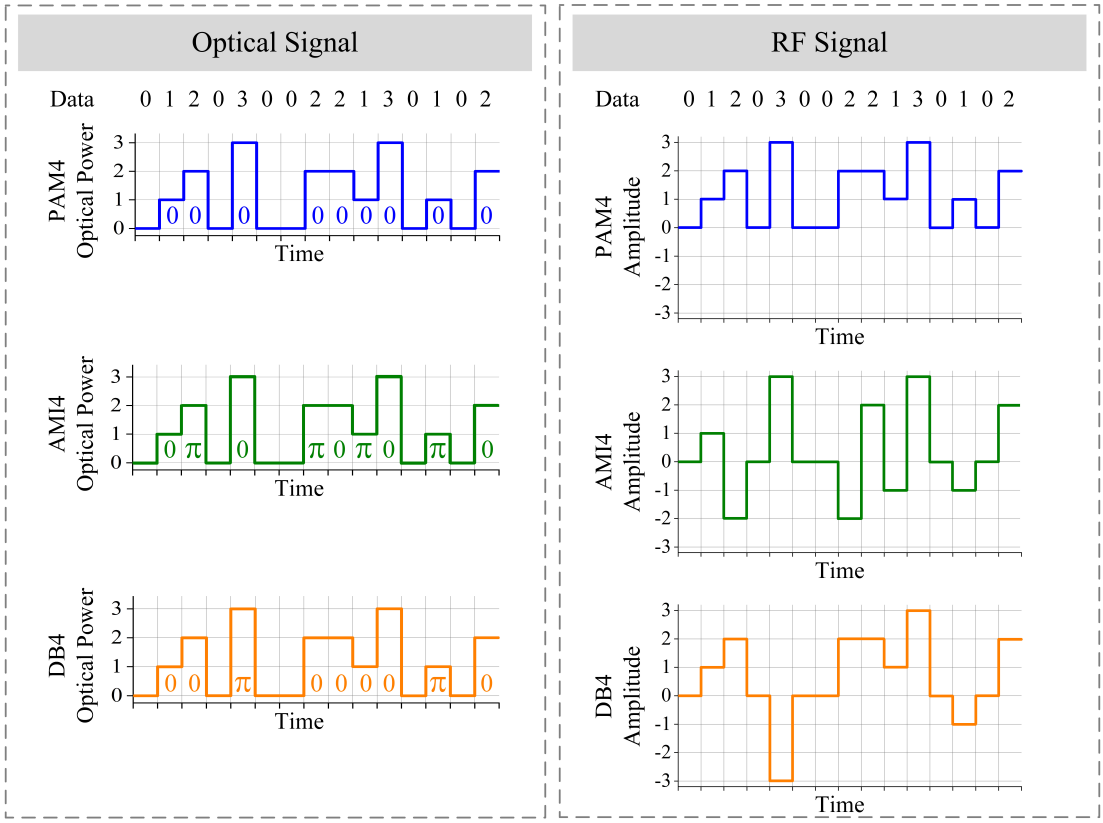

Figure 6-12: PAM4, AMI4, and DB4 in the domain of optical power (left) and RF signal (right) for side-by-side representation. Note that the amplitude and square shape of the waveforms are only for visualisation, and do not reflect the physical signals in the experiments.

To demonstrate the signal's transmission performance in this experiment, we then varied the input power into the booster amplifier from -20dBm to -8dBm whilst collecting a number of metrics, such as eye diagrams, spectra and BERs. The amplifier was selected from either the SOA or the BDFA, so that the influence that different amplifier-induced distortions may have on the signal performance could be considered. The SOA was set to provide a gain of ~18.6dB, resulting in a maximum launch power of ~10.6dBm into the SMF-28e and a transmission reach of up to 45km (corresponding to a 15.3-dB link loss). The BDFA was set to deliver a gain of 22.4dB and offered a maximum launch power of 14.4dBm. This higher value of launch power allowed us to extend the transmission reach to a maximum of 60km (corresponding to a ~20-dB link loss).

6.4.1.1 Back-to-Back

The results of back-to-back BER measurements for the AMI4, PAM4, and DB4 signals as a function of received power are plotted in Figure 6-13 (a) to show the performance of the system in the absence of a booster amplifier and the transmission fibre. Predictably, the PAM4 and DB4 signals, which exhibited similar intensity profiles, show comparable performance. AMI4 on the other hand, behaved like a RZ format, owing to the phase flip on each occurrence of a pulse, and as a result, outperformed the other two for a given average received power, i.e., offering a receiver sensitivity gain.

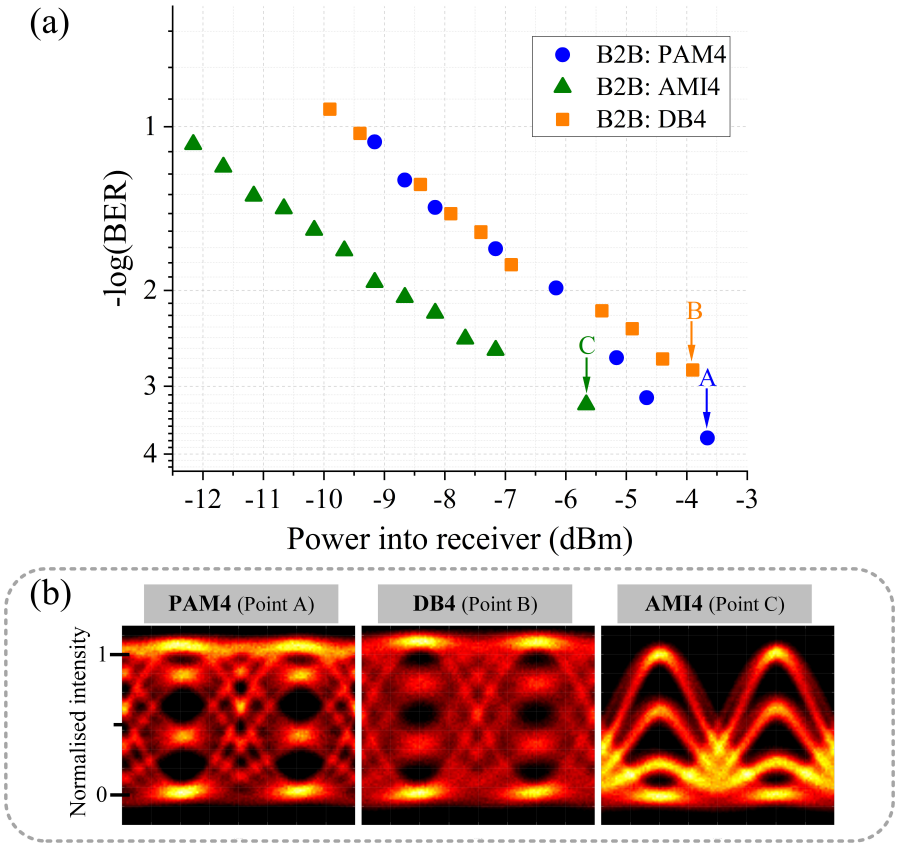

Figure 6-13: Back-to-back measurements (with the booster bypassed): (a) BER curves (b) eye diagrams. Note that the eye diagrams of each signal format were taken at their optimum point (lowest BER), represented by points A, B, and C for PAM4, DB4, and AMI4, respectively (in the BER curves). The amplitudes of the eye diagrams are normalised to the intensity of AMI4.

The B2B eye diagrams for each format are shown in Figure 6-13 (b). Their measurement points corresponded to points A, B, and C in Figure 6-13 (a) for PAM4, DB4, and AMI4, respectively, which correspond to the highest total received powers

possible with each format. The specific power levels of each symbol were optimised for each format individually to maximise the performance of the respective format after transmission as determined by its BER. The optimisation process selected for asymmetric eyes in the PAM4 B2B case and it is known that this can help to mitigate the effects of dispersion [124]. Interestingly, the optimised DB4 signal possessed much more symmetrical eyes and this is likely because its intrinsic dispersion tolerance meaning that eyes are chosen for their additive noise performance (symmetric) over dispersion performance (asymmetric).

The performance of the various signals after fibre transmission was studied and the results are presented in the following sections.

6.4.1.2 45-km SOA Transmission

The performance of the 45-km link employing the SOA as a booster amplifier was studied first. Figure 6-14 provides spectral plots of the three formats at various points of a 45-km SOA-equipped link. The SOA output power was 8.5dBm, which was adjusted to meet the optimum value of the AMI4 transmission. AMI4 and DB4 clearly show carrier suppression, which was caused by the repeated phase shift. The traces were also indicative of the nonlinear distortion of the signals induced by the SOA, which manifested as preferential amplification of the blue-side of the signal spectrum [62]. In addition, a comparison between the spectra at the amplifier output to those captured at the receiver revealed some Kerr-induced spectral broadening during transmission, which was present in all cases. For a better illustration of the spectral broadening, see the inset plots in Figure 6-14, which show the three spectra of PAM4-SOA normalised so that their peaks sit atop one another.

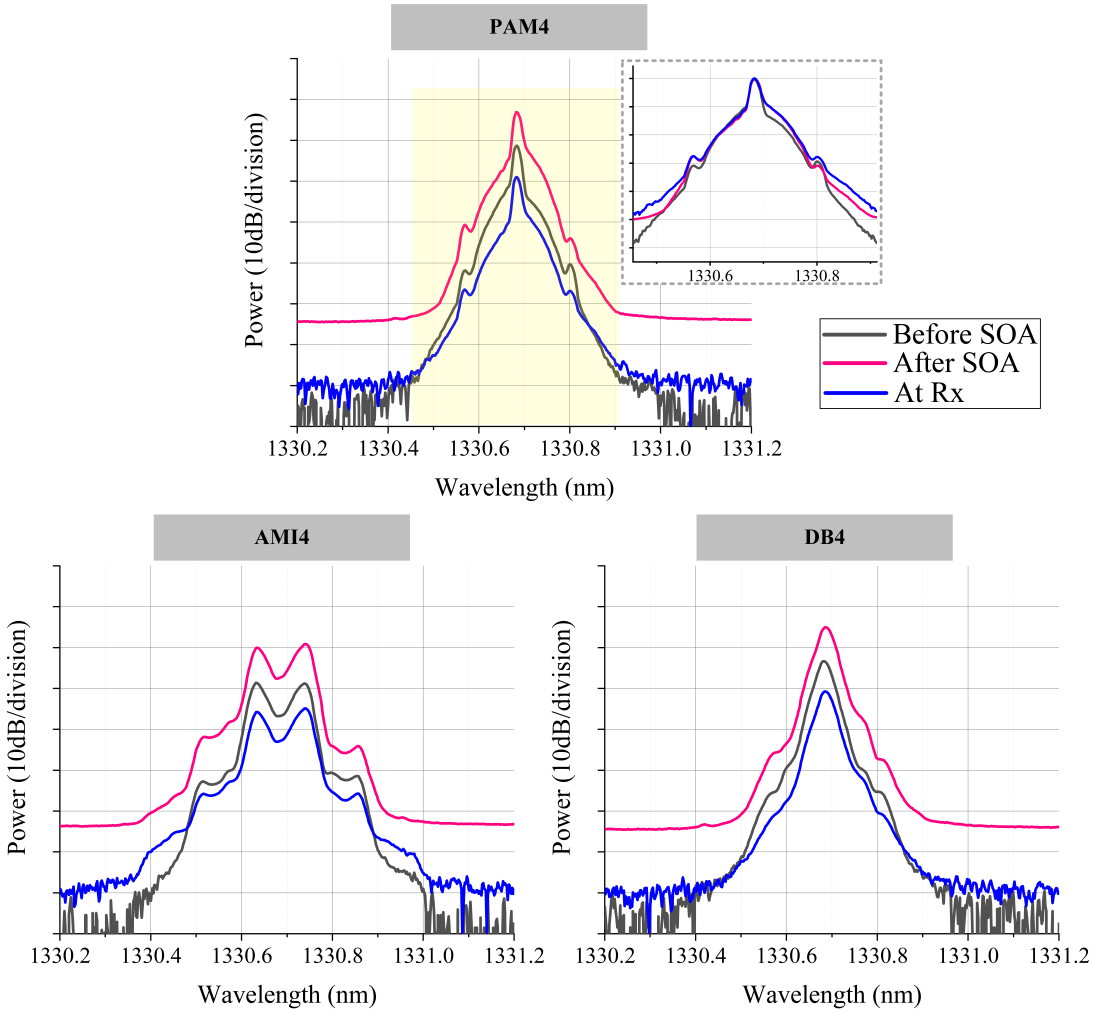

Figure 6-14: Spectra of PAM4, AMI4, and DB4 for the SOA-equipped link for the transmission reach of 45km. The optical spectrum analyser resolution was set to 0.01nm to capture the spectra. The inset plots on the top row are normalised spectra whose peaks lie atop one another (highlighted region shows the range of the spectra; y-axis plotted with 10dB/division).

The BER results are shown in Figure 6-15 (a). Evidently, out of the three formats, AMI4 was the only one that could achieve BERs almost at the FEC limit. In addition, both partial response formats, AMI4 and DB4, offered a better tolerance to the effects of nonlinearities in the transmission link than the PAM4 signal. This was evidenced by their optimum BER points which occurred at around the same launch power of ~8.5dBm, while the PAM4 case happened at ~7.4dBm. Comparing the Q-factors of PAM4 and AMI4 at their optimum points shows that AMI resulted in a 3.96-dB Q-factor improvement compared PAM4.

To observe the signal distortions, the eye diagrams of the transmitted signals were captured at the receiver (without any DSP) and are shown in Figure 6-15 (b). Note that the presented signals were taken at their optimum point, corresponding to their minimum BER (points A, B, and C, respectively) observed in Figure 6-15 (a). The results show that the eyes of both PAM4 and DB4 exhibited obvious skewing. This form of distortion is usually due to nonlinearity-induced effects [125]. In this case, these originated mainly from the SOA amplification; in the next section, it will be seen that in the BDFA-equipped links, there was less eye skewing. Meanwhile, the eye diagram of AMI4 maintained a good eye-opening, even though it was captured at a higher launch power than PAM4. This was mainly because of the nonlinearity-mitigation capability of AMI4 [115] [117]. AMI4 not only offered superior nonlinearity performance but also exhibited the benefit of an RZ-like format in terms of allowing a wider eye-opening at a given received average power (compared to the DB4's eye which was measured at around the same power).

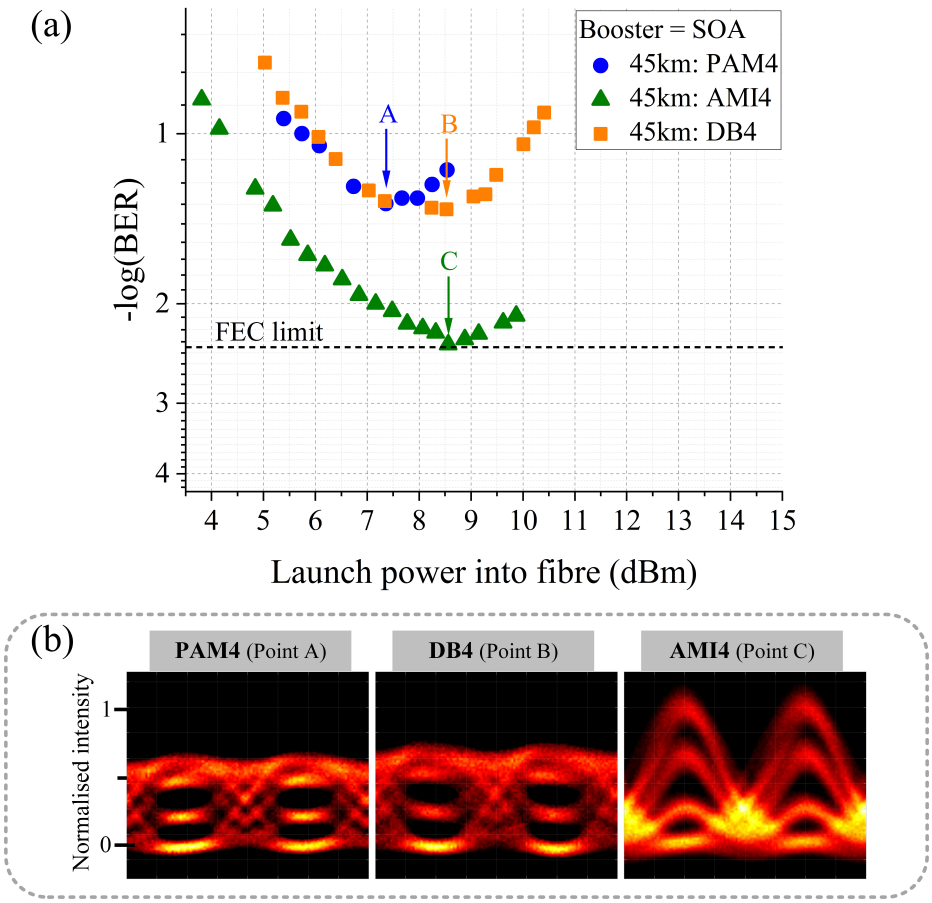

Figure 6-15: 45-km transmission with the SOA as a booster: (a) BER curves (b) eye diagrams captured at the optimum BER (points A, B, and C) of the signals.

6.4.1.3 45-km and 60-km BDFA Transmissions

In this section, we provide the results and discussions of the transmission with the BDFA. By replacing the SOA with the BDFA, we were also able to extend the transmission distance from 45km to 60km. Figure 6-16 provides spectral plots of the three formats at various points of a 45-km BDFA-equipped link (BDFA output power/launch power = 12.5dBm). It can be seen that after amplification the spectra remain more symmetrical than those of the SOA case (shown in Figure 6-14), while propagation along the fibre still caused Kerr-induced spectral broadening. Spectra for the 60-km case have been omitted as they are very similar to the 45-km case.

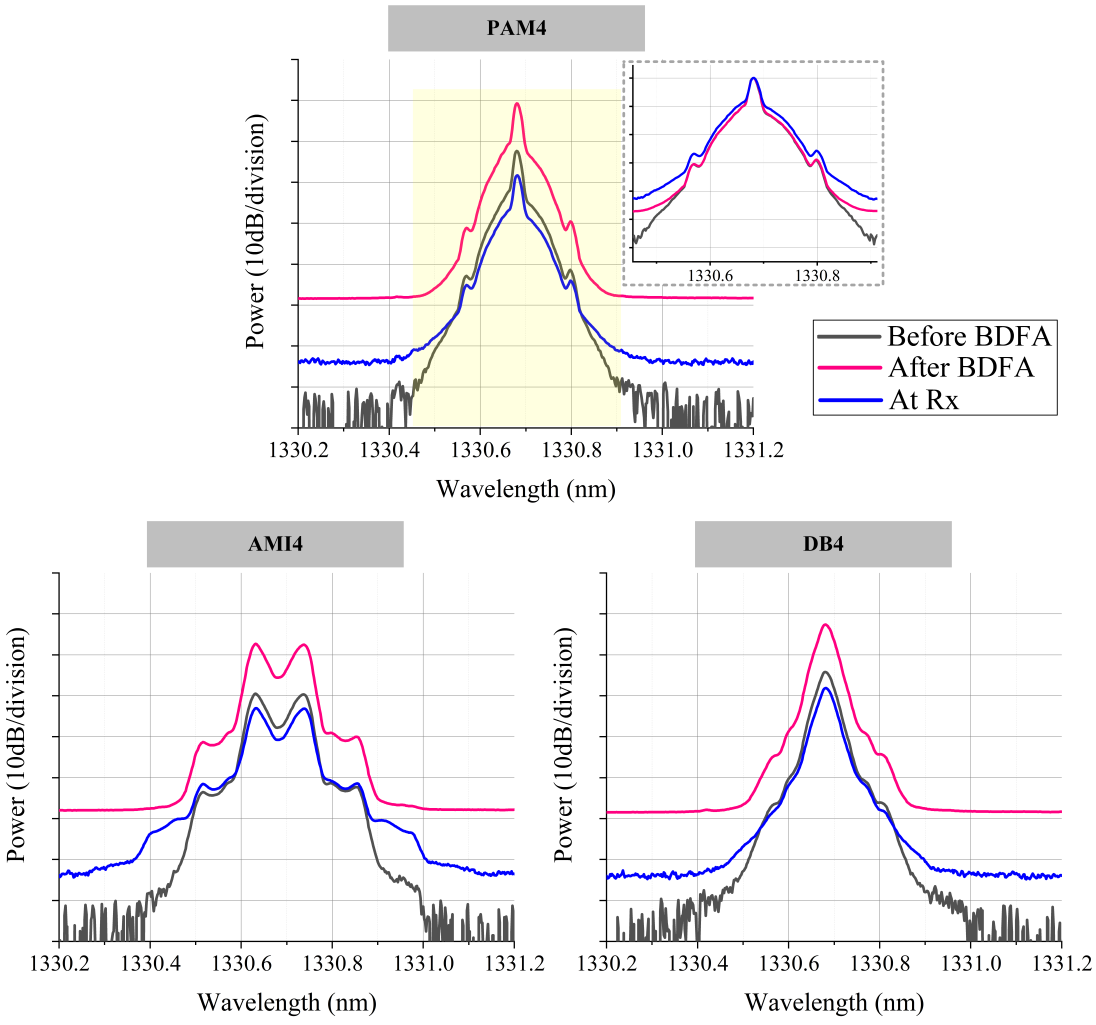

Figure 6-16: Spectra of PAM4, AMI4, and DB4 for the BDFA-equipped link for the transmission reach of 45km. The OSA resolution was set to 0.01nm for the measurement. The inset plots on the top row are normalised spectra whose peaks lie atop one another (highlighted region shows the range of the spectra; y axis plotted with 10dB/division)

The BER curves for the 45-km distance and the 60km case are presented in Figure 6-17 (a) and Figure 6-17 (b), respectively. In the 45km case, all three formats could realise BERs below the FEC limit. As before, the performance of the AMI4 signal was far better than that of the others. Its improvement was equivalent to 2.72dB in Q-factor compared to the PAM4 signal and indicated that AMI4 can be launched at a higher power than in the SOA case. After the extension of the link, PAM4 and DB4 failed to reach the FEC limit, whilst AMI4 still succeeded, offering a 4.28dB improvement in Q-factor over the PAM4 signal. Once again, AMI4 showed superior tolerance to nonlinearities, allowing higher powers to be launched into the fibre.

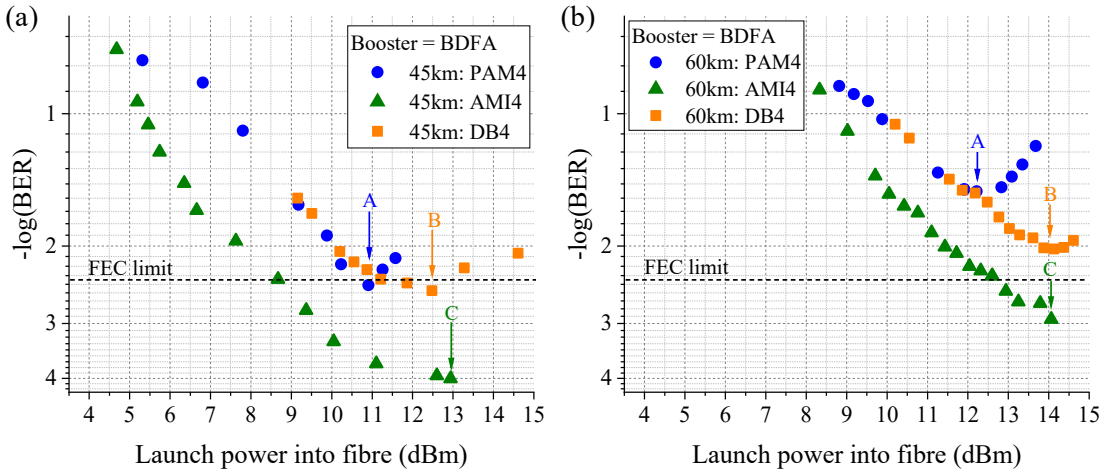

Figure 6-17: BER curves of BDFA-equipped transmissions at (a) 45km and (b) 60km.

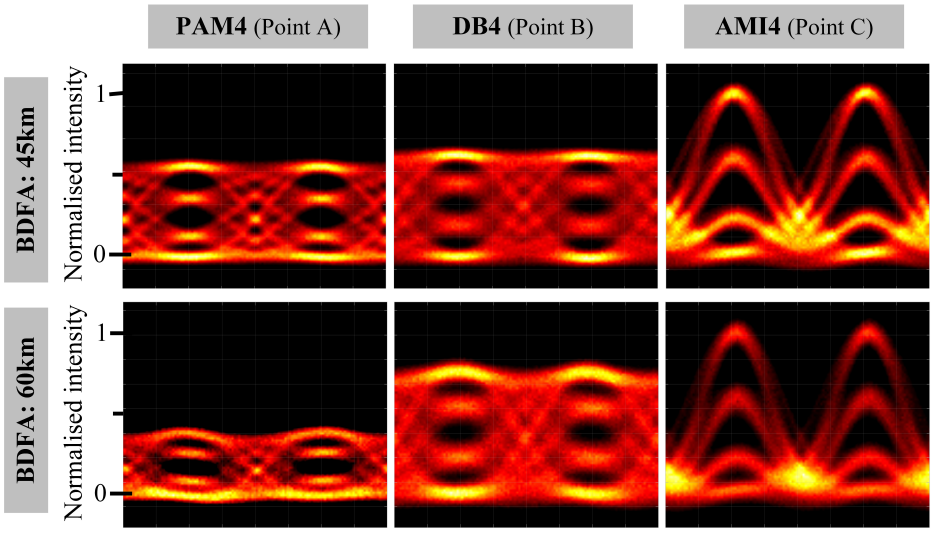

Figure 6-18: Eye diagrams of BDFA-equipped transmissions of 45km (top row) and 60km (bottom row) captured at the optimum BER (points A, B, and C) of the signals.

The eye diagrams after transmission, captured at the optimum points for each signal (points A, B, and C), with BDFA amplification for 45km and 60km are shown in the top and bottom rows, respectively, of Figure 6-18. Evidently, the top power level distortion on PAM4 and DB4 signals, due to the nonlinearity that we can observe in the SOA case, disappeared in the BDFA-equipped link. Despite the apparent absence of nonlinear distortion, the eyes were still distorted at the bottom level due to dispersion and eye opening decreased. This effect was less severe in the DB4 and AMI4 signals since ISI in the optical domain induced destructive interference between the π-phase shifted adjacent symbols and so helped to maintain the contrast between symbols. Once the reach was extended from 45km to 60km, the transmission became even more affected by dispersion. In this case, the benefit of adopting phase flip was even more evident, since a typical IMDD format like PAM4 was rendered irrecoverable much sooner than the other formats, having very narrow bottom eyes even at its optimum launch power, whilst DB4 and AMI4 maintained their eye-opening after transmission.

6.4.2 Simulation Study

In the previous section, we experimentally demonstrated the benefit of employing AMI4 in O-band transmission. We chose to compare AMI4 to NRZ-PAM4 because the equipment requirements were very similar. In that scenario, we could not directly determine whether the benefit of AMI4 was due to the serial phase flip or the specific RZ-like pulse shape of AMI4. In order to illustrate the mechanism by which AMI4 improved tolerance to nonlinearity, a simulation matched to the experimental conditions was performed using *VPI Photonics*. The peak launch power of all signals was fixed at 60mW and the symbol rate was set to 50GBd (these variables were chosen to make the phenomena more visually noticeable). The waveforms before and after transmission are presented in Figure 6-19, where a continuous wave (CW) laser and a pulsed (PS) laser were used as the source in Figure 6-19 (a-b) and Figure 6-19 (c-d), respectively.

The PAM4 and AMI4 formats studied experimentally in the previous sections correspond to the CW-PAM4 (Figure 6-19 (a)) and CW-AMI4 (Figure 6-19 (b)) simulation results. Here it is clear that CW-AMI4 is able to maintain differentiation between the four power levels of the signal, whilst regular CW-PAM4 is not, as

expected. Narrowing of the CW-AMI4 pulses can also be seen and this is due to the destructive interference between consecutive pulses.

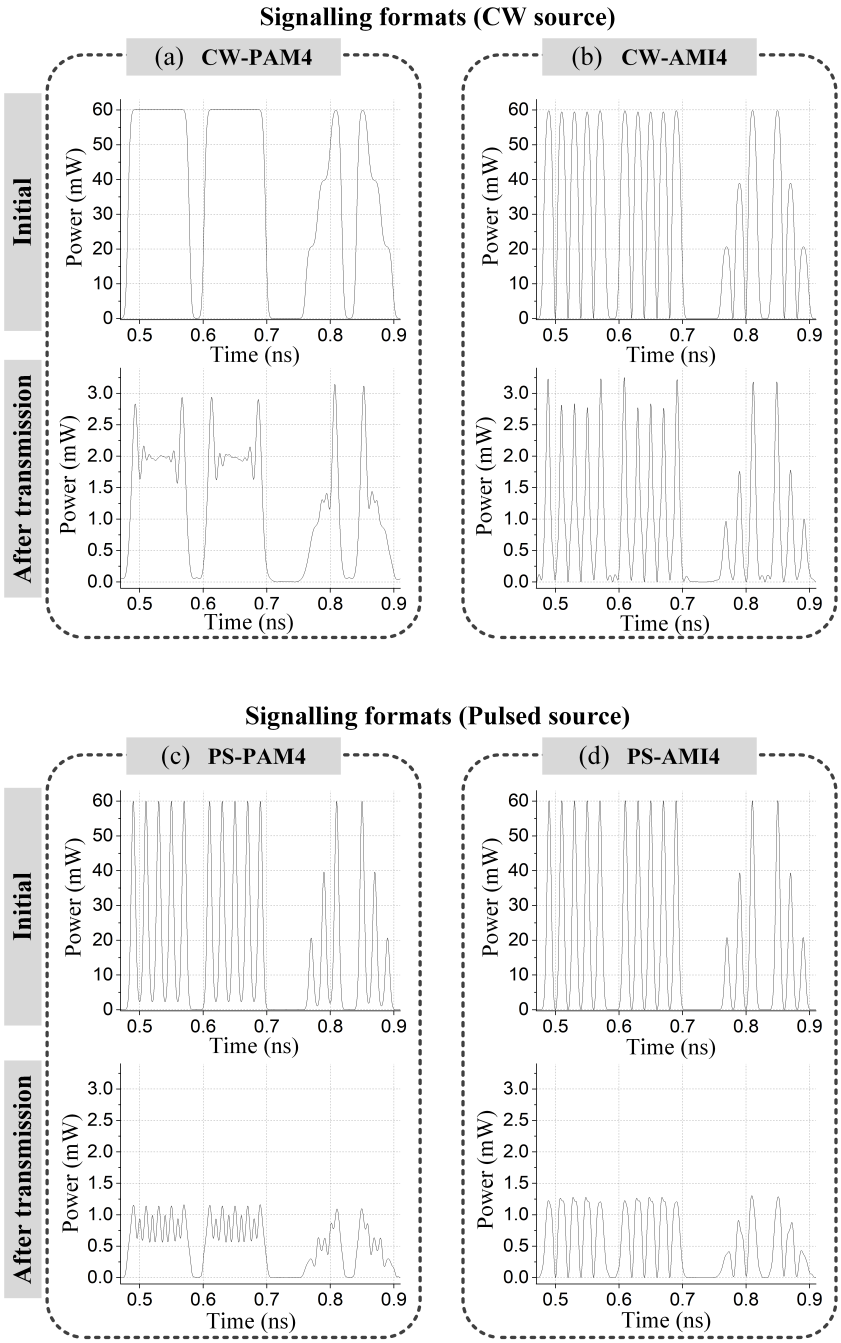

Figure 6-19: Simulation results of a 45-km transmission of SMF-28e at $\lambda = 1330.7$ nm with (a) CW-PAM4, (b) CW-AMI4, (c) PS-PAM4, and (d) PS-AMI4 at the transmitter (initial) and after the transmission. The transmission parameters are – bit pattern = '333330333300012303210', symbol rate = 50 GBd, attenuation = 0.33 dB/km, and dispersion = 1.0 ps/nm/km.

The first question to answer is whether RZ signalling alone provides nonlinearity tolerance. Indeed, it can be seen that, although PS-PAM4 (Figure 6-19 (c)) did suffer from nonlinear distortion, it did not suffer as much as CW-PAM4 (Figure 6-19 (a)). This shows that RZ signalling can be beneficial to nonlinear performance and to understand why, it can be useful to consider the impact that SPM can have on a pulse. Recalling that the phase shift experienced by a signal due to SPM can be described by: $\Delta\phi \propto P$, it follows that $\frac{d\Delta\phi}{dt} \propto \frac{dP}{dt}$. Thus, on its own, the constant power region of the pulse remains relatively unchanged by SPM (where $\frac{dP}{dt}$ and therefore $\frac{d\phi}{dt}$ are low), whilst the edges of the pulse (where $\frac{dP}{dt}$ and therefore $\frac{d\phi}{dt}$ are high) will generate the 'cat-ears' discussed in Section 2.1.4, which will subsequently be pulled away from the pulse by dispersion, forming ghost pulses that will interfere with neighbouring pulses. RZ signalling regularises pulse lengths, resulting in all pulses being distorted in the same, potentially tolerable, way. This accounts for the improvement in performance of PS-PAM4 over CW-PAM4 (and also of AMI4 relative to DB4), but it does not explain what happens when these ghost pulses interfere with neighbouring symbols.

To understand this, we can compare the results of PS-PAM4 (Figure 6-19 (c)) to PS-AMI4 (Figure 6-19 (d)). Here, it can be seen that PS-AMI4 provided a much clearer 4-level pattern at the receiver than PS-PAM4 and, given their identical original pulse shape, it shows that the *phase flip* itself was indeed beneficial for transmission. This is simply due to the destructive interference between colliding ghost pulses in PS-AMI4 (and AMI signalling in general), but their constructive interference in PAM4. Indeed, when viewing the results of the PS-PAM4 simulation after transmission, individual ghost pulses can be discerned lying between the original pulses.

Finally, comparing CW-AMI4 (Figure 6-19 (b)) to PS-AMI4 (Figure 6-19 (d)), we can see that, although the former offers a larger eye opening, the latter has more regularly spaced eyes. It is clear that *pulse shape* does in general have an impact on the performance of transmission formats and for CW-AMI4, this pulse will be determined by a combination of the pulse shape of the electrical drive waveform and the MZM transfer curve, as is typical.

In summary, it was both the phase flip and the MZM-induced pulse shape which were responsible for AMI4's benefits.

6.5 Conclusion

The implementation of high-capacity transmission systems in the O-band may expose signals to greater nonlinear distortion compared to the C-band, owing to the lower dispersion, higher loss (resulting in higher launch powers) and higher nonlinearity of the O-band. In this chapter, AMI was demonstrated to provide a substantial improvement over OOK and DB in the O-band, owing partly to its tolerance to nonlinearity, but also its RZ-like nature (proven by simulation). AMI did not lose this advantage when it was extended to AMI4 and indeed it was shown that a transmission of AMI4 over 60km of fibre could still reach the FEC limit, whereas PAM4 and DB4 could not. The simulation results confirm that the benefits of AMI4 over regular PAM4 signalling arise from both the repeated phase flipping and the RZ-like nature of the format. Generation of AMI with an MZM provides a convenient way of generating an RZ format without the need for higher bandwidth electrical drive signals or additional pulse carving modulators.

Overall, we observed that the combination of a low-nonlinearity doped-fibre amplifier and AMI4 offered a great improvement in receiver sensitivity, thanks to a greater tolerance to nonlinear impairments, especially in the low CD region of the O-band.

Now that it has been proven that the concepts of AMI and DB can be applied to PAM4, it is natural to speculate what impact they can have on even higher order formats, such as PAM8 and beyond. Such formats are less tolerant to additive noise, dispersion and nonlinearity, and so adopting partial response formats that enhance their performance could be especially valuable.

In this work, an external modulator (a DD-MZM) was used to generate the formats under test. However, it is common in cost-sensitive O-band systems to use directly modulated lasers (DMLs). Adopting an approach similar to the technique published in [126], where a DML was used to create a quadrature phase-shift keying (QPSK) signal through the generation of a signal in the upper-right quadrature of a phase diagram, followed by coherent addition, could help to bring the cost advantages of direct modulation to AMI and DB.

Chapter 7

Conclusions

This thesis investigated the idea that the BDFA could be the O-band equivalent to the C-band EDFA – a low noise, high gain, linear optical amplifier which could bring about adoption of amplified DWDM O-band systems. To make this case, the BDFA was thoroughly characterised, being compared to both C-band EDFAs and alternative O-band amplifiers, before being applied to a number of realistic transmission experiments. These experiments increase the confidence that the BDFA is suitable for deployment in real-world systems and will guide the development of any future transmission systems equipped with the BDFA.

It is worthwhile reviewing some of the key points discovered during this work. The BDFA studied had a 5-dB gain bandwidth of 50nm (roughly between 1320nm and 1370nm) and a peak gain of more than 25dB at an input power of -20dBm. This bandwidth is equivalent to ~8.3THz in frequency and compares favourably to the ~4.4-THz bandwidth of a typical C-band EDFA. Regarding the gain tilt characterisation, it was demonstrated that the BDFA had a dynamic gain tilt of between -0.3dB/nm and 0.4dB/nm (0-dBm input power) over the wavelength range 1320nm to 1360nm (longer wavelengths could not be measured due to laser availability), which compares well to the EDFAs dynamic gain tilt of 0.6dB/nm at a wavelength of 1545nm and 0.2dB/nm at a wavelength of 1559nm for the same input

power, as reported in [86]. Gain flatness is especially important in long-haul WDM systems, where it can lead to unequal gain between channels and limit band performance.

Dynamic performance is another important property for WDM systems that is determined by the carrier lifetime of the amplifier. Arguably, the most popular current solution for O-band amplification is the SOA, but unfortunately, SOAs exhibit a relatively short carrier lifetime (less than 1ns), giving rise to a dynamic gain response and causing a number of nonlinear phenomena which can impair their performance severely. Doped fibre amplifiers, on the other hand (and especially the EDFA) are known for their much longer carrier lifetime (~10ms). Problems arising from a short carrier lifetime can manifest in a relatively fast gain recovery in response to transient changes in input power that can cause patterning effects on the signal or XGM. The transient response was measured for both the BDFA and the SOA. It was shown that the BDFA had a considerably slower response. Specifically, the transient response of the BDFA dropped below 0.5dB for a modulation speed of 150kHz (compared to ~6kHz in the EDFA, reported by [88]), whilst for the SOA, the transient response remained ~7dB, with no signs of dropping with increasing frequency. Although, the carrier lifetime of the BDFA (~600μs) is not quite as low as that of the EDFA, there were no observable adverse effects when operating the BDFA in deep saturation. Moreover, the PDG of the BDFA was confirmed to be typical for a doped fibre amplifier, at <0.64dB for all scenarios studied. This is another metric where SOAs tend to perform poorly.

The parameter investigated next was the NF, which has a substantial impact upon amplifier performance. The frequency-resolved NF of several amplifiers was measured to ensure that the amplifiers did not exhibit any unexpected low-frequency noise which could compromise their performance. The results confirmed that the BDFA exhibited no excessive low-frequency noise and had a NF between 6dB and 7dB, comparable to a typical 'booster' EDFA that was also measured (although it should be noted that the BDFA had a saturated output power of 16dBm, which was lower than typical booster EDFAs, >20dBm). This NF is expected to improve as BDFA technology develops further, and it is noted that there is a complex chemistry that must be understood to extract gain from the broad fluorescence bandwidth of bismuth. Afterwards, the frequency-resolved NF method was also applied to a number of other optical amplifiers – the SOA, a double-pass BDFA, a broadband Raman amplifier. At

the power level investigated, the SOA exhibited no excess low-frequency noise, but did possess a NF that was generally worse than that of the BDFA. Meanwhile, both the double-pass BDFA and the Raman amplifier showed an excess of low-frequency noise, supporting the importance of performing a frequency-resolved NF measurement on novel amplifiers.

With the positive results provided by the gain and NF characterisations, the next stage was to study the BDFA in a realistic transmission system. Its performance was first demonstrated in several WDM experiments using ~10Gbit/s OOK signals over a wavelength range of 1321nm to 1371nm. This format and bitrate were chosen as they are arguably the most well studied and, hence, would produce intuitive results, widely comparable to telecommunications literature. A satisfactory performance after transmission was shown both in a wideband CWDM scenario as well as a narrowband DWDM scenario, the latter undertaken to provide results with realistic channel spacings of 100GHz and 200GHz. A maximum reach of 140km was achieved, which could be extended further with additional BDFAs as the error performance at the receiver was power limited, rather than OSNR limited. Moreover, the nonlinear performance of the BDFA, when being used as an inline amplifier, was found to be considerably better than that of the SOA and indeed the transmission fibre was observed to create more FWM than the BDFA itself. These experiments gave the confidence to embark on a series of transmission experiments in collaboration with Dr Yang Hong, in which the reach extension of O-band signals was demonstrated for a variety of signals (see the List of Publications for the related references).

The observation of nonlinearity during transmission suggested that it might be beneficial to study techniques for nonlinearity mitigation, especially since, given the higher loss of the O-band (encouraging higher launch power), as well as the lower CD (in SSMF), it is expected that performance in O-band systems may become limited by nonlinearity sooner than in the C-band. AMI is a well-known technique for nonlinearity tolerance and it has been extensively studied in the C-band, where it became understood that its benefits arose due to the mitigation of degradation caused by the mixture of dispersive and nonlinear effects, causing ghost pulses, rather than nonlinearity alone [117]. Therefore, it might be expected that AMI would not offer improvements to nonlinearity tolerance in the near-zero dispersion O-band region. Interestingly, it was demonstrated in this thesis that AMI was very effective for compensating nonlinearity experienced by O-band signals from both an SOA and from

the SSMF transmission fibre itself. Adoption of AMI in a link equipped with an SOA booster enabled a reach in excess of 60km to be achieved, where both regular NRZ-OOK and DB failed. The concept of AMI was extended to a higher-order signalling with the development of the AMI4 format. This was the first time this format was demonstrated and it also provided a notable performance improvement, with the adoption of AMI4 allowing reach extension of 33% relative to that achievable with PAM4 or DB4. The simulation results also confirmed that the benefits of AMI over regular IMDD formats were due to both phase alternating and the RZ-like nature of the AMI.

For convenience, Table 7-1 summarises the key performance metrics of the BDFA presented in this work. In summary, the results presented in this thesis support the use of the BDFA as a practical O-band amplifier. Indeed, it could be argued that the BDFA is currently the most suitable source of O-band amplification available at this time (in terms of noise performance, bandwidth, and simplicity), although this is something that will be determined as the BDFA is refined further and early attempts are made at its commercialisation.

Key Performance Metrics of the BDFA	**Value**
BDF length	150 m
Intrinsic loss of the BDF (measured at 1550 nm)	14.6 dB
BDF-to-SSMF splicing loss (measured at 1550 nm)	0.3 dB
Bi-directional pumping wavelengths	1240 nm and 1267 nm
Total pump power	720 mW
Confirmed useable wavelength range (5-dB bandwidth)	1320 nm – 1370 nm
Confirmed useable bandwidth (5-dB bandwidth)	8.3 THz
Peak gain (around 1340nm)	>25 dB
Saturated output power	16 dBm
Wavelength at zero-crossing static gain tilt (0 dB/nm)	1340 nm
Dynamic gain tilt between 1320nm and 1360nm	<0.4 dB/nm
Transient response at beyond 150-kHz modulation speed	<0.5 dB
Maximum XGM (tested with 100GHz and 200GHz spacings)	-20dB
PDG	<0.64 dB
Averaged NF (using electrical method)	6 dB – 7 dB

Table 7-1: Key performance metrics of the BDFA.

7.1 Future Work

The experimental work presented in this thesis has highlighted both the promising performance of the BDFA and its practicality in WDM O-band transmission has been demonstrated. This section presents future work that could be undertaken for further development of the performance of the BDFA as well as for broadband optical telecommunications in the O-band and beyond.

7.1.1 BDFA Performance

Regarding the amplifier characterisation presented in Chapter 3 and Chapter 4, there are further measurements that could be taken to expand the characterisation of the BDFA further still. For example, the presence (or absence) of spectral hole burning in the BDFA could be confirmed. Spectral hole burning occurs when an amplifier is not fully homogenously broadened and can essentially cause localised depletion of gain. Polarisation hole burning is a similar phenomenon that could also be characterised and might be particularly interesting here as the BDFA tested has a much longer gain fibre (150m) than typical EDFAs have (on the order of metres) and polarisation hole burning is known to depend upon PMD [127].

Although bismuth-doped fibres exhibit a broad fluorescence band, implementation of practical gain fibres has been a challenge because the luminescence of a given sample depends strongly on the state of the bismuth active centres contained within the fibre. This state itself is determined by the presence of oxygen deficient centres that cause a change in the valence state of bismuth ions [76] [80]. In may be worthwhile conducting longer term studies to ensure the stability of the glass and/or bismuth active centres, although it is noted the same amplifier was used in this thesis over a 3-year period with no discernible change in amplifier performance.

A further study on the bismuth doped fibre is to investigate its transparency to C-band light. This study might be useful in O+C band transmission. If the BDFA is transparent to the C-band signal, the system will not need to split the two bands at the amplification stage and hence could offer a lower cost and loss.

The next major step for the BDFA would be to seek a possible commercialisation of the amplifier. Important activities supporting this would be to develop additional pumping control modes, such as automatic current control (ACC), automatic power control (APC), and automatic gain control (AGC), in the boxed BDFA. This

functionality can be simply implemented by monitoring the control parameter (current, gain, or power) and applying feedback loop to maintain/correct the required parameter.

7.1.2 High-Speed, Broadband Optical Telecommunications

The lower CD and higher nonlinear coefficient in the O-band compared to the C-band, means that the O-band is likely to suffer more from nonlinearity. It will be worthwhile to fully understand the impact of nonlinearity on a highly populated DWDM band and study the application of nonlinearity compensation techniques, such as digital backpropagation or optical phase conjugation to O-band systems.

In Chapter 6, AMI was proven to increase signal tolerance to nonlinear distortion in O-band transmission. To improve the spectral efficiency (SE) of the transmission, the classic 2-level AMI format was extended to a 4-level format, which was shown to retain the benefits of nonlinearity tolerance. To increase the SE further, higher order extensions, such as AMI8 or AMI16 could be considered, although it is noted that these formats will suffer from a decreasing receiver sensitivity with increasing order. Regarding the generation of AMI, in this thesis a DD-MZM was used, which could be considered costly compared to, for instance, a DML. A DML on its own cannot, in general, be used to generate symbols of equal power but with a π relative phase shift. However, it was shown in [126] that QPSK could be generated using two DMLs and coherent addition. A similar technique could be used to generate AMI signals, with a potentially significant cost saving.

Another route to increase the SE and reach in the O-band would be the adoption of coherent formats, such as dual-polarisation QPSK or 16QAM. Coherent communication might be particularly useful in the O-band, given its higher loss than the C-band. Adoption of coherent communication would also enable the use of digital back propagation, as discussed previously.

The specific BDFA tested here (with phosphosilicate glass host) provides coverage over the 1320nm-1370nm wavelength region. However, the very same fibre, when pumped at longer wavelengths (1270nm and 1310nm) can exhibit gain across the E-band [18]. Beyond this, as mentioned before, bismuth doped fibres can offer gain over much of the transmission window of SSMF. Regarding ultra-wide-band communication, demonstrating gain over as much of the transmission window of

SSMF as possible using a variety of BDFAs as well as other doped fibre amplifiers, will be useful for understanding which bands are the most promising for future communications. Such studies could be extended to hollow core fibre, notably nested anti-resonant nodeless fibre (NANF) which have been demonstrated to offer the possibility of very wide and flat transmission windows. Such fibres have been demonstrated with transmission windows from ~1000nm to ~2000nm [128] [129] (corresponding to a bandwidth of 150THz), with a loss as low as 0.28dB/km [130] and offer 67% of the latency of SSMF. With further development, such fibres may bring the loss in the O-band down the same level as that in the C-band in SSMF. Along with the very low nonlinearity and low CD that can be offered by NANF [131], it could bring O-band performance in line with C-band performance, making DWDM in the O-band even more possible.

List of Publications

Publications as First Author

1. **N. Taengnoi**, K.R.H. Bottrill, Y. Hong, Y. Wang, N.K. Thipparapu, J.K. Sahu, P. Petropoulos, and D.J. Richardson, "Experimental Characterization of Bismuth-Doped Fibre Amplifier: Electrical NF, PDG, and XGM," in *2020 Conference on Lasers and Electro-Optics (CLEO)*, 2020.

2. ***N. Taengnoi**, K.R.H. Bottrill, Y. Hong, Y. Wang, N.K. Thipparapu, J.K. Sahu, P. Petropoulos, and D.J. Richardson, "Experimental characterization of an O-band bismuth-doped fiber amplifier," *Optics Express,* vol. 29, no. 10, pp. 15345-15355, 2021.
   Dataset DOI: 10.5258/SOTON/D1780

3. **N. Taengnoi**, K.R.H. Bottrill, N.K. Thipparapu, A.A. Umnikov, J.K. Sahu, P. Petropoulos, and D.J. Richardson, "Amplified O-Band WDM Transmission Using a Bi-Doped Fibre Amplifier," in *2018 European Conference on Optical Communication (ECOC)*, Rome, Italy, 2018.
   Dataset DOI: 10.5258/SOTON/D0422

4. *__N. Taengnoi__, K.R.H. Bottrill, N.K. Thipparapu, A.A. Umnikov, J.K. Sahu, P. Petropoulos, and D.J. Richardson, "WDM Transmission with In-Line Amplification at 1.3μm Using a Bi-Doped Fiber Amplifier," *Journal of Lightwave Technology,* vol. 37, no. 8, pp. 1826-1830, 2019.

   Dataset DOI: 10.5258/SOTON/D0796

5. **N. Taengnoi**, K.R.H. Bottrill, C. Lacava, D.J. Richardson, and P. Petropoulos, "AMI for Nonlinearity Mitigation in O-Band Transmission," in *2019 Optical Fiber Communications Conference and Exhibition (OFC)*, San Diego, CA, 2019.

   Dataset DOI: 10.5258/SOTON/D0677

6. **N. Taengnoi**, K.R.H. Bottrill, Y. Hong, N.K. Thipparapu, C. Lacava, J.K. Sahu, D.J. Richardson, and P. Petropoulos, "Reach extension of PAM4 signals in O-band transmission by application of alternate-mark-inversion," in *2019 European Conference on Optical Communication (ECOC)*, Dublin, Ireland, 2019.

   Dataset DOI: 10.5281/zenodo/2648810

7. *__N. Taengnoi__, K.R.H. Bottrill, Y. Hong, N.K. Thipparapu, C. Lacava, J.K. Sahu, D.J. Richardson, and P. Petropoulos, "4-Level Alternate-Mark-Inversion for Reach Extension in the O-Band Spectral Region," *Journal of Lightwave Technology,* vol. 39, no. 9, pp. 2847-2853, 2021.

   Dataset DOI: 10.5258/SOTON/D1753

* Journal publications.

Other Publications

1. K.R.H. Bottrill, **N. Taengnoi**, Y. Hong, D.J. Richardson, and P. Petropoulos, "Self-Pumping Saturated Four Wave Mixing Through Harmonic Synthesis," in *2019 European Conference on Optical Communication (ECOC)*, Dublin, Ireland, 2019.

2. *K.R.H. Bottrill, **N. Taengnoi**, F. Parmigiani, D.J. Richardson, and P. Petropoulos, "PAM4 transmission over 360 km of fibre using optical phase conjugation," *OSA Continuum,* vol. 2, no. 3, pp. 973-982, 2019.

3. Y. Hong, **N. Taengnoi**, K.R.H. Bottrill, H. Sakr, T. Bradley, J. Hayes, G. Jasion, Y. Wang, N.K. Thipparapu, A.A. Umnikov, J.K. Sahu, F. Poletti, P. Petropoulos, and D.J. Richardson, "Dual O+C-band WDM transmission over 1-km hollow core NANF using an O-band bismuth-doped fibre amplifier," in *2019 European Conference on Optical Communication (ECOC)*, Dublin, Ireland, 2019.

4. Y. Hong, K.R.H. Bottrill, **N. Taengnoi**, H. Sakr, T. Bradley, J. Hayes, G. Jasion, F. Poletti, D.J. Richardson, and P. Petropoulos, "Beyond 100-Gb/s/λ direct-detection transmission over the S+C+L-bands in an ultra-wide bandwidth hollow core fibre," in *2019 European Conference on Optical Communication (ECOC)*, Dublin, Ireland, 2019.

5. H. Sakr, K.R.H. Bottrill, **N. Taengnoi**, P. Petropoulos, D.J. Richardson, F. Poletti, Y. Hong, T. Bradley, G. Jasion, J. Hayes, H. Kim, I.A. Davidson, E.N. Fokoua, and Y. Chen, "Hollow Core Optical Fibres for Ultra-Wideband Optical Communications," in *2019 Asia Communications and Photonics Conference (ACP)*, Chengdu, China, 2019.

6. P. Petropoulos, J. Hayes, G. Jasion, J.K. Sahu, F. Poletti, D.J. Richardson, Y. Hong, K.R.H. Bottrill, **N. Taengnoi**, H. Sakr, T. Bradley, N.K. Thipparapu, Y. Wang, and A.A. Umnikov, "Extending the Optical Bandwidth of Optical Communication Systems," in *2019 Asia Communications and Photonics Conference (ACP)*, Chengdu, China, 2019.

7. H. Sakr, T. Bradley, Y. Hong, G.T. Jasion, J. Hayes, H. Kim, I.A. Davidson, E.N. Fokoua, Y. Chen, K. Bottrill, **N. Taengnoi**, P. Petropoulos, D.J. Richardson, and F. Poletti, "Ultrawide Bandwidth Hollow Core Fiber for Interband Short Reach Data Transmission," in *2019 Optical Fiber Communications Conference and Exhibition (OFC)*, San Diego, CA, 2019.

8. *K.R.H. Bottrill, **N. Taengnoi**, Y. Hong, D.J. Richardson, and P. Petropoulos, "Phase Preserving Amplitude Saturation Through Tone Synthesis Assisted Saturated Four-Wave Mixing," *Journal of Lightwave Technology,* vol. 38, no. 7, pp. 1817-1826, 2020.

9. *H. Sakr, K.R.H. Bottrill, **N. Taengnoi**, N.V. Wheeler, P. Petropoulos, D.J. Richardson, F. Poletti, Y. Hong, T. Bradley, G.T. Jasion, J. Hayes, H. Kim, I. Davidson, E.N. Fokoua, and Y. Chen, "Interband Short Reach Data Transmission in Ultrawide Bandwidth Hollow Core Fiber," *Journal of Lightwave Technology,* vol. 38, no. 1, pp. 159-165, 2020.

10. *Y. Hong, K.R.H. Bottrill, **N. Taengnoi**, N.K. Thipparapu, Y. Wang, A.A. Umnikov, J.K. Sahu, D.J. Richardson, and P. Petropoulos, "Experimental Demonstration of Dual O+C-Band WDM Transmission Over 50-km SSMF With Direct Detection," *Journal of Lightwave Technology ,* vol. 38, no. 8, pp. 2278-2284, 2020.

11. *Y. Hong, H. Sakr, **N. Taengnoi**, K.R.H. Bottrill, T. Bradley, J. Hayes, G. Jasion, H. Kim, N.K. Thipparapu, Y. Wang, A.A. Umnikov, J.K. Sahu, F. Poletti, P. Petropoulos, and D.J. Richardson, "Multi-Band Direct-Detection Transmission Over an Ultrawide Bandwidth Hollow-Core NANF," *Journal of Lightwave Technology ,* vol. 38, no. 10, pp. 2849-2857, 2020.

12. Y. Hong, T. Bradley, **N. Taengnoi**, K.R.H. Bottrill, J. Hayes, G. Jasion, H.C. Mulvad, F. Poletti, P. Petropoulos, and D.J. Richardson, "Comparative Investigations between SSMF and Hollow-Core NANF for Transmission in the S+C+L-Bands," in *2020 Optical Fiber Communications Conference and Exhibition (OFC)*, San Diego, CA, 2020.

13. Y. Hong, K.R.H. Bottrill, **N. Taengnoi**, N.K. Thipparapu, Y. Wang, J.K. Sahu, D.J. Richardson, and P. Petropoulos, "First Investigation on Double- and Single-Sideband Formats in BDFA-Enabled O-Band Transmission," in *2020 Conference on Lasers and Electro-Optics (CLEO)*, 2020.

14. Y. Hong, F. Feng, K.R.H. Bottrill, **N. Taengnoi**, R. Singh, G. Faulkner, D. O'Brien, and P. Petropoulos, "Beyond Terabit/s WDM Optical Wireless Transmission using Wavelength-Transparent Beam Tracking and Steering," in *2020 Optical Fiber Communications Conference and Exhibition (OFC)*, San Diego, CA, 2020.

15. S. Liang, S. Jain, L. Xu, K.R.H. Bottrill, **N. Taengnoi**, M. Guasoni, P. Zhang, M. Xiao, Q. Kang, Y. Jung, P. Petropoulos, and D.J. Richardson, "Record Gain, Low Noise Figure, C+L Band Lumped Raman Amplifier," in *2020 European Conference on Optical Communications (ECOC)*, 2020.

16. Y. Hong, **N. Taengnoi**, K.R.H. Bottrill, N.K. Thipparapu, Y. Wang, J.K. Sahu, D.J. Richardson, and P. Petropoulos, "Experimental Demonstration of 50-Gb/s/λ O-band CWDM Direct-Detection Transmission over 100-km SMF," in *2021 Asia Communications and Photonics Conference (ACP)*, Shanghai, China, 2021.

17. *Y. Hong, K.R.H. Bottrill, **N. Taengnoi**, N.K. Thipparapu, Y. Wang, J.K. Sahu, D.J. Richardson, and P. Petropoulos, "Numerical and experimental study on the impact of chromatic dispersion on O-band direct-detection transmission," *Applied Optics,* vol. 60, no. 15, pp. 4383-4390, 2021.

18. *Y. Hong, T.D. Bradley, **N. Taengnoi**, K.R.H. Bottrill, J.R. Hayes, G.T. Jasion, F. Poletti, P. Petropoulos, and D.J. Richardson, "Hollow-core NANF for High-speed Short-reach Transmission in the S+C+L-bands," *Journal of Lightwave Technology,* 2021 (Early Access).

19. *S. Liang, S. Jain, L. Xu, K.R.H. Bottrill, **N. Taengnoi**, M. Guasoni, P. Zhang, M. Xiao, Q. Kang, Y. Jung, P. Petropoulos, and D.J. Richardson, "High Gain Low Noise Spectral-Gain-Controlled Broadband Lumped Fiber Raman Amplifier", *Journal of Lightwave Technology*, vol. 39, no. 5, pp. 1458-1463, 2021.

* Journal publications.

Bibliography

[1] G.P. Agrawal, "Optical Communication: Its History and Recent Progress," in *Optics in Our Time*, Springer, Cham, 2016, pp. 177-199.

[2] P.J. Winzer, D.T. Neilson, and A.R. Chraplyvy, "Fiber-optic transmission and networking: the previous 20 and the next 20 years [Invited]," *Optics Express,* vol. 26, no. 18, pp. 24190-24239, 2018.

[3] T. Miya, Y. Terunuma, T. Hosaka, and T. Miyoshita, "Ultimate low-loss single-mode fibre at 1.55 μm," *Electronics Letters,* vol. 15, pp. 106-108, 1979.

[4] International Telecommunication Union (ITU), "G.652 : Characteristics of a single-mode optical fibre and cable (11/2016)," 2016. [Online]. Available: https://www.itu.int/rec/T-REC-G.652-201611-I/en.

[5] Corning, "Corning SMF-28e Optical Fiber (Product Information)," [Online]. Available: http://www.tlc.unipr.it/cucinotta/cfa/datasheet_SMF28e.pdf.

[6] G.P. Agrawal, Fiber-Optic Communication Systems (Third Edition), Wiley, 2002.

[7] R.J. Mears, L. Reekie, I.M. Jauncey, and D.N. Payne, "Low-noise erbium-doped fibre amplifier operating at 1.54μm," *Electronics Letters,* vol. 23, no. 19, pp. 1026-1028, 1987.

[8] K. Minoguchi, F. Hamaoka, S. Okamoto, T. Sasai, K. Horikoshi, A. Matsushita, M. Nakamura, E. Yamazaki, and Y. Kisaka, "Beyond 100-Tb/s ultra-wideband transmission in S, C, and L bands over single-mode fiber," in *Proc. SPIE 11309, Next-Generation Optical Communication: Components, Sub-Systems, and Systems IX*, San Francisco, CA, 2020.

[9] A.D. Ellis, J. Zhao, and D. Cotter, "Approaching the Non-Linear Shannon Limit," *Journal of Lightwave Technology,* vol. 28, no. 4, pp. 423-433, 2010.

[10] D.M. Marom, R. Ryf, and D.T. Neilson, "Chapter 16: Networking and routing in space-division multiplexed systems," in *Optical Fiber Telecommunications VII*, Los Angeles, CA, Academic Press, 2019, pp. 719-750.

[11] B. Barua, "Comparison the Performance of Free-Space Optical Communication with OOK and BPSK Modulation under Atmospheric Turbulence," *International Journal of Engineering Science,* vol. 3, no. 5, pp. 4391-4399, 2011.

[12] P.A. Andrekson and M. Karlsson, "Fiber-based phase-sensitive optical amplifiers and their applications," *Advances in Optics and Photonics,* vol. 12, no. 2, pp. 367-428, 2020.

[13] Y. Tamura, H. Sakuma, K. Morita, M. Suzuki, Y. Yamamoto, K. Shimada, Y. Honma, K. Sohma, T. Fujii, and T. Hasegawa, "The First 0.14-dB/km Loss Optical Fiber and its Impact on Submarine Transmission," *Journal of Lightwave Technology,* vol. 36, no. 1, pp. 44-49, 2018.

[14] Z. Liu, B. Karanov, L. Galdino, J.R. Hayes, D. Lavery, K. Clark, K. Shi, D.J. Elson, B.C. Thomsen, M.N. Petrovich, D.J. Richardson, F. Poletti, R. Slavik, and P. Bayvel, "Nonlinearity-Free Coherent Transmission in Hollow-Core Antiresonant Fiber," *Journal of Lightwave Technology,* vol. 37, no. 3, pp. 909-916, 2019.

[15] S.T. Le, M.E. McCarthy, S.K. Turitsyn, I. Phillips, D. Lavery, T. Xu, P. Bayvel, and A.D. Ellis, "Optical and Digital Phase Conjugation Techniques for Fiber Nonlinearity Compensation," in *OptoElectronics and Communication Conference*, Shanghai, China, 2015.

[16] Y. Hong, H. Sakr, N. Taengnoi, K. Bottrill, T. Bradley, J. Hayes, G. Jasion, H. Kim, N.K. Thipparapu, Y. Wang, A.A. Umnikov, J. Sahu, F. Poletti, P. Petropoulos, and D. Richardson, "Multi-Band Direct-Detection Transmission Over an Ultrawide Bandwidth Hollow-Core NANF," *Journal of Lightwave Technology,* vol. 38, no. 10, pp. 2849-2857, 2020.

[17] M.A. Iqbal, L. Krzczanowicz, I.D. Phillips, P. Harper, A. Lord, and W. Forysiak, "Ultra-Wideband Raman Amplifiers for High Capacity Fibre-Optic Transmission Systems," in *2020 22nd International Conference on Transparent Optical Networks (ICTON)*, Bari, Italy, 2020.

[18] Y. Wang, N.K. Thipparapu, D.J. Richardson, and J. K. Sahu, "Ultra-broadband Bismuth-Doped Fiber Amplifier Covering a 115-nm Bandwidth in the O and E Bands," *Journal of Lightwave Technology,* vol. 39, no. 3, pp. 795-800, 2020.

[19] E. Dianov, M. Melkumov, A.V. Shubin, S. Firstov, V. Khopin, A. Guryanov, and I. Bufetov, "Bismuth-doped fibre amplifier for the range 1300 - 1340 nm," *Quantum Electronics,* vol. 39, pp. 1099-1101, 2009.

[20] M.A. Melkumov, I.A. Bufetov, A.V. Shubin, S.V. Firstov, V.F. Khopin, A.N. Guryanov, and E.M. Dianov, "Laser diode pumped bismuth-doped optical fiber amplifier for 1430 nm band," *Optics Letters,* vol. 36, no. 13, pp. 2408-2410, 2011.

[21] J. Kani, K. Hattori, M. Jinno, S. Aisawa, T. Sakamoto, and K. Oguch, "Trinal-wavelength-band WDM transmission over dispersion-shifted fiber," in *OFC/IOOC'99. Technical Digest. Optical Fiber Communication Conference, 1999, and the International Conference on Integrated Optics and Optical Fiber Communication*, San Diego, CA, 1999.

[22] F.A. Flood, "L-band erbium-doped fiber amplifiers," in *Optical Fiber Communication Conference. Technical Digest Postconference Edition. Trends in Optics and Photonics Vol.37*, Baltimore, MD, 2000.

[23] J.B. Rosolem, A.A. Juriollo, and M.A. Romero, "S Band EDFA Using Standard Erbium Doped Fiber, 1450 nm Pumping and Single Stage ASE Filtering," in *OFC/NFOEC 2008 - 2008 Conference on Optical Fiber Communication/National Fiber Optic Engineers Conference*, San Diego, CA, 2008.

[24] T. Kasamatsu, Y. Yano, and T. Ono, "Laser-diode-pumped highly efficient gain-shifted thulium-doped fiber amplifier operating in the 1480-1510-nm band," *IEEE Photonics Technology Letters,* vol. 13, no. 5, pp. 433-435, 2001.

[25] F. Hamaoka, M. Nakamura, S. Okamoto, K. Minoguchi, T. Sasai, and A. Matsushita, "Ultra-Wideband WDM Transmission in S-, C-, and L-Bands Using Signal Power Optimization Scheme [Highly-Scored Paper]," *Journal of Lightwave Technology,* vol. 37, no. 8, pp. 1764-1771, 2019.

[26] J.S. Wang, E.M. Vogel, E. Snitzer, J.L. Jackel, V.L. da Silva, and Y. Silberberg, "1.3 μm emission of neodymium and praseodymium in tellurite-based glasses," *Journal of Non-Crystalline Solids,* vol. 178, pp. 109-113, 1994.

[27] H. Schmeckebier, "Introduction to semiconductor optical amplifiers (SOAs)," in *Quantum-dot-based semiconductor optical amplifiers for o-band optical communication*, Berlin, Germany, Springer, 2017, pp. 13-34.

[28] N. Thipparapu, A. Umnikov, P. Barua, and J.K. Sahu, "Bi-doped fiber amplifier with a flat gain of 25 dB operating in the wavelength band 1320–1360 nm," *Optics Letters,* vol. 41, no. 7, pp. 1518-1521, 2016.

[29] L. Chorchos and J.P. Turkiewicz, "O-Band 8×100 G Data Transmission With 240 GHz Channel Spacing," *IEEE Communications Letters,* vol. 23, no. 12, pp. 2288-2291, 2019.

[30] V. Mikhailov, M.A. Melkumov, D. Inniss, A.M. Khegai, K.E. Riumkin, S.V. Firstov, F.V. Afanasiev, M.F. Yan, Y. Sun, J. Luo, G.S. Puc, S.D. Shenk, R.S. Windeler, P.S. Westbrook, R.L. Lingle, E.M. Dianov, and D.J. DiGiovanni, "Simple Broadband Bismuth Doped Fiber Amplifier (BDFA) to Extend O-band Transmission Reach and Capacity," in *2019 Optical Fiber Communications Conference and Exhibition (OFC)*, San Diego, 2019.

[31] G.P. Agrawal, Nonlinear Fibre Optics, Amsterdam: Elsevier Academic Press, 2007.

[32] R. Hui, "Chapter 5: Optical Amplifiers," in *Introduction to Fiber-Optic Communications*, eBook ISBN: 9780128092347, Academic Press, 2019, pp. 155-207.

[33] T.D. Bradley, J.R. Hayes, Y. Chen, G.T. Jasion, S.R. Sandoghchi, R. Slavik, E.N. Fokoua, S. Bawn, H. Sakr, I.A. Davidson, A. Taranta, J.P. Thomas, M.N. Petrovich, D.J. Richardson, and F. Poletti, "Record Low-Loss 1.3dB/km Data Transmitting Antiresonant Hollow Core Fibre," in *2018 European Conference on Optical Communication (ECOC)*, Rome, Italy, 2018.

[34] M. Zamani, C. Chen, C. Li, and Z. Zhang, "A Blind Channel Estimation for 100+ Gb/s Optical IM-DD DMT Over 100-km SMF in 1550 nm," *IEEE Photonics Technology Letters,* vol. 26, no. 19, pp. 1928-1931, 2014.

[35] Y. Hong, K.R.H. Bottrill, N. Taengnoi, H. Sakr, T. Bradley, J. Hayes, G. Jasion, F. Poletti, D.J. Richardson, and P. Petropoulos, "Beyond 100-Gb/s/λ direct-detection transmission over the S+C+L-bands in an ultra-wide bandwidth hollow core fibre," in *2019 European Conference on Optical Communication (ECOC)*, Dublin, Ireland, 2019.

[36] F. Ouellette, "Dispersion cancellation using linearly chirped Bragg grating filters in optical waveguides," *Optics Letters,* vol. 12, no. 10, pp. 847-849, 1987.

[37] J. Sirkis, "Athermal bragg grating package with course and fine mechanical tuning". United States (US) Patent 6453108, 30 9 2000.

[38] A.S. Karar, J.C. Cartledge, K. Roberts, "Transmission Over 608 km of Standard Single-Mode Fiber Using a 10.709-Gb/s Chirp Managed Laser and Electronic Dispersion Precompensation," *IEEE Photonics Technology Letters,* vol. 24, no. 9, pp. 760-762, 2012.

[39] J. McNicol, M. O'Sullivan, K. Roberts, A. Comeau, D. McGhan, and L. Strawczynski, "Electrical domain compensation of optical dispersion [optical fibre communication applications]," in *OFC/NFOEC Technical Digest. Optical Fiber Communication Conference*, Anaheim, CA,, 2005.

[40] M. Sieben, J. Conradi and, D.E. Dodds, "Optical single sideband transmission at 10 Gb/s using only electrical dispersion compensation," *Journal of Lightwave Technology,* vol. 17, no. 10, pp. 1742-1749, 1999.

[41] P.J. Winzer and R. Essiambre, "Advanced Optical Modulation Formats," *Proceedings of the IEEE,* vol. 94, no. 5, pp. 952-985, 2006.

[42] J. Mo, Y.J. Wen, Y. Dong, Y. Wang, and C. Lu, "Optical minimum-shift keying format and its dispersion tolerance," in *2006 Optical Fiber Communication Conference and the National Fiber Optic Engineers Conference*, Anaheim, CA, 2006.

[43] P. Kabaciński, T.M. Kardaś, Y. Stepanenko, and C. Radzewicz, "Nonlinear refractive index measurement by SPM-induced phase regression," *Optics Express,* vol. 27, no. 8, pp. 11018-11028, 2019.

[44] M. Asobe, "Nonlinear Optical Properties of Chalcogenide Glass Fibers andTheir Application to All-Optical Switching," *Optical Fiber Technology,* vol. 3, no. 2, pp. 142-148, 1997.

[45] Z. Liu, S. Zhang, and F.W. Wise, "Rogue waves in a normal-dispersion fiber laser," *Optics Letters,* vol. 40, no. 7, pp. 1366-1369, 2015.

[46] A.G. Striegler and B. Schmauss, "Analysis and optimization of SPM-based 2R signal regeneration at 40 gb/s," *Journal of Lightwave Technology,* vol. 24, no. 7, pp. 2835-2843, 2006.

[47] E. Ip and J.M. Kahn, "Compensation of dispersion and nonlinear impairments using digital backpropagation," *Journal of Lightwave Technology,* vol. 26, no. 20, pp. 3416-3425, 2008.

[48] S. Aisawa, N. Takachio, and K. Iwashita, "Performance of NRZ-versus RZ-WDM transmission around zero dispersion wavelength over dispersion-shifted fiber," *IEEE Photonics Technology Letters,* vol. 10, no. 4, pp. 615-617, 1998.

[49] L.A.M. Saito, P.D. Taveira, P.B. Gaarde, K. De Souza, and E.A. De Souza, "Multi-pump discrete Raman amplifier for CWDM system in the O-band," in *2006 International Telecommunications Symposium*, 2006, pp. 1005-1009.

[50] R. Hui and M. O'Sullivan, "Chapter 3: Characterization of Optical Devices," in *Fiber optic measurement techniques*, Burlington, MA, Academic Press/Elsevier, 2009, pp. 259-363.

[51] D.M. Baney, "Chapter 13: Characterization of Erbium-doped Fiber," in *Fiber Optic Test and Measurement*, New Jersey, Prentice Hall, 1998, pp. 519-594.

[52] W.J. Miniscalco, L.J. Andrews, A. Thompson, L.J. Quimby, L.B. Vacha, and M.G. Drexhage, "1.3 μm fluoride fiber laser," *Electronics Letters,* vol. 24, no. 1, pp. 28-29, 1988.

[53] H. Taleb, K. Abedi, and S. Golmohammadi, "Dynamic response of quantum-dot semiconductor optical amplifiers electrical, optical, and electro-optical pumping schemes," in *20th Iranian Conference on Electrical Engineering (ICEE2012)*, Tehran, Iran, 2012.

[54] D.J. Feng, C.L. Chiu, E.Y. Lin, T.S. Lay, and T.Y. Chang, "Modulation-Doped InGaAlAs/InP Semiconductor Optical Amplifier Structures Grown by Molecular Beam Epitaxy," *Japanese Journal of Applied Physics,* vol. 45, no. 4A, p. 2426–2429, 2006.

[55] J. Renaudier and A. Ghazisaeidi, "Scaling Capacity Growth of Fiber-Optic Transmission Systems Using 100+nm Ultra-Wideband Semiconductor Optical Amplifiers," *Journal of Lightwave Technology,* vol. 37, no. 8, pp. 1831-1838, 2019.

[56] T. Durhuus, C. Joergensen, B. Mikkelsen, R.J.S. Pedersen, and K.E. Stubkjaer, "All optical wavelength conversion by SOA's in a Mach-Zehnder configuration," *IEEE Photonics Technology Letters,* vol. 6, no. 1, pp. 53-55, 1994.

[57] H. Uenohara and Y. Aikawa, "Hybrid integrated semiconductor optical amplifier-Mach Zehnder interferometer (SOA-MZI)-type all-optical wavelength converter with a selectable delay time push-pull configuration," in *2012 17th Opto-Electronics and Communications Conference (OECC 2012)*, Busan, South Korea, 2012.

[58] T. Akiyama, M. Ekawa, M. Sugawara, K. Kawaguchi, H. Sudo, A. Kuramata, H. Ebe, and Y. Arakawa, "An ultrawide-band semiconductor optical amplifier having an extremely high penalty-free output power of 23 dBm achieved with quantum dots," *IEEE Photonics Technology Letters,* vol. 17, no. 8, pp. 1614-1616, 2005.

[59] Z. Zhu, X. Li, and Y. Xi, "A Polarization Insensitive Semiconductor Optical Amplifier," *IEEE Photonics Technology Letters,* vol. 28, no. 17, pp. 1831-1834, 2016.

[60] T. Zhong and P. Goldner, "Emerging rare-earth doped material platforms for quantum nanophotonics," *Nanophotonics,* vol. 8, no. 11, pp. 2003-2015, 2019.

[61] Thorlabs, "BOA1036S - O-Band Booster Optical Amplifier, CWL = 1350 nm (Typ.), Butterfly Pkg, SMF, FC/APC," [Online]. Available: https://www.thorlabs.com/newgrouppage9.cfm?objectgroup_id=3990&pn=BOA1036S.

[62] G.P. Agrawal and N.A. Olsson, "Self-Phase Modulation and Spectral Broadening of Optical Pulses in Semiconductor Laser Amplifiers," *IEEE Journal of Quantum Electronics,* vol. 25, no. 11, p. 2297–2306, 1989.

[63] G. Valley, "A review of stimulated Brillouin scattering excited with a broad-band pump laser," *IEEE Journal of Quantum Electronics,* vol. 22, no. 5, pp. 704-712, 1986.

[64] A.V. Harish and J. Nilsson, "Suppression of Stimulated Brillouin Scattering in Single-Frequency Fiber Raman Amplifier Through Pump Modulation," *Journal of Lightwave Technology,* vol. 37, no. 13, pp. 3280-3289, 2019.

[65] C.R.S. Fludger, V. Handerek, and R.J. Mears, "Pump to signal RIN transfer in Raman fiber amplifiers," *Journal of Lightwave Technology,* vol. 19, no. 8, pp. 1140-1148, 2001.

[66] M.N. Islam, "Raman Amplifiers for Telecommunications [Invited Paper]," *IEEE Journal of Selected Topics in Quantum Electronics,* vol. 8, no. 3, pp. 548-559, 2002.

[67] M. Nakazawa, M. Tokuda, Y. Negishi, and N. Uchida, "Active transmission line: light amplification by backward-stimulated Raman scattering in polarization-maintaining optical fiber," *Journal of the Optical Society of America B,* vol. 1, no. 1, pp. 80-85, 1984.

[68] L. Krzczanowicz, M.A. Iqbal, I. Phillips, M. Tan, P. Skvortcov, P. Harper, and W. Forysiak, "Low transmission penalty dual-stage broadband discrete Raman amplifier," *Optics Express,* vol. 26, no. 6, pp. 7091-7097, 2018.

[69] M.A. Iqbal, M.A.Z. Al-Khateeb, L. Krzczanowicz, I.D. Phillips, P. Harper, and W. Forysiak, "Linear and Nonlinear Noise Characterisation of Dual Stage Broadband Discrete Raman Amplifiers," *Journal of Lightwave Technology,* vol. 37, no. 14, pp. 3679-3688, 2019.

[70] M. Brierley, S. Carter, P. France, and J.E. Pederson, "Amplification in the 1300 nm telecommunications window in an Nd-doped fluoride fibre," *Electronics Letters,* vol. 26, no. 5, pp. 329-330, 1990.

[71] M. Naftaly and A. Jha, "Nd3+-doped fluoroaluminate glasses for a 1.3 μm amplifier," *Journal of Applied Physics,* vol. 87, no. 5, p. 2098, 2000.

[72] L. Kiani, P. Pax, D.R. Drachenberg, J. Dawson, C. Boley, C. Mart, V. Khitrov, C. Yu, R. Crist, M. Cook, N. Schenkel, M. Runkel, and M. Messerly, "Improved Nd Doped Silica Fiber for E-Band Amplification," in *2020 Optical Fiber Communications Conference and Exhibition (OFC)*, San Diego, CA, 2020.

[73] H. Takebe, K. Yoshino, T. Murata, K. Morinaga, J. Hector, W.S. Brocklesby, D.W. Hewak, J. Wang, and D.N. Payne, "Spectroscopic properties of Nd3+ and Pr3+ in gallate glasses with low phonon energies," *Applied Optics,* vol. 36, no. 24, pp. 5839-5843, 1997.

[74] IEEE Standard, "IEEE Standard for Ethernet - Amendment 11: Physical Layers and Management Parameters for 100 Gb/s and 400 Gb/s Operation over Single-Mode Fiber at 100 Gb/s per Wavelength," *IEEE Std 802.3cu-2021 (Amendment to IEEE Std 802.3-2018 and its approved amendments),* pp. 1-87, 2021.

[75] Y. Nishida, M. Yamada, T. Kanamori, K. Kobayashi, J. Temmyo, S. Sudo, and Y. Ohishi, "Development of an efficient praseodymium-doped fiber amplifier," *IEEE Journal of Quantum Electronics,* vol. 34, no. 8, pp. 1332-1339, 1998.

[76] E. Dianov, "Bismuth-doped optical fibers: a challenging active medium for near-IR lasers and optical amplifiers," *Light: Science & Applications,* vol. 1, no. 15, p. 12, 2012.

[77] I.A. Bufetov, S.L. Semenov, V.V. Vel'miskin, S.V. Firstov, G.A. Bufetova, and E.M. Dianov, "Optical properties of active bismuth centres in silica fbres containing no other dopants," *Quantum Electronics,* vol. 40, no. 7, pp. 639-641, 2010.

[78] E.G. Firstova, I.A. Bufetov, V.F. Khopin, V.V. Vel'miskin, S.V. Firstov, G.A. Bufetova, K.N. Nishchev, A.N. Gur'yanov, and E.M. Dianov, "Luminescence properties of IR-emitting bismuth centres in SiO2-based glasses in the UV to near-IR spectral region," *Quantum Electronics,* vol. 45, no. 1, pp. 59-65, 2015.

[79] N.K. Thipparapu, Y. Wang, S. Wang, A.A. Umnikov, P. Barua, and J.K. Sahu, "Bi-doped fiber amplifiers and lasers [Invited]," *Optical Materials Express,* vol. 9, no. 6, pp. 2446-2465, 2019.

[80] B. Zhang, Y. Chu, X. Fu, S. Wei, J. Wang, Y. Luo, and G. Peng, "Thermal bleaching of BACs in bismuth/erbium co-doped fiber fabricated through 3D silica lithography," *Optics Letters,* vol. 45, no. 13, pp. 3729-3732, 2020.

[81] B. Zhang, S. Wei, M.T.A. Khan, Y. Luo, and G.D. Peng, "Dynamics study of thermal activation of BAC-Si in bismuth/erbium-codoped optical fiber," *Optics Letters,* vol. 45, no. 2, pp. 571-574, 2020.

[82] S. Hwang and K. Cho, "Gain tilt control of L-band erbium-doped fiber amplifier by using a 1550-nm band light injection," *IEEE Photonics Technology Letters,* vol. 13, no. 10, pp. 1070-1072, 2001.

[83] K. Thyagarajan, "Erbium-Doped Fiber Amplifiers," in *Guided Wave Optical Components and Devices*, Academic Press, 2006, pp. 119-129.

[84] Y.W. Lee, J. Nilsson, S.T. Hwang, and S.J. Kim, "Experimental characterization of a dynamically gain-flattened erbium-doped fiber amplifier," *IEEE Photonics Technology Letters,* vol. 8, no. 12, pp. 1612-1614, 1996.

[85] S.L. Hansen, S.B. Andreasen, P. Thorsen, and K. Dybdal, "Experimental verification of new EDFA gain-tilt distortion theory," *IEEE Photonics Technology Letters,* vol. 5, no. 12, pp. 1433-1435, 1993.

[86] S.L. Hansen, P. Thorsen, K. Dybdal, and S.B. Andreasen, "Gain tilt of erbium-doped fiber amplifiers due to signal-induced inversion locking," *IEEE Photonics Technology Letters,* vol. 5, no. 4, pp. 409-411, 1993.

[87] D.R. Zimmerman and L.H. Spiekman, "Amplifiers for the Masses: EDFA, EDWA, and SOA Amplets for Metro and Access Applications," *Journal of Lightwave Technology,* vol. 22, no. 1, pp. 63-70, 2004.

[88] C.R. Giles, E. Desurvire, and J.R. Simpson, "Transient gain and cross talk in erbium-doped fiber amplifiers," *Optics Letters,* vol. 14, no. 16, pp. 880-882, 1989.

[89] J. Yao, "Photonics for ultrawideband communications," *IEEE Microwave Magazine,* vol. 10, no. 4, pp. 82-95, 2009.

[90] T. Panayiotou, N. Antoniades, and G. Ellinas, "On the impact of polarization-dependent gain/loss for optical multicast sessions," *Optics Express,* vol. 22, no. 24, pp. 29827-29834, 2014.

[91] R. Sabella and P. Lugli, "Multichannel Optical Systems," in *High Speed Optical Communications*, Springer US, 1999.

[92] H. Ahmad and S.W. Harun, "Double-pass L-band EDFA with flat-gain and improved noise figure characteristic," in *2004 IEEE Region 10 Conference TENCON 2004, pp. 75-77*, Chiang Mai, Thailand, 2004.

[93] D.M. Baney, P. Gallion, and R.S. Tucker, "Theory and Measurement Techniques for the Noise Figure of Optical Amplifiers," *Optical Fiber Technology,* vol. 6, no. 2, pp. 122-154, 2000.

[94] P. Urquhart and T.J. Whitley, "Long span fiber amplifiers," *APPLIED OPTICS,* vol. 29, pp. 3503-3509, 1990.

[95] M.N. Zervas and R.I. Laming, "Rayleigh Scattering Effect on the Gain Efficiency and Noise of Erbium-Doped Fiber Amplifiers," *Journal of Quantum Electronics,* vol. 31, p. 468–471, 1995.

[96] H.R. Mojaver, A.S. Dhillon, R.B. Priti, V.I. Tolstikhin, K. Leong, and O. Liboiron-Ladouceur, "Lossless Operation of an 8 × 8 SiPh/InP Hybrid Optical Switch," *IEEE Photonics Technology Letters,* vol. 32, no. 11, pp. 667-670, 2020.

[97] L.L. Yi, L. Zhan, J.H. Ji, Q.H. Ye, and Y.X. Xia, "Improvement of gain and noise figure in double-pass L-band EDFA by incorporating a fiber Bragg grating," *IEEE Photonics Technology Letters,* vol. 16, no. 4, pp. 1005-1007, 2004.

[98] S.W. Harun, P. Poopalan, and H. Ahmad, "Gain enhancement in L-band EDFA through a double-pass technique," *IEEE Photonics Technology Letters,* vol. 14, no. 3, pp. 296-297, 2002.

[99] L. Fei and L. Houbing, "Optimum detection threshold for free-space optical communication with atmospheric scintillation," in *2015 International Conference on Optoelectronics and Microelectronics (ICOM)*, Changchun, China, 2015.

[100] M. Tang, P. Shum, and Y.D. Gong, "Design of double-pass discrete Raman amplifier and the impairments induced by Rayleigh backscattering," *Optics Express,* vol. 11, no. 16, pp. 1887-1893, 2003.

[101] R. Gutierrez-Castrejon and A. Filios, "Pattern-Effect Reduction Using a Cross-Gain Modulated Holding Beam in Semiconductor Optical In-Line Amplifier," *Journal of Lightwave Technology,* vol. 24, no. 12, pp. 4912-4917, 2006.

[102] S. Liang, S. Jain, L. Xu, K.R.H. Bottrill, N. Taengnoi, M. Guasoni, P. Zhang, M. Xiao, Q. Kang, Y. Jung, P. Petropoulos, and D.J. Richardson, "High Gain, Low Noise, Spectral-Gain-Controlled, Broadband Lumped Fiber Raman Amplifier," *Journal of Lightwave Technology,* vol. 39, no. 5, pp. 1458-1463, 2021.

[103] C.B. Gaur, F. Ferreira, V. Gordienko, V. Ribeiro, Á.D. Szabó, and N.J. Doran, "Experimental comparison of fiber optic parametric, Raman and erbium amplifiers for burst traffic for extended reach PONs," *Optics Express,* vol. 28, no. 13, pp. 19362-19373, 2020.

[104] B. Zhu, "Entirely passive coexisting 10G-PON and GPON compatible reach extender using Raman amplification," *Optics Express,* vol. 20, no. 3, pp. 2290-2296, 2012.

[105] F. Wei, F. Yang, X. Zhang, D. Xu, M. Ding, L. Zhang, D. Chen, H. Cai, Z. Fang, and G. Xijia, "Subkilohertz linewidth reduction of a DFB diode laser using self-injection locking with a fiber Bragg grating Fabry-Perot cavity," *Optics Express,* vol. 24, no. 15, pp. 17406-17415, 2016.

[106] Z.Q. Pan, J. Zhou, F. Yang, Q. Ye, H.W. Cai, R.H. Qu, and Z.J. Fang, "Low-frequency noise suppression of a fiber laser based on a round-trip EDFA power stabilizer," *Laser Physics,* vol. 23, p. 035105, 2013.

[107] P. Czyżak, P. Mazurek, and J.P. Turkiewicz, "1310nm Raman amplifier utilizing high-power quantum-dot pumping lasers," *Optics & Laser Technology,* vol. 64, pp. 195-203, 2014.

[108] S.Peiris, N. Madamopoulos, N. Antoniades, D. Richards, and R. Dorsinville, "Performance Analysis of a Hybrid Raman Optical Parametric Amplifier in the O- and E-Bands for CWDM PONs," *Photonics,* vol. 1, no. 4, pp. 473-487, 2014.

[109] L. Chen, P. Dong, and Y. Chen, "Chirp and Dispersion Tolerance of a Single-Drive Push–Pull Silicon Modulator at 28 Gb/s," *IEEE Photonics Technology Letters,* vol. 24, no. 11, pp. 936-938, 2012.

[110] G. de Valicourt, M. Mestre, N. Moroz, and Y. Pointurier, "Semiconductor optical amplifier for next generation of high data rate optical packet-switched networks," in *Some Advanced Functionalities of Optical Amplifiers*, IntechOpen, 2015.

[111] P.S. Cho, Y. Achiam, G. Levy-Yurista, M. Margalit, Y. Gross and J.B. Khurgin, "Investigation of SOA Nonlinearities on the Amplification of DWDM Channels With Spectral Efficiency Up to 2.5 b/s/Hz," *IEEE Photonics Technology Letters,* vol. 16, no. 3, pp. 918-920, 2004.

[112] K.S. Kim, R.H. Stolen, W.A. Reed, and K.W. Quoi, "Measurement of the nonlinear index of silica-core and dispersion-shifted fibers," *Optics Letters,* vol. 19, no. 4, pp. 257-259, 1994.

[113] C. Xie, L. Wang, L. Dou, M. Xia, S. Chen, H. Zhang, Z. Sun, and J. Cheng, "Open and disaggregated optical transport networks for data center interconnects [Invited]," *Journal of Optical Communications and Networking,* vol. 12, no. 6, pp. C12-C22, 2020.

[114] Optical Internetworking Forum, "Implementation agreement 400ZR [White paper]," *OIF-400ZR-01.0,* 2020.

[115] X. Wei, A.H. Gnauck, X. Liu, and J. Leuthold, "Nonlinearity tolerance of RZ-AMI format in 42.7 Gbit/s long-haul transmission over standard SMF spans," *Electronics Letters,* vol. 39, no. 20, pp. 1459-1461, 2003.

[116] K. Cheng and J. Conradi, "Reduction of pulse-to-pulse interaction using alternative RZ formats in 40-Gb/s systems," *IEEE Photonics Technology Letters,* vol. 14, no. 1, pp. 98-100, 2002.

[117] P.J. Winzer, A.H. Gnauck, G. Raybon, S. Chandrasekhar, Y. Su, and J. Leuthold, "40-Gb/s return-to-zero alternate-mark-inversion (RZ-AMI) transmission over 2000 km," *IEEE Photonics Technology Letters,* vol. 15, no. 5, pp. 766-768, 2003.

[118] G. Lu, L. Chen, and C. Chan, "A simple AMI-RZ transmitter based on single-arm intensity modulator and optical delay interferometer," *Optics Communications,* vol. 255, no. 1-3, pp. 35-40, 2005.

[119] A.S. Siddiqui, S.G. Edirisinghe, J.J. Lepley, J.G. Ellison, and S.D. Walker, "Dispersion-tolerant transmission using a duobinary polarization-shift keying transmission scheme," *IEEE Photonics Technology Letters,* vol. 14, no. 2, pp. 158-160, 2002.

[120] M. Aleksejeva and S. Spolitis, "Research on NRZ-OOK and Duobinary Modulation formats for C and L band 25 Gbit/s WDM-PON Transmission Systems," in *2018 Advances in Wireless and Optical Communications (RTUWO)*, 2018.

[121] Y. Xu, P. Yu, N. Ye, and Y. Song, "Experimental analysis of four-wave mixing effect on next generation Ethernet passive optical network," *Optical Engineering,* vol. 59, no. 7, p. 076114, 2020.

[122] Y. Hong, K.R.H. Bottrill, N. Taengnoi, N.K. Thipparapu, Y. Wang, J.K. Sahu, D.J. Richardson, and P. Petropoulos, "Numerical and experimental study on the impact of chromatic dispersion on O-band direct-detection transmission," *Applied Optics,* vol. 60, no. 15, pp. 4383-4390, 2021.

[123] A. Ciżman and R. Poprawski, "Set-up for spontaneous and induced birefringence measurements," *Optica Applicata,* vol. 35, no. 1, pp. 163-170, 2005.

[124] J. Verbist, J. Lambrecht, M. Verplaetse, J. Van Kerrebrouck, A. Srinivasan, P. De Heyn, T. De Keulenaer, X. Yin, G. Torfs, J. Van Campenhout, G. Roelkens, and J. Bauwelinck, "DAC-Less and DSP-Free 112 Gb/s PAM-4 Transmitter Using Two Parallel Electroabsorption Modulators," *Journal of Lightwave Technology,* vol. 36, no. 5, pp. 1281-1286, 2018.

[125] Y. You, W. Zhang, L. Sun, J. Du, C. Liang, F. Yang, and Z. He, "Time skewing and amplitude nonlinearity mitigation by feedback equalization for 56 Gbps VCSEL-based PAM-4 links," *Optics Communications,* vol. 410, pp. 909-915, 2018.

[126] Z. Liu and R. Slavík, "Optical injection locking: From principle to applications," *Journal of Lightwave Technology,* vol. 38, no. 1, pp. 43-59, 2020.

[127] A.N. Pilipetskii, B. Bakhshi, M. Vaa, M. Nissov, and N.S. Berganon, "The interaction between fiber PMD and polarization hole burning in long-haul transmission systems," in *OFC/NFOEC Technical Digest. Optical Fiber Communication Conference, 2005*, Anaheim, CA, 2005.

[128] H. Sakr, Y. Chen, T.D. Bradley, G.T. Jasion, J.R. Hayes, I.A. Davidson, E.N. Fokoua, N.V. Wheeler, D.J. Richardson, and F. Poletti, "Advances in Hollow Core Fiber for the 1μm and Visible Wavelength Regions," in *OSA Advanced Photonics Congress (AP) 2020 (IPR, NP, NOMA, Networks, PVLED, PSC, SPPCom, SOF)*, 2020.

[129] H. Sakr, Y. Hong, T.D. Bradley, G.T. Jasion, J.R. Hayes, H. Kim, I.A. Davidson, E.N. Fokoua, Y. Chen, K.R.H. Bottrill, N. Taengnoi, N.V. Wheeler, P. Petropoulos, D.J. Richardson, and F. Poletti, "Interband Short Reach Data Transmission in Ultrawide Bandwidth Hollow Core Fiber," *Journal of Lightwave Technology,* vol. 38, no. 1, pp. 159-165, 2020.

[130] G.T. Jasion, T.D. Bradley, K. Harrington, H. Sakr, Y. Chen, E.N. Fokoua, I.A. Davidson, A. Taranta, J.R. Hayes, D.J. Richardson, and F. Poletti, "Hollow Core NANF with 0.28 dB/km Attenuation in the C and L Bands," in *2020 Optical Fiber Communications Conference and Exhibition (OFC)*, San Diego, CA, 2020.

[131] Y. Hong, K.R.H. Bottrill, T.D. Bradley, H. Sakr, G.T. Jasion, K. Harrington, F. Poletti, P. Petropoulos, and D.J. Richardson, "Low-Latency WDM Intensity-Modulation and Direct-Detection Transmission Over >100 km Distances in a Hollow Core Fiber," *Laser & Photonics Reviews,* vol. 15, no. 9, p. 2100102, 2021.